Thermophysical and structural properties of the equilibrium and undercooled melt of bulk metallic glasses investigated by electrostatic levitation

Dissertation

zur Erlangung des Grades
Doktor der Ingenieurswissenschaften (Dr. Ing.)

der Naturwissenschaftlich-Technischen Fakultät III
Chemie, Pharmazie und Werkstoffwissenschaften
der

Universität des Saarlandes

von

Isabell Jonas

angefertigt am

Institut für Materialphysik im Weltraum, des
Deutschen Zentrums für Luft- und Raumfahrt (DLR)

Köln 2016

Tag des Kolloquiums: 14.02.2017

Dekan der Fakultät: Prof. Dr. rer. nat. Guido Kickelbick
Berichterstatter :   Prof. Dr. rer. nat. Ralf Busch
                         Prof. Dr.-Ing. Frank Mücklich
Vorsitz: Prof. Dr.-Ing. Dirk Bähre
Akad. Mitarbeiterin: Dr.-Ing. Dr. rer. nat. Anne Jung

Abstract

Upon quenching a liquid into a glass, its viscosity increases drastically. A "strong" liquid is characterised by an Arrhenius-like temperature dependency of the viscosity with a temperature independent activation energy. For a "fragile" liquid, the activation energy increases monotonically. In many bulk metallic glasses (BMGs) both strong and fragile behaviour can be observed at different temperatures. However, most of these strong-to-fragile crossovers take place in the undercooled state, where experimental data is rare because this region is masked by crystallisation. This fact and the chemical reactivity of metallic melts make investigations of an underlying transition and of accurate melt viscosities experimentally challenging.

In this work, electrostatic levitation was used for investigations of Zr-based BMGs, providing precise high temperature data over a broad temperature range and enabling access to the deeply undercooled melt. With this new data, we confirmed that the investigated BMGs exhibit different fragilities.
Studies of the undercooled melt revealed indications for a transition in specific heat capacity and in local structure changes at the same temperature.

These indications are associated with a structural transition and are attributed to be the origin of the difference in fragility. The underlying mechanism may be due to a liquid-liquid transition. Whether there are chemical composition changes in the different liquid phases is subject to further studies.

Zusammenfassung

Beim Abschrecken einer Flüssigkeit in den Glaszustand steigt die Viskosität drastisch. Eine "starke" Flüssigkeit ist gekennzeichnet durch eine Arrhenius-artige Temperaturabhängigkeit der Viskosität und eine temperaturunabhängige Aktivierungsenergie. Eine "fragile" Flüssigkeit weist eine monoton steigende Aktivierungsenergie auf. Viele metallische Massivglas (MMG) Bildner zeigen sowohl "starkes" als auch "fragiles" Verhalten bei verschiedenen Temperaturen. Allerdings finden die meisten dieser Übergänge in der unterkühlten Schmelze statt, wo aufgrund von Kristallisation kaum experimentelle Daten verfügbar sind. Dieser Umstand und die chemische Reaktivität metallischer Schmelzen erschweren Untersuchungen zugrunde liegender Übergange sowie präzise Viskositätsdaten.

In dieser Arbeit wurde Elektrostatische Levitation genutzt um Zr-basierte MMG zu untersuchen, da sie über einen großen Bereich präzise Hochtemperaturdaten sowie Zugang zu unterkühlten Schmelzen liefert. Es wurde bestätigt, dass die untersuchten MMG unterschiedliche Fragilitäten aufweisen. Untersuchungen der unterkühlten Schmelze zeigten Hinweise auf einen Übergang in der spezifischen Wärmekapazität und in Strukturänderungen bei derselben Temperatur.

Diese Hinweise wurden mit einem strukturellen Übergang assoziiert und als Ursache der verschiedenen Fragilitäten angenommen. Der zugrunde liegende Mechanismus könnte ein Flüssig-Flüssig-Übergang sein. Ob Entmischung dabei eine Rolle spielt, ist Gegenstand weiterer Forschung.

Contributions and publications

This thesis was created as part of a joint German Research Foundation (DFG) Project between the Institute of Materials Physics in Space at the German Aero Space Center (Me 1958/11-2) and the Chair of Metallic Materials at the University Saarland.

The experimental results presented in chapter 5, which are obtained by electrostatic levitation technique were collected, analysed, and interpreted by the author. Results obtained by Couette rheometry were collected and analysed by W. Hembree, University Saarland. Microgravity results obtained by using the TEMPUS facility belonging to the Institute of Materials Physics in Space were prepared and analysed either by the author or by W. Hembree, as cited accordingly in chapter 5.1. The author, F. Yang, W. Hembree, M. Stolpe, S.Wei, Z. Evenson, C. Yuan, and D. Holland-Moritz planned and carried out x-ray experiments at PETRA III, DESY Hamburg. The author and F. Yang analysed the diffraction data presented within this thesis. Fan Yang was responsible for assisting with experimental implementations and supervising this thesis. The overall research direction and project administration was conducted by A. Meyer.

At the time of writing this thesis, there has been one publication based on results presented within this work:

- M. Stolpe, I. Jonas, S. Wei, W. Hembree, F. Yang, A. Meyer, and R. Busch, Structural changes during a liquid-liquid transition in the deeply undercooled $Zr_{58.5}Cu_{15.6}Ni_{12.8}Al_{10.3}Nb_{2.8}$ bulk metallic glass forming melt, *Phys. Rev. B* **93**, 014201 (2016)

Additionally, results of this thesis have contributed to international academic conferences and workshops:

- I. Jonas, F. Yang, and A. Meyer; Possible liquid-liquid transition in BMGs investigated by levitation techniques. Oral presentation at the 10th International Conference on Bulk Metallic Glasses, June 2014, **Shanghai, China.**

- I. Jonas, W. Hembree, R. Busch, and A. Meyer; Measurement of viscosity in Zr-based glass forming alloys. Poster presentation at the 3rd Sino German Workshop, May 2015, **Hefei, China.**

Contents

Chapter 1

Introduction

Glasses are solids with an amorphous, liquid-like structure [103]. They form when a melt is rapidly cooled to below its glass transition temperature without crystallisation setting in. If these glasses consist of metals and form bulk glassy specimens of critical thicknesses larger than 1 mm, they are referred to as bulk metallic glasses (BMGs). The first BMG was discovered in 1982 by Drehmann et al. [32].

The large casting thicknesses of good glass formers require only low cooling rates to avoid crystallisation. Their melts exhibit a high thermal stability against crystallisation. Furthermore, the driving force for crystallisation between the undercooled and crystalline state is low, while kinetics are sluggish and impede nucleation and crystal growth.

Kinetic properties of BMGs, such as viscosity or relaxation time vary with temperature over many orders of magnitude from just a few mPas in the equilibrium melt to 10^{12} Pas at the glass transition temperature. If the temperature dependence follows a near-Arrhenius behaviour, the liquid is classified as strong whereas a non-Arrhenius behaviour is defined as fragile [5]. The deviation from the Arrhenius behaviour is defined as fragility (D*) [8]. Recent studies revealed a transition in BMGs from a kinetically strong behaviour in the vicinity of the glass transition temperature to a fragile behaviour in the liquid state [38]. A transition between these kinetically different states is known as a strong-to-fragile crossover and can also be found in other glass-forming systems, like inorganic or polymer glasses [112] and in network-formers (SiO$_2$ [9]) or molecular liquids (ortho-terphenyl [9]). The origin of such a crossover is not well understood, but suspected to be a thermodynamic transition hidden in the undercooled melt or even below the glass transition temperature [9, 112]. In literature it is commonly referred to as a liquid-liquid transition (LLT) [114].

Earlier studies of the LLT focused on water [101, 7, 26, 67]. They revealed comparable and possibly transferable findings. Ito et al. [54] for instance showed that water possesses an Arrhenius-like temperature dependence of the relaxation time near the glass transition temperature in contrast to a highly non-Arrhenius behaviour at the melting temperature. This indicates that a dynamic crossover also exists in water. Further studies (on water) revealed a polyamorphic transi-

tion hidden in the experimentally inaccessible undercooled temperature range [54, 74, 75]. Even further indications for an underlying transition were found in the form of thermodynamic signals in heat capacity maxima [7, 54]. However, no direct connection between polyamorphism, fragility, and thermodynamic signals is detected so far. But the origin of these phenomena found in water is suspected to arise from the same underlying process, which is possibly an LLT.

It is common for all systems showing indications for an underlying transition to be complicated by the fact that these transitions are mostly located in the undercooled melt or at high temperatures and high (or negative) pressures beyond the experimentally accessible range. Therefore, further thermophysical or structural parameters are desirable to characterise such transitions and elucidate their nature.

The ability of BMGs to exist in the undercooled liquid state offers access to this very state and allows for investigations of important thermodynamic and physical properties which describe such a dynamic crossover phenomenon and ultimately its underlying origin.

In analogy to water, some indications for an underlying transition were found in BMG forming liquids [62, 121]. Way et al. [111] discovered different temperature dependencies in the viscosity of the equilibrium melt of Vitreloy 1 depending on the measurement's starting temperature. Recently, indications for an underlying transition were found in the heat capacity behaviour and in structural information [114], as well as in computer simulations [86, 90, 48]. However, most transitions seem to occur in the undercooled liquid state and are thus hidden by crystallisation. Therefore, experimental difficulties make it challenging to directly observe a strong-to-fragile crossover and its underlying origin. In fact, not only investigations of the undercooled state but also of the melt of BMGs are experimentally challenging, because metallic melts are chemically highly reactive. These difficulties are reflected by the fact that melt viscosities covering two orders of magnitude have been published for the BMG Vitreloy 1 [111, 69, 76, 46].

Therefore, one aim of this work is to compare different high temperature measurement methods with each other and discuss them in terms their of accuracy. These measurement methods are Couette rheometry and electrostatic (ESL) as well as electromagnetic (EML) levitation in combination with the oscillating drop technique and the latter under microgravity conditions. Only with accurate high temperature data is it possible to review indications of a transition and its underlying origin.

In the following, electrostatic levitation is used to systematically investigate several Zr-based BMGs in terms of indications to elucidate the underlying transition and its origin. This is done by means of viscosity, density, specific volume, thermal expansion coefficients, and specific heat capacity. Moreover, structural properties of these BMGs are reviewed by combining electrostatic levitation experiments with high energy x-ray investigations. Here, indications for an underlying transition are sought on the atomic scale in time-resolved experiments.

Chapter 2

Theoretical principles

This chapter introduces first the principle of glass formation before discussing thermodynamic and kinetic aspects of glass formation. It then deals with the structure and specific features of metallic glasses followed by an overview of the history and development of metallic and bulk metallic glasses. In the next section, the basics of viscosity are explained followed by a discussion about viscosity in glass forming systems and the introduction of fragility. In the last section of this chapter, phase transitions and their characteristics are introduced in terms of the Ehrenfest classification followed by a literature review on the liquid-liquid transition.

2.1 Formation and properties of metallic glasses

2.1.1 Glass formation

If a liquid is cooled from its equilibrium state, it falls below the melting temperature at some stage. Upon passing the melting temperature, nucleation usually sets in, followed by crystallisation upon further cooling. Such a transition from the liquid to the crystalline state is accompanied by a change in volume and enthalpy, as depicted in figure 2.1. It is a typical example of a phase transition of the first order [106].

However, if nucleation can be suppressed the system enters a metastable undercooled state. If this state is preserved by sufficiently high cooling rates to below the glass transition temperature, T_g the system is considered to be a glass or an amorphous solid. The transition temperature from an undercooled melt to a glass depends on the cooling rate, as indicated in figure 2.1 by different cooling rates and the according glass transition temperatures (T_{g1} and T_{g2}).
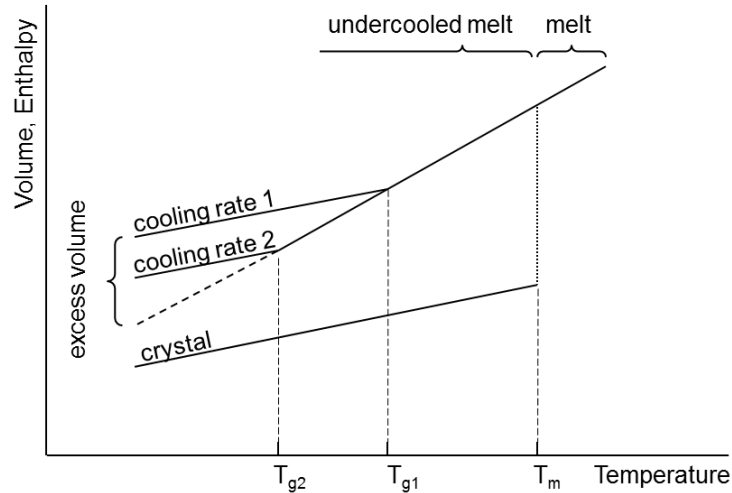
Figure 2.1 – Schematic plot of volume and enthalpy changes upon cooling of a liquid. The transition from the undercooled melt into the glassy state is marked by the glass transition temperature, T_g and is accompanied by an abrupt change in volume, enthalpy, and entropy. T_g depends on the cooling rate and can take place at different temperatures as indicated by T_{g1} and T_{g2}.

2.1.2   Thermodynamic and kinetic aspects of glass formation

The equilibrium state of a melt can be described by the Gibbs free energy, G and the state variables temperature, T, pressure, P, and the number of particles, n as

$$G\,(P,\,T,\,n) = U - T\,S + P\,V \tag{2.1}$$

where U is the internal energy, S the entropy, and V the volume of the system. Figure 2.2 shows the Gibbs free energy of a solid and a liquid phase as function of the temperature at constant pressure and number of particles. For this case the last term of equation 2.1 (PV) can be neglected. In thermodynamic equilibrium, a system will always assume the lowest energy state possible. Therefore, a system above its melting temperature, T_{melt} exists in a liquid state (dashed line), while below its melting point it exists in a solid state (solid line). At the melting temperature, solid and liquid phase are in thermodynamic equilibrium.

Upon undercooling a system below its melting temperature without crystallisation setting in a difference in Gibbs free energy between the undercooled melt and the solid phase forms. This difference, ΔG is the driving force for crystallisation. For the formation of glasses ΔG should be as small as possible, in order to reduce the driving force for crystallisation to a minimum. A system in the undercooled state, thus below its melting temperature possesses a higher energy than in the crystalline state. Therefore, an undercooled melt is a thermodynamically metastable state.
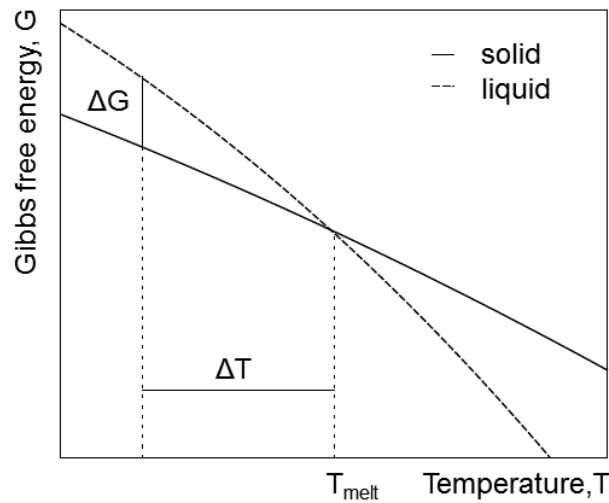
Figure 2.2 – The Gibbs free energy of a solid and a liquid phase as function of temperature. The intersection of the two curves defines the melting point [59]. The difference (ΔG) between the two energies is the driving force for crystallisation.

Upon further undercooling a system eventually passes its glass transition temperature, where it falls out of the metastable state and is considered a "frozen in" liquid. This means the system is kinetically inhibited. The glass transition is associated with a structural arrest. Therefore local density variations can not be compensated anymore. The restricted mobility of atoms or molecules leads to a "freezing in" of excess volume. The general understanding is that the larger the cooling rate, the sooner kinetic processes are inhibited, the more excess volume is frozen in (see figure 2.1), and the sooner the glassy state is reached, meaning in turn that the glass transition shifts to higher temperatures.

Therefore, the glass transition is not a transition in the thermodynamic sense. It is rather considered as a kinetic freezing or unfreezing event on laboratory time scales [112].

2.1.3 Metallic and bulk metallic glasses

The first metallic glass was discovered in 1960 by quenching an Au-Si melt [58]. The development of further metallic glasses consisting of binary and multicomponent alloys followed. All these glasses, which are also referred to as conventional glasses, have in common that in order to produce them critical cooling rates of 10^5 -10^6 K/s are required. Therefore, and because of the finite thermal conductivity, only critical thicknesses of a few hundred μm are possible.

In the early 1980's the first bulk metallic glasses with critical thicknesses of more than 10 mm were developed. The first BMG of this sort was a Pd-based system [32, 61]. Further Zr- [83, 52, 55] and Ce-based [121] systems followed.

BMG formers are typically multicomponent alloys consisting of three to five components and a large atomic size mismatch [98]. They mostly possess a composition close to a deep eutectic in combination with a negative heat of mixing and a low melting temperature [10, 112]. Moreover, BMGs are characterised by relatively low critical cooling rates, for instance in the order of $10\,K/s$ for critical thicknesses of ~ $10\,mm$ [12] in Pd-based BMGs. These cooling rates allow the formation of amorphous structures with drastically enlarged critical thicknesses. For instance up to $70\,mm$ in $Pd_{43}Cu_{27}Ni_{10}P_{20}$ or up to $25\,mm$ in $Zr_{46.75}Ti_{8.25}Cu_{7.5}Ni_{10}Be_{27.5}$ [12].

BMGs with good glass forming abilities (GFA) exhibit an excellent thermal stability against crystallization [66, 95] at relatively low critical cooling rates. The critical cooling rate necessary to bypass crystallisation is reflected in a time-temperature-transformation (TTT) diagram, as schematically shown in figure 2.3.

Shape and location of the c-shaped "nose" indicate the time and temperature range where crystallisation typically sets in. Above the liquidus temperature, T_{liq} the system is in the liquid state. Below T_{liq} the system can either exist in as an undercooled melt or in a crystallised state. Upon sufficient high cooling rates, the "nose" can be bypassed and the glassy state (below T_g) is reached.
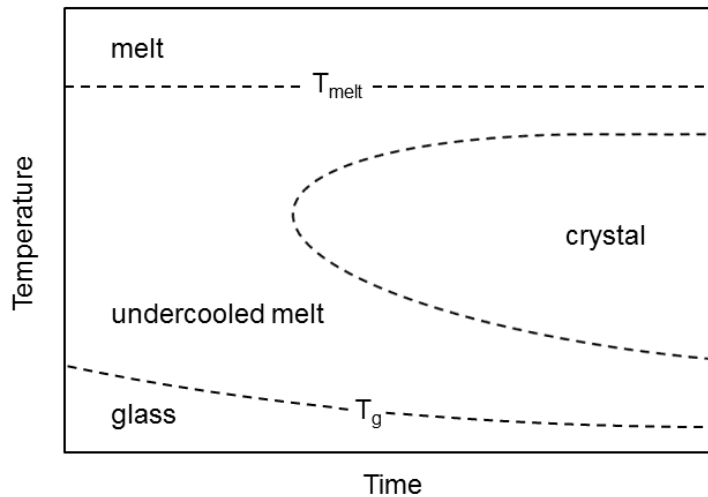
Figure 2.3 – Time-temperature-transformation (TTT) diagram of an arbitrary system.

Thus, BMGs offer excellent conditions for thermophysical and structural investigations of the undercooled state, as carried out in this work.

2.1.4 Structure of metallic glasses

Metallic glasses exhibit an amorphous structure. This means, they lack the highly ordered arrangement of atoms in a recurring lattice structure. Instead, their individual atoms exhibit a disordered structure on the atomic scale. Therefore, the structure of a glass (and an undercooled melt) is compared to that of a liquid. It is also referred to as "frozen in" liquid.

Metallic glasses forming liquids are densely packed systems with a slow dynamic. This is achieved by combining atoms of different sizes. Atoms larger than the main atom size increase the elastic stress between atoms. This hinders diffusion and increases the thermal stability of a glass-forming alloy. Atoms smaller than the main atom size fill in gaps and thereby increase the (packing) density.

The difference in structure between an amorphous and a crystalline structure is well reflected in x-ray experiments. Figure 2.4 displays such a diffraction diagram of a metallic glass solidified once in an amorphous and once in a crystalline state. The amorphous state (top) shows smooth peaks and a rather broad first peak, indicating only a short-range order and no indications for crystallisation, while the crystalline state (bottom) shows a sharpened and increased first peak and many small Bragg peaks, which arise from the different lattice planes of crystals and thus indicate crystallisation.
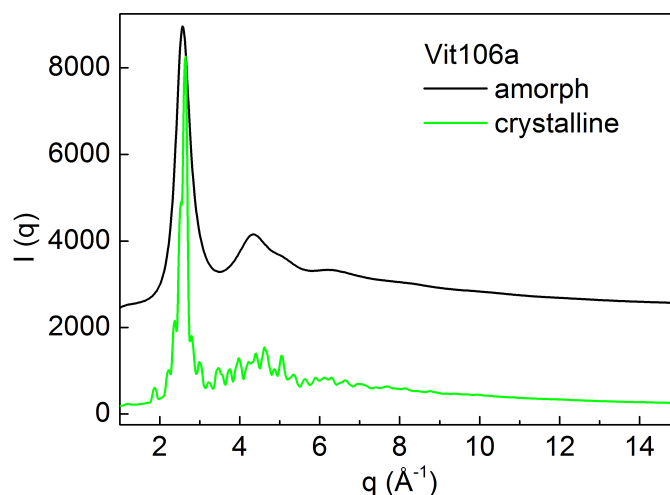
Figure 2.4 – X-ray diffraction diagram of the bulk metallic glass Vit106a. Two diffraction curves of the sample once in the amorphous state (top) and once in the crystalline state (bottom) are shown. The amorphous curve is shifted for clarity.

Several models to describe a simple liquid structure have been developed using hard spheres to depict the individual atoms [28, 16], such as the "dense random packing" model by Scott (for equal spheres [97]) or Bernal (for randomly packed spheres [17]). These models offer a useful

approach for scientific considerations. However, they meet their limits for multicomponent systems of more than three different elements.

As previously mentioned, upon rapid cooling of a metallic glass-forming melt into the glassy state excess volume is frozen in. Re-heating this glass to below its caloric glass transition temperature, allows the short-range order associated with that particular temperature to finally form. This process is called aging. If all excess volume is annealed, the glass possesses the volume of the undercooled melt [12].

The annealing of excess volume, which is also called relaxation, is linked to a change in volume and enthalpy. However, it also entails a change in other physical properties. A decrease in volume for example, is accompanied by a denser state of the equilibrium liquid/structure and thus leads to a higher packing fraction. This in turn slows down diffusion [57, 107] and increases viscosity [36].

2.2 Viscosity

Viscosity is an important parameter in rheology. It is used to describe the dynamic of a fluid on a macroscopic scale [45]. Furthermore, it is understood as a measure of the internal friction of a fluid.

Additionally, it is one of the few parameters which currently show indications for the proposed liquid-liquid transition [114]. Therefore, it is discussed in the following section.

2.2.1 Dynamical viscosity

The dynamical viscosity expresses the resistance of a liquid to shear flow. It is frequently also associated with the "thickness" of a liquid [19].

For the definition of the dynamical viscosity a viscous fluid between two parallel plates is considered, as illustrated in figure 2.5.

This setup assumes two plates, at a distance y apart, which enclose a fluid. One plate is sheared by the force, $\vec{F}$ and with the velocity $\vec{v}$, parallel to the other plate which is stationary. Assuming that the fluid is divided into infinitesimal small vertical layers which stick to each other and the plates, a flow profile is created along the y direction caused by internal friction. If the upper plate moves, the layer in direct proximity will move as well because of the adhesion to the next layer and so on. The velocity, $\vec{v}$ with which the individual layers move, decreases towards the stationary plate. This relation is described by

$$\vec{F} = \eta \, A \, \frac{dv}{dy} \quad . \tag{2.2}$$

Here A is the area of the plates and η the viscosity [68, 45]. Hence, the viscosity describes the
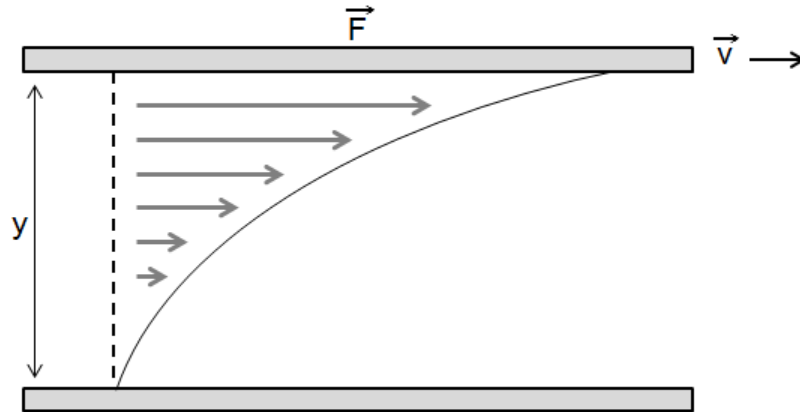
Figure 2.5 – Schematic setup of a laminar shearing process to define the viscosity of a fluid between two plates.

resistance of a fluid to a deformation by shear stress or the other way around, viscosity describes the capability of a liquid to flow. The viscosity is given in $\eta = N\,s/m^2 = Pa\,s$.

If the viscosity is independent of shear velocity and time, it is considered to be a Newtonian liquid.

2.2.2 Viscosity in glass forming systems

Viscosity, on the one hand can be used to define the glass transition temperature. If a melt upon undercooling and without crystallisation setting in, reaches a viscosity of 10^{12} Pas, it is per definition at its glass transition temperature.

On the other hand, the temperature dependence of the viscosity can be used to distinguish two different classes of glass-forming alloys.
For this, the viscosity is plotted on a logarithmic scale against the inverse temperature normalised with respect to the glass transition temperature, T_g/T, thus in an Arrhenius plot [5], as shown in figure 2.6. Based on this notation two classes of glass formers can be distinguished. Kinetically strong glass formers which show a near Arrhenius behaviour and fragile glass formers which exhibit drastic changes in the temperature dependence of the viscosity particularly around T_g.
The temperature dependence of the viscosity, $\eta(T)$ can be described by the Vogel-Fulcher-Tammann equation [38]:

$$\eta(T) = \eta_0 \exp\left(\frac{D^* \, T_0}{T - T_0}\right) \tag{2.3}$$

Here T is the temperature, T_0 is the temperature at which the barriers with respect to flow would approach infinity [5], and D* is the fragility parameter, which quantitatively describes the degree

of deviation from the Arrhenius behaviour [36]. The strongest glass formers possess a D* value of D* ≈ 100, while the most fragile glass formers have a D* value of around 2 [36]. Examples for strong liquids are SiO_2 (D* = 100 [51]) and GeO_2, whereas ortho-terphenyl (D* = 5 [104]) and chlorobenzene represent fragile liquids.

The pre-exponential factor η_0 is the theoretical infinite-temperature limit for η, according to $\eta_0 = h\,N_A/v_m$, where h is the Planck's constant, N_A the Avogadro's number, and v_m the atomic volume [36]. η_0 was introduced by Eyring [39]. In metallic glasses it corresponds to 4×10^{-5} Pas [22, 23, 94, 65].

Note that η can be replaced with the relaxation time τ, which is also a kinetic property of a liquid. η and τ are proportional to each other according to the Maxwell relation

$$\eta = G_\infty \tau \quad . \tag{2.4}$$

Here G_∞ is the infinite frequency shear modulus [112, 6].

This fragility concept, which was proposed by Angell [5], describes different scaling behaviours of viscosity with temperature [112]. However, several glass formers whose temperature dependence can not be uniformly described as strong or fragile exist. These systems for example are $Gd_{55}Al_{25}Co_{10}Ni_{10}$ and $Pr_{55}Ni_{25}Al_{20}$ [121], as shown in figure 2.6.
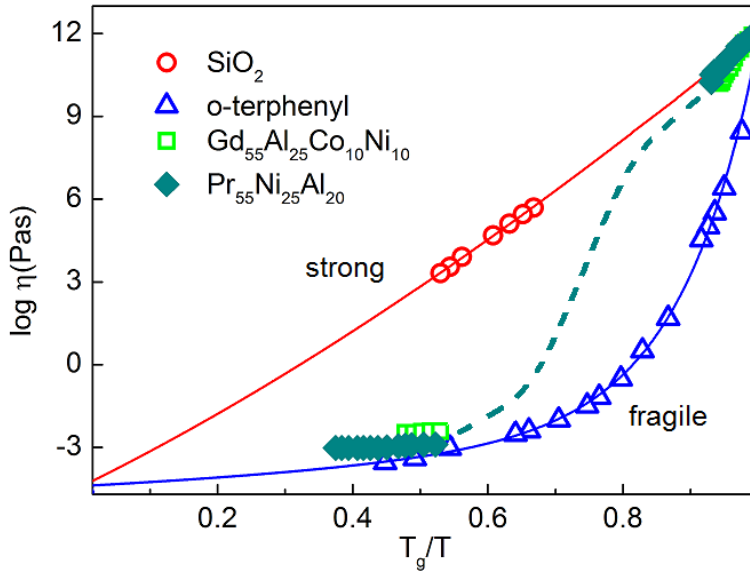
Figure 2.6 – Angell plot of SiO_2 and ortho-terphenyl as representatives of strong and fragile glass formers, respectively. The data is taken from Angell [9]. Additionally, the glass-forming alloys $Gd_{55}Al_{25}Co_{10}Ni_{10}$ and $Pr_{55}Ni_{25}Al_{20}$, which show a discrepancy in their high and low temperature dynamics are depicted [121].

The temperature dependent viscosity of these two metallic glass-forming alloys shows a discrepancy between high and low temperature dependency. They exhibit a rather strong dynamic in

the vicinity of T$_g$, while at higher temperatures they show a more fragile behaviour.

This behaviour indicates a dynamic transition from a fragile state in the melt to a rather strong state in the vicinity of T$_g$, hence a fragile-to-strong crossover. A possible course for such a transition is illustrated in figure 2.6 by the dotted curve. The origin for such a crossover is suspected to be an underlying liquid-liquid transition [114, 62, 122] (see section 2.3.2). However, no direct experimental evidence exists up to now.

Another model using the equilibrium viscosity to describe the deviation from the Arrhenius law is the Adam-Gibbs-equation. It provides an important connection between kinetic properties and thermodynamic quantities [112] and is given by

$$\eta\,(T) = \eta_0 \, \exp\left(\frac{C}{T \, S_c(T)}\right) \quad . \tag{2.5}$$

Here η_0 is a constant, T is the temperature, C is the free energy barrier per particle for cooperative rearrangements, and S$_c$(T) is the configurational entropy [112, 36]. When using equation 2.5 for data fittings, the excess entropy S$_{ex}$ is often used as an approximation instead of S$_c$. This, however, leads to poor results in many cases [41]. According to equation 2.5 the viscous slowdown during undercooling of a liquid is primarily caused by a decrease in configurational entropy. This means that while approaching the glass transition temperature, local potential energy barriers build up and less entropy configurations are available in the undercooled liquid [36].

The Adam-Gibbs equation connects thermodynamic (S$_c$(T)) and kinetic (η(T)) properties with each other. It predicts a change in kinetic properties if thermodynamic properties change and vice versa.

2.3 Phase transitions

2.3.1 First and second order transitions

A phase is a spatial area of homogeneous chemical composition and physical ordering parameter. An ordering parameter, is a criterion which clearly distinguishes one phase from another. For instance particle density characterises either a solid, a liquid or a gas phase. Electrical conductivity, crystal structure, or magnetisation are possible other ordering parameters.

A phase transition is accordingly the transition from one or more phases to one or more other phases. It is induced by a change of state variable such as temperature, pressure, or composition. The dependence of phase changes with respect to state variables are typically depicted in a phase diagram.

A phase transition occurs in order to minimise the free enthalpy or Gibbs free energy, *G* of a thermodynamic system [18]. It is defined as

$$G = U - T\,S + p\,V \tag{2.6}$$

where U is the internal energy, T the temperature, S the entropy, p the pressure, and V the volume of the system. At low temperatures the internal energy of a phase dominates the free enthalpy, while at elevated temperatures the second term (TS) becomes dominant, because entropy is temperature dependent and thus increases with temperature. Therefore, ordered states with a low internal energy are expected at low temperatures, while rather disordered states are expected at higher temperatures.

Phase transitions are distinguished in different orders according to the Ehrenfest classification [18]. For this, a thermodynamic property like enthalpy, entropy, or volume is displayed as a function of the Gibbs free energy in dependence of the variables temperature and pressure. According to Ehrenfest a first-order phase transition is characterised by:

- a continuous transition in $G(T, p)$ and

- a discontinuous transition in the first derivative of $G(T, p)$ with respect to the variables.

This is graphically depicted in the top row of figure 2.7.
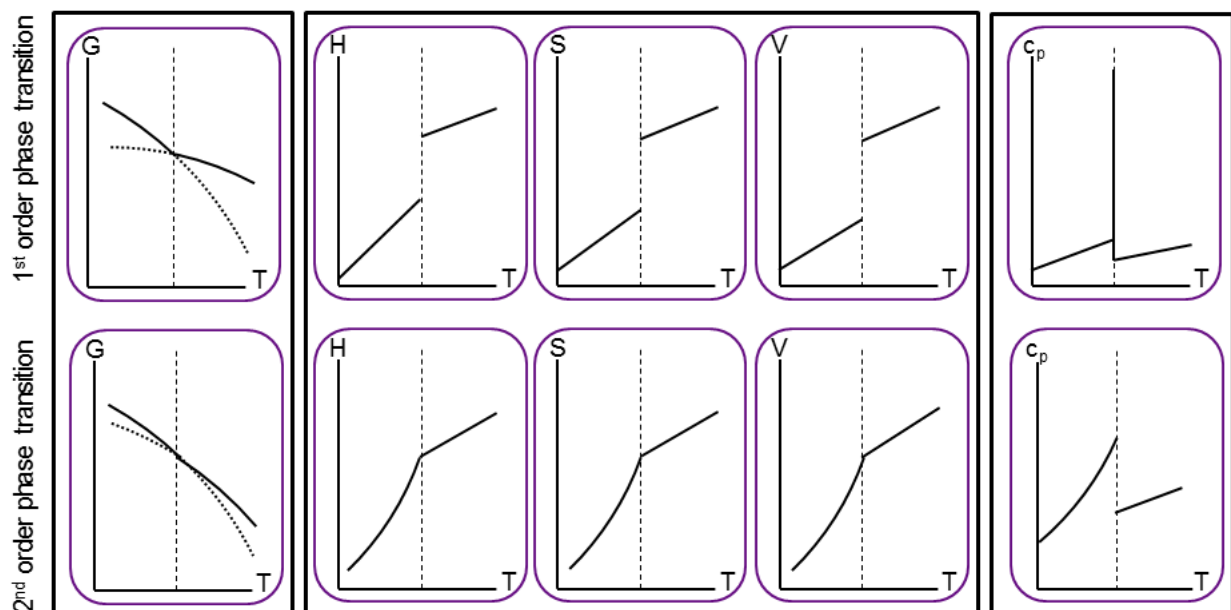
Figure 2.7 – The qualitative course of thermodynamic properties accompanying a first-order (top row) and a second-order (bottom row) phase transitions.

Example for first-order phase transitions are melting, freezing, vaporisation, or condensation processes. A second order phase transition is characterised by:

- a continuous transition in $G(T, p)$ and

- a continuous transition in the first derivative of $G(T, p)$ with respect to the variables and

- a discontinuous transition in the second derivative of $G(T, p)$ with respect to the variables.

This is graphically depicted in the bottom row of figure 2.7. Examples are sublimation and deposition processes or the transition from a ferromagnetic to a paramagnetic phase at the Curie temperature in a ferromagnet.

2.3.2 Liquid-liquid transition

Liquid-liquid transitions (LLTs) (in BMGs) are suspected to be polyamorphic phase transitions between two distinct liquid states of identical compositions but with different entropy and structure [114]. The origin of such proposed LLTs is not well understood and subject of current research [7, 116, 117].

However, experimental evidence for LLTs is difficult to obtain, because most transitions take place in the undercooled liquid state and are therefore masked by crystallisation or the transitions take place at elevated temperatures and/or pressures [114] and are thus experimentally inaccessible.

LLTs were first discovered in network-formers, like SiO_2 [90], BeF_2 [48], or Al_2O_3-Y_2O_3 [4, 42] and molecular liquids, such as water [54], triphenyl phosphite [105], or ortho-terphenyl [9].

Due to the experimental difficulties computer simulations are quite frequently employed to study LLTs. Simulations revealed for instance a strong-to-fragile transition in the network-formers SiO_2 [90, 108, 11] and BeF_2 [48]. In addition, a polyamorphic transition was found in these systems [86, 90, 48]. Moreover, a thermal signal in the form of heat capacity maxima were found in SiO_2 [86, 90] and BeF_2 [48] at temperature far above the melting point.

Yet, also experimentally determined data exists and provides indications for a transition. For example in the form of a polyamorphic transition discovered in Al_2O_3-Y_2O_3 [4, 42] or as thermal signal in the form of heat capacity maxima in BeF_2 [9].

Similar to network-formers also molecular liquids revealed indications for a transition. For instance, a polyamorphic transition was discovered in triphenyl phosphate [105] and ortho-terphenyl [9]. Within the class of molecular liquids water is presumably the most well investigated system. Here, a strong-to-fragile crossover was found by Ito et al. [54]. They showed that water possesses a strong Arrhenius-like temperature dependent relaxation time near T_g in contrast to a fragile behaviour around the melting temperature. Furthermore, a polyamorphic transition was found between a high density state in the melt and a low density state close to T_g [74]. Moreover, water exhibits heat capacity peaks upon cooling at around $240\,K$ and upon heating amorphous ice at around $150\,K$ [7].

Network-formers as well as molecular liquids exhibit either covalent bonds, which are directional bonds with a defined bonding distance or hydrogen bonds, which form networks. Here, an LLT

is usually attributed to a change of local chemical environment of the molecules. This means that for instance in network formers the angle between atoms or the arrangement of molecules in molecular liquids changes. This is also referred to as an order-disorder phenomenon.

Metals, however are characterised by non-(or weak) directional bonds in the melt [114]. Here, interactions between atoms occur only if two atoms come very close and repel each other. Therefore, LLTs were not expected to take place in bulk metallic glasses or at least not due to network-forming properties. Yet, recent studies revealed growing evidence for an LLT in BMGs [71, 64]. Several BMGs showed a drastic changes in the temperature dependency of the viscosity and revealed a more fragile behaviour in the equilibrium melt than at low temperatures in the vicinity of T_g [38, 121]. This finding indicates a strong-to-fragile crossover, as shown in figure 2.6. For the Zr-based BMG Vitreloy 1, a hysteresis-like temperature dependency was even discovered above the melting point [111]. This hysteresis was interpreted as strong-to-fragile transition by the authors. Moreover, heat capacity maxima were found in BMGs [15, 114] and more recently structural changes in the undercooled melt [64, 114, 102]. Yet, the nature of LLTs in BMGs is ambiguous, but will be further investigated within this thesis.

Chapter 3

Electrostatic levitation

Levitation allows containerless processing of objects and enables material investigations without crucible interactions. Hence, contaminations caused by crucible materials do not occur and cannot distort measurements. The absence of contaminations and crucible walls also enables investigations in the undercooled state by avoiding heterogeneous nucleation.

In this study, electrostatic levitation was used to investigate BMGs. This chapter explains the principle of electrostatic levitation (3.1) as well as the influence of gravitation on electrostatic levitation (3.2). Furthermore different electrostatic levitation devices used within this study are introduced and their design to meet individual requirements within electrostatic levitation are explained (3.3).

3.1   The principle of electrostatic levitation

In order to levitate an object electrostatically, this object must be able to carry charges on its surface. In an electric field, this electrically charged object experiences Coulomb force. If the Coulomb force acts in opposite direction to the gravitational force and is sufficiently strong the object is lifted and levitated. The electric field is generated by applying a potential difference between two electrodes arranged vertically above each other. Additional orthogonally arranged electrodes stabilize the object laterally. See figure 3.1.

According to Earnshaw´s theorem electrostatic fields cannot capture charges in a stable equilibrium position [33], because no three dimensional potential minimum exists. To still position a sample in an electrostatic field, the electric field stabilizing the sample position must be actively and continuously controlled in all three spatial directions. This entails a fast sample position detection system, a control unit with an appropriate algorithm to process the position information and high voltage sources connected to each electrode, respectively, adjusting the electrical field for a quasi stable levitation. This makes electrostatic levitation a technically complex and demanding method.

For an active and continuous positioning control, the current sample position must first be detected. The position information is fed to a feedback control algorithm, which calculates the voltages necessary for stabilizing the levitating object. These voltages are then applied to the respective electrodes.

At the beginning of an electrostatic levitation process every object must be initially charged. This is done by induced charging. While the object still sits on its designated starting spot, a potential difference is applied between top electrode and object on its conductive starting spot. This potential difference is increased until enough repelled electrons leave the object so that a positively charged object remains, which eventually lifts off.

During the levitation process charge losses need to be compensated. This can be done by either ultraviolet light or by thermal emission.

In contrast to electromagnetic levitation, electrostatic fields do not heat the object up. Heating is typically achieved by laser. Thus, heating and levitation processes are decoupled. This enables on the one hand access a broad temperature range from room temperature to the temperature at maximum laser power or at most below the boiling point of the object, and on the other hand investigations in the undercooled temperature regime.

Therefore, electrostatic levitation allows materials science investigations. Measurements of density, thermal expansion, viscosity and heat capacity are possible. See chapter 4.

3.2 Gravity in electrostatic levitation

Levitation is based on equilibrating forces. In ground based electrostatic levitation experiments, an object is lifted against gravity by the electrostatic force, F_{ES}, which is defined as charge multiplied by the field strength. The charge, q in metallic objects is freely located on the outer shell of the levitating object, while the field strength, E is given by the applied potential between the electrodes.

Newton's second law defines a force, F_G, which is given by mass, m times acceleration, a [106]. On ground this acceleration is given by the gravitational acceleration. Considering a one-dimensional case, where these forces are balanced, the equilibrium of forces on the object is:

$$F_{ES} = q\, E = m\, a = F_G \tag{3.1}$$

However, this global equilibrium does not hold for every point of the object. Every part of the object experiences a gravitational force, while only surface parts experience an electrostatic force. Hence, a local disequilibrium of forces on the levitating object exists.

Scientific measurement methods, such as e.g. the measurement of viscosity with the oscillating drop technique are based on idealised models. In the case of electrostatic levitation a force free droplet is assumed [89, 46].

In order to approach this model of a force free droplet as far as possible, the local disequilibrium of forces on the levitating object must be reduced. This can only be done by reducing the absolute value of the individual forces to a minimum.

Taking into account equation 3.1, the absolute value of the product $m \cdot a$ can be decreased by taking electrostatic levitation experiments into microgravity. Here, the gravitational acceleration is decreased, while the mass stays constant. Thus, a smaller electrostatic force is required to compensate the force, F_G, (eq. 3.1).

Therefore, an ideal electrostatic levitation experiment should be conducted under microgravity conditions. Since this is difficult to put into action on a regular basis, electrostatic levitation under microgravity conditions should be conducted as a benchmark experiment in order to compare ground based and microgravity experiments and to investigate the influence of gravity on electrostatic levitation.

An electrostatic levitator for use in microgravity conditions is under construction at the Institute of Materials Physics in Space, DLR Cologne [78, 79].

3.3 Electrostatic devices

This section presents different electrostatic levitation devices used within this study. They are located at the Institute of Materials Physics in Space, Cologne. Here, their setup and components as well as their individual adaptation to different experiments are explained.

3.3.1 The electrostatic levitator 1

The first electrostatic levitator introduced here is the ESL 1 [72] It is a stationary device used to process spherical samples of up to 3 mm in diameter to determine parameters for thermal expansion, density, viscosity, and heat capacity.

The central part of every electrostatic levitator is its electrode system. For the ESL 1, it consists of three electrode pairs to cover the three spatial directions. The first pair, top and bottom electrode are arranged one above the other at a distance of 8 mm. They lift the sample up against gravity. The remaining two electrode pairs are side electrodes in the shape of circular ring segments located on the same level as the bottom electrode. They stabilize the sample in its lateral directions. A scheme of the ESL 1 is shown in Figure 3.1.

To generate an electrostatic field a -20 kV to +20 kV amplifier (20-20B 'Trek') and a four channel amplifier (HVA-3B4 'wme') with ±3 kV on each channel are employed. Each channel is assigned to a side electrode, while the -20 kV to +20 kV amplifier serves the top electrode. The bottom electrode is on ground potential.

The sample position is detected via shadow casting. For this two 15 mW He-Ne-positioning lasers
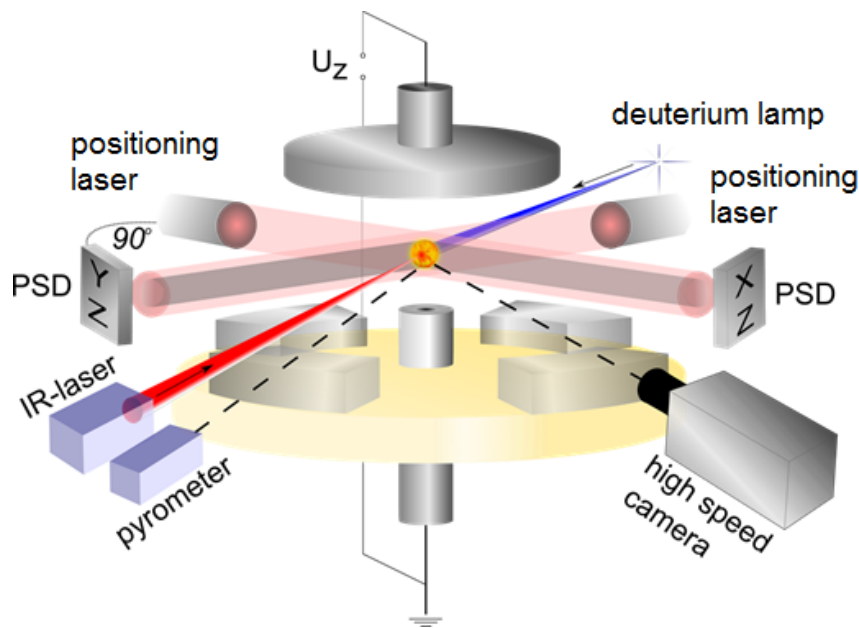
Figure 3.1 – Schematic of the electrostatic levitator 1, Ref. [31]

with a wavelength of 632.8 nm are used. They are arranged in horizontal plane and perpendic-ular towards each other. Optical beam expanders enlarge the respective beam radiation, while infinitely variable iris diaphragms limit the beam diameter to the electrode distance. The lasers each illuminate a (2L10SP 'Sitek') photo sensitive device (PSD), which track the shadow of the sample. The hereby obtained position information is fed into a feedback algorithm and is pro-cessed at 500 Hz. The calculated voltages necessary to stabilise the levitating sample, are then applied to the electrodes. For more information on the algorithm, see reference [72, 73].

During the levitation process the amount of charge on the levitating object is not constant over time. Therefore, possible charge losses need to be compensated. At lower temperatures the lev-itating object is irradiated with ultraviolet light. Here, the photoelectric effect enables positive charging of the object. Energy-rich photons of the ultraviolet light are absorbed by the levitating object and cause electrons to emit. Hence, a positively charged object remains.

At higher temperatures thermionic emission sets in and keeps the sample charged. When heating a levitating object energy is transferred, which enables electrons to overcome their work function and emit, leaving behind again a positively charged object.

In order to compensate the loss of charge on the sample a 150 W deuterium lamp with a wave-length of 115 - 400 nm is used.

For melting samples a 25 W laser at a wavelength of 810 nm is used. The laser output power is controlled manually through an external analogue voltage.

For monitoring the sample's temperature an (IGA 140-TV 'Infratherm' [1]) single colour pyrom-

eter with a spot size smaller than 1 x 1 mm is employed. It measures at wavelengths of 1450 - 1800 nm. The measured temperature range covers 300 - 2000 °C at a sampling rate of 100 Hz.

For determining density and viscosity high speed video diagnostic with an (ultima APX 'Photon') high speed camera is used. It is installed on a guide rail to maintain a exact position. The high speed camera is equipped with an (AF micro-nikkor 'Nikon') lens with a focal length of 200 mm and a (TC-201 'Nikon') teleconverter, enabling close-ups with very good magnification and infinitely variable focusing. Additionally, a (VG9 'Schott') bandpass coloured glass filter with a spectral range of transmission of 485 to 565 nm is installed on the lens. It cuts off laser reflections and radiation and thus enables detecting a sample shadow created by background illumination of a (Mi-150 'Dolan-Jenner Industries') cold light source on the camera chip.

The ESL 1 is also equipped with an additional (DS345 'Stanford Research Systems') function generator, which is used for viscosity measurements. Frequency and amplitude of the sinusoidal signal are adjustable. This signal can be added to the setpoint settings.

The setup of the ESL 1 allows very stable electrostatic levitation of sample masses from 20 to 100 mg and is therefore well suited for density and viscosity measurements.

3.3.2   The mobile electrostatic levitator

The electrostatic levitator introduced in this section was specially designed as a mobile device [59, 60] in order to take it to beam lines for structural and dynamical investigations with neutron and synchrotron experiments.
Therefore the setup contains modifications enabling a more compact design, a special scattering geometry, and particularly for QNS experiments, a long processing time for larger samples.

The mobile ESL has a very compact design. All devices are either installed on top of the vacuum chamber or in separate racks, except for the ultraviolet lamp, which for geometrical reasons is attached directly to the chamber. Here, a (UVS 10/35 'Specs') helium gas discharge lamp was chosen for its compact and small design. This arrangement of equipment allows a vacuum chamber diameter, which can be installed at beam lines.

For scattering experiments a special geometry of the levitation zone is required. A 180° angular range for the incoming and outgoing beam is necessary, where no instruments block the beam. Therefore, and in contrast to the ESL 1 the position detection is realized via mirrors. Two 30 mW positioning lasers with a wavelength of 658 nm are located on top of the chamber. Their beam paths lead to mirrors located below the scattering plane, which guide the beams through the levitation zone and over a second mirror to (2L20SP 'SiTek') PSDs.

In contrast to the ESL 1, the mobile ESL is designed to process larger samples up to 1 g. For QNS experiments a large scattering volume (~ 1 cm^3) is necessary in order to reduce the duration of the experiment to a reasonable timing (few hours) [118, 59]. Therefore the electrode system

Figure 3.2 – Electrode system of the mobile electrostatic levitator.

is adapted, as shown in figure 3.2. The gap between top and bottom electrode is enlarged to 12 mm in total. The high voltage amplifier serving the top electrode is a (PM07071N 'Trek') 40 kV amplifier. This enables a higher field strength than in the ESL 1, so that larger samples can be processed.

Experiments at beam lines require longer processing times than in laboratories. When samples are processed over longer times, they evaporate material. This material condenses on the ground and forms an electrically conductive layer. Once this layer connects two electrodes, the electrostatic field collapses and terminates the experiment. To prevent this from happening isolation gaps around the side electrodes have been introduced, as shown in figure 3.2.

The mobile ESL enables running programmable temperature profiles. For this, it is equipped with two (LM75 'Mergenthaler') 75 W heating lasers with (LH500 'Mergenthaler') laser heads with built-in pyrometers. The lasers operate at a wavelength of 808 nm, while the pyrometers measure at wavelengths of 1650 nm - 1750 nm.
Additionally, the laser output power can also be controlled manually by an external analogue voltage. This enables determining of heat capacities.

Components not mentioned in this chapter are identical to the ones used in the ESL 1.

Within this work synchrotron experiments were performed. The mobile ESL was taken to the German Electron Synchrotron Hamburg, to the PETRA III beam line for structural investigations. Results are presented in chapter 5.

Chapter 4

Materials and methods

4.1 Sample selection and preparation

Samples investigated within this thesis are zirconium-copper (Zr-Cu) and copper-titanium (Cu-Ti) based multicomponent metallic alloys. A complete selection of these BMG formers as well as their respective composition is shown in table 4.1.

In order to further characterise a possible liquid-liquid transition the strong-to-fragile crossover is studied. For this, the fragility and the glass forming ability of the investigated BMGs are systematically varied by the number and amount of components.

In electrostatic levitation experiments these BMGs exhibit different glass forming abilities. Vit106a and Inoue 4 for instance exhibit an excellent glass forming ability. In fact, they undercool to below T_g without crystallising and at suitable sample sizes [1].

Vit106 possess slightly different alloy composition than Vit106a, while Vit105 contains titanium instead of niobium. Investigations of these BMGs will show, whether small variations in composition or substituting individual elements has an influence on thermophysical properties. Vit101, as a copper-titanium based BMG, is of interest because zirconium is only a minor component of the alloy. Diffusion studies of Basuki et al. [13] showed, that zirconium atoms form significantly stronger temporary nearest-neighbour bonds in the melt than other atoms. It is therefore to be investigated whether zirconium plays a central role in the strong-to-fragile crossover.

AMZ4, Inoue 3, and Inoue 4 (again) possess a reduced number of components and therefore a reduced complexity. It is thus possible to study whether the strong-to-fragile crossover is also observed in less complex BMGs. Moreover, two different grades of AMZ4, a high purity and a lower purity version, also referred to as industrial version in the following, allow investigations of impurity elements on thermophysical properties. The two grades are made from different pre-alloys, which differ in purity, mainly in oxygen content, as shown in table 4.2. This question is

---

[1]Inoue 4 can not be vitrified reliably in ESL experiments. It is subject to a by far poorer nucleation statistic than Vit106a, which vitrifies reliably.

trade name	composition	T_g (K)	T_{sol}^{DSC} (K)	T_{liq}^{DSC} (K)
Vit106a	$Zr_{58.5}Cu_{15.6}Ni_{12.8}Al_{10.3}Nb_{2.8}$	670	1089	1113
Vit106	$Zr_{57}Cu_{15.4}Ni_{12.6}Al_{10}Nb_5$	671	1088	1118
Vit105	$Zr_{52.5}Cu_{17.9}Ti_5Ni_{14.6}Al_{10}$	663	1066	1087
Vit101	$Zr_{11}Cu_{47}Ti_{34}Ni_8$	676	1108	1158
high purity AMZ4	$Zr_{59.3}Cu_{28.8}Al_{10.4}Nb_{1.5}$	726	1128	1186
industrial AMZ4	$Zr(705)_{60.8}Cu_{28.8}Al_{10.4}$	668	1130	1192
Inoue 4	$Zr_{65}Cu_{17.5}Ni_{10}Al_{7.5}$	628	1101	1165
Inoue 3	$Zr_{60}Cu_{25}Al_{15}$	671	1157	1182

Table 4.1 – Sample selection of the BMGs investigated within this thesis. Glass transition-, solidus-, and liquidus temperatures are determined within this work by differential scanning calorimetry (see section 4.4). Heating rates are $q_H = 0.166\,K/s$.

of interest, since the oxygen content of the starting materials is scaled to the costs involved. The manufacturing costs for these two quality grades differ by a factor of 9.5.

Sample preparations were carried out at the University of the Saarland, in the Chair of Metallic Materials of Prof. Dr. Ralf Busch. Here, crystalline master alloys were prepared by arc-melting of elemental metals having purities ranging from 99.9 % to 99.999 %. To produce glassy sample compositions, these master alloys were re-melted and cast into water-cooled copper molds under high-purity argon atmosphere. The resulting sample rods weigh between 4 and 8 g, depending on the rod size. For more details see [47].

ESL samples were cut from these rods and re-melted in an arc-furnace under argon atmosphere to spherical shapes at the Institute of Materials Physics in Space, Cologne.

Parts of this thesis deal with comparative measurements of the viscosity (chap. 5.1). In order to

element or price	Zr crystal bar [3]	Zr R60705 [2]
oxygen (ppm)	70	10300 ($\approx 1\,at\%$)
hydrogen (ppm)	25	4540
nitrogen (ppm)	20	1630
carbon (ppm)	n/a	3810 ppm
iron & chromium (ppm)	300	3280
niobium (ppm)	50	30000 ($\approx 3\,at\%$)
price (€/kg)	900	95

Table 4.2 – Manufacturer's specifications for zirconium grades as used in high purity AMZ4 made of Zr crystal bars and low purity AMZ4 made of Zr R60705 [44].

exclude any influence from the sample material on these measurements, sample compositions were produced and investigated in batches. Thereby, identical starting materials are ensured.

4.2 Measurement methods using electrostatic levitation

This section explains different measurement methods used in combination with electrostatic levitation. It deals with the measurement principles as well as with the analysis of the measured data and the corresponding error estimations.

4.2.1 Temperature measurement

Time-resolved temperature measurements are part of each measurement method used within this work. In addition, they are used to determine the specific heat capacity.
Temperatures of levitating droplets are contactlessly recorded using single colour pyrometry, as described in chapter 3.1 and 3.2. Here, the temperature of a droplet's surface is determined according to its thermal radiation.

Every object with temperatures above absolute zero emits thermal radiation in form of electromagnetic radiation. This is described by Planck's law [30], which further states that the radiation at a definite temperature is given by spectral radiance and intensity as function of wavelengths as depicted in figure 4.1.
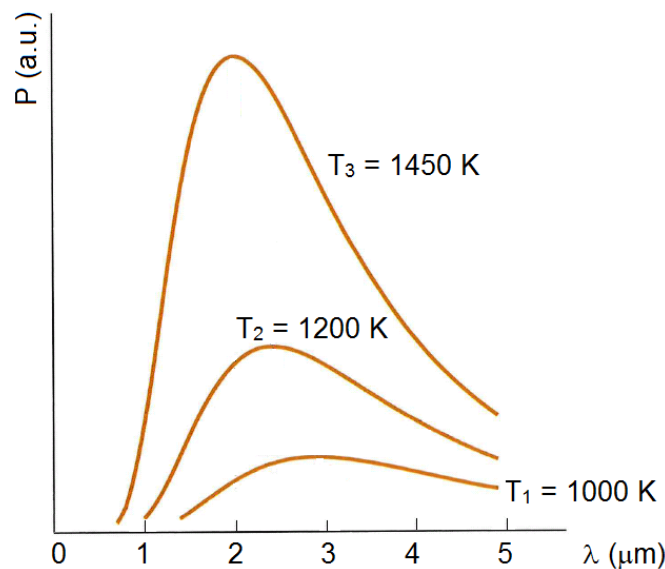
Figure 4.1 – Planck's radiation spectrum: Radiation power of a black body as function of the wavelength for different temperatures [106].

The operating principle of a pyrometer in turn uses the Stefan-Boltzmann law in order to deduce the temperature from the spectral radiation. This law reads

$$P = \sigma \cdot A \cdot T^4 \tag{4.1}$$

in its simplest form, where P is the radiation power, σ the Stefan-Boltzmann constant, A the surface area, and T the absolute temperature. Equation 4.1 holds for idealised black-bodies, whose emissivity is 1 over the entire spectrum. The degree of emissivity specifies how much thermal radiation a grey-body in comparison to a black-body emits. In order to apply equation 4.1 to grey-bodies the emissivity, ε needs to be taken into account.

$$P = \varepsilon(\lambda, T) \cdot \sigma \cdot A \cdot T^4 \tag{4.2}$$

Metallic melts, however, are not pure grey-bodies, because their emissivity depends not only on temperature and surface texture, but also on the wavelength. A wavelength dependent emissivity changes the radiation distribution. This causes an additional temperature dependency and as a result the total radiation power is no longer proportional to the fourth power of the absolute temperature. The hemispherical total emissivity of a body with such frequency independent emissivity has to be determined individually. However, only the dependency of the spectral range in which the pyrometer measures is of interest, thus 1.45 - 1.8 μ (chap. 3.3.1). Here, no significant changes in the emissivity are known and it is therefore considered to be wavelength independent. Furthermore, the emissivity of the liquid state is assumed to be temperature independent. The emissivity is a material-dependent parameter. For Zr-based alloys, as used within this work, ε = 0.28 is a good approximation. Possible temperature offsets to the real temperature are corrected via a clearly defined point, such as the liquidus or solidus temperature. This correction is carried out for every temperature measurement as follows:

$$T_{real} = \left(\frac{1}{T^{Pyro}} + \frac{1}{T^{DSC}_{sol/liq}} - \frac{1}{T^{Pyro}_{sol/liq}} \right)^{-1} \tag{4.3}$$

Here T_{real} is the corrected temperature, T^{Pyro} is the temperature recorded by the pyrometer, $T^{DSC}_{sol/liq}$ is the solidus or liquidus reference temperature determined from DSC measurements within this work (chap. 4.4), and $T^{Pyro}_{sol/liq}$ the solidus or liquidus temperature determined from the measured time-temperature profile of the pyrometer.

Figure 4.2 shows an example, how a liquidus temperature is determined from a measured pyrometer scan (left) and a corresponding DSC measurement (right). The respective temperature is determined by creating two tangents and determining the intersection point.
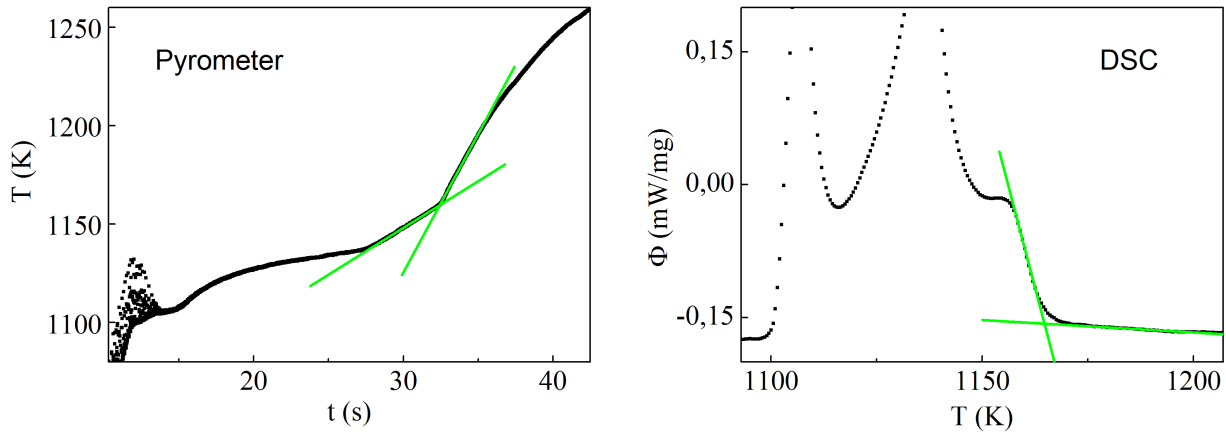
Figure 4.2 – (left) Melting plateau of a time-temperature profile obtained by pyrometry. The liquidus temperature, T_{liq}^{Pyro} is determined via the intersection point of applied tangents.
(right) Melting peak of a DSC scan. The reference liquidus temperature, T_{liq}^{DSC} is determined by the intersection point of applied tangents.

Measuring errors

The temperature uncertainty is affected by the precision of the pyrometer and the temperature correction. The accuracy of the pyrometer below 1500 °C is given with 0.3 % of the measured value plus 1 °C [1], which for instance results in an uncertainty of 4.6 °C at 1200 °C . The repeatability, in contrast is given with 0.1 % of the measured value plus 1 °C . This results in a low noise level of 2.2 °C at 1200 °C .

The temperature uncertainty after correction is affected by the accuracy of the solidus or liquidus temperature ($T_{sol/liq}^{Pyro}$) determined from the pyrometer scan and the corresponding reference temperature ($T_{sol/liq}^{DSC}$). $T_{sol/liq}^{Pyro}$ is determined from either solidus or liquidus temperature depending on which is more pronounced. The precision of this temperature depends on the course of the time-temperature profile. An increased noise level, for instance caused by slightly different emissivities of different phases co-existing during melting (see fig. 4.2 in the vicinity of 1100 K) can distort this temperature course. The solidus or liquidus temperature of the pyrometer can typically be determined within a maximum error of ± 2.5 K. The temperature uncertainty of the DSC reference temperature is given with ± 4 K up to 1373 K (section 4.4). However, consistent reference temperatures were used throughout this work for each sample system. Based on these uncertainties the corrected absolute temperature is assumed to deviate by ± 10 K. This uncertainty holds for all temperature dependent measurement results presented within this work. For reasons of clarity the temperature uncertainty is not always displayed. But, note that the relative accuracy of individual measurements is not affected by this.

4.2.2 Specific heat capacity at constant emissivity

The specific heat capacity is a thermodynamic property. It can be derived from a time-temperature profile of a free radiation cooling experiment performed in an ESL.

Under the assumption, that a cooling process occurs purely due to radiation loss the Stefan-Boltzmann law (eq. 4.2) can be used to derive the specific heat capacity over emissivity. All parameters required for this are either known or can be obtained from the cooling curve.
The radiation power, P as given in equation 4.2 is defined as thermal energy per time. Thermal energy, however can also be described as amount of heat. The release of heat leads to a decrease in temperature. This amount of heat dissipated is proportional to the change in temperature and the mass of the material as described by

$$\Delta Q = c_p \cdot m \cdot \Delta T \tag{4.4}$$

where ΔQ is the amount of dissipated heat, m the mass, and ΔT the change in temperature. The proportionality constant, c_p is the specific heat capacity of a material. Deriving this equation after time and combining it with equation 4.2 leads to

$$P = \frac{dQ}{dt} = c_p \cdot m \cdot \frac{dT}{dt} = -\sigma \cdot A \cdot \varepsilon \cdot \left(T^4 - T_0^4\right) \; . \tag{4.5}$$

Here $\frac{dT}{dt}$ is the cooling rate of an ESL experiment, σ the Stefan-Boltzmann constant, A the sample surface area, ε the emissivity of the sample, T the sample temperature, and T_0 the room temperature. Surface area and mass are determined via the sample radius, assuming a spherical shape. Equation 4.5 is then rearranged to describe the quotient of specific heat capacity and emissivity as

$$\frac{c_p}{\varepsilon} = \frac{-\sigma \cdot A \cdot (T^4 - T_0^4)}{m \cdot \frac{dT}{dt}} \; . \tag{4.6}$$

In order to obtain the derivative of the cooling curve its data is reduced and averaged. Otherwise the noise of the pyrometer signal causes large scattering in the obtained heat capacity result. This is particularly important at lower temperatures where the cooling rate is smaller and more data points per time are available. This high data rate, however enables not loosing the time resolution.

Figure 4.3 (left) shows the time-temperature profile of a heating and free radiation cooling ESL experiment with reduced and averaged data upon cooling.

The resulting quotient of heat capacity and emissivity is presented in figure 4.3 (right). Here, c_p/ε was determined several times from the same cooling curve (left), but with different reduction rates. The quality of the c_p/ε signal depends mainly on the reduction rate and averaging process. Too many data points per time lead to scattering (see fig. 4.3 (right) 400 data points), while too few data points result in inaccuracy (see fig. 4.3 (right) 15 data points). An appropriate reduction rate was found to be on average one data point per second (see fig. 4.3 (right) 65 data points).
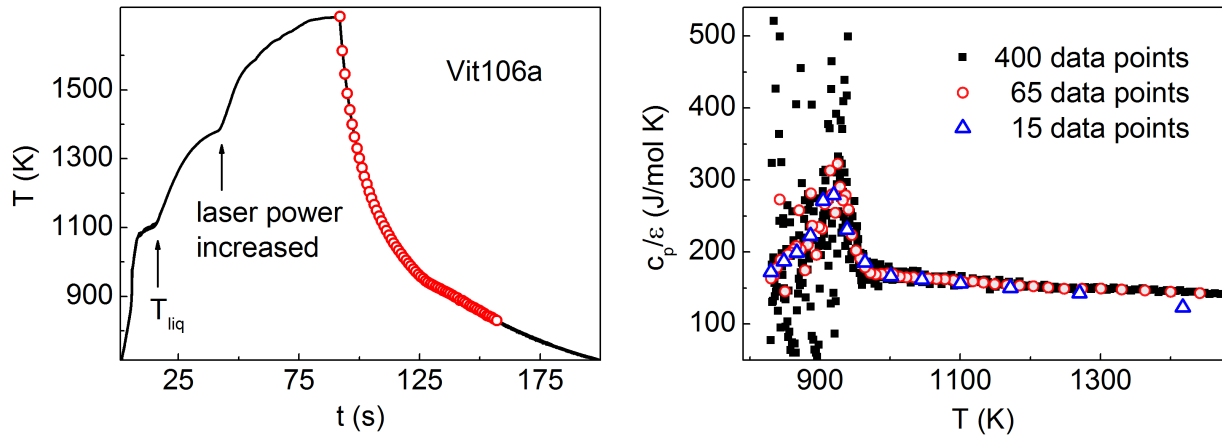
Figure 4.3 – (left) Time-temperature profile of a heating and free radiation cooling ESL experiment with reduced and averaged data (red circles) upon cooling.
(right) Different c_p/ε_T values determined from different numbers of reduced data points (DP (per 65 s)) of the cooling curve shown left.

ESL cooling experiments have the advantage of allowing access to the undercooled state. This enables determining the c_p/ε signal throughout the undercooled region until the onset of a recalescence or even down to below the glass transition temperature, where conventional crucible based methods have no access.

4.2.3 Density measurement

Density measurements are performed on levitating liquid samples. For this purpose, the volume of a sample in dependence of its temperature is calculated via its projected area. By employing the sample mass the temperature dependent density can be obtained.

During a density measurement a levitating liquid sample is illuminated by a backlight. Its shadow is recorded from opposite the light source with a high speed camera. At the same time the sample temperature is tracked by a pyrometer. An example of such a recorded image is shown in figure 4.6 b).

All captured images are analysed in terms of their sample volume using the in-house software Dibble Lights [20]. Here, an edge detection is performed, where pixels with a certain grey value are recognised as edge pixels. These pixels are fitted with a polynomial. This allows a virtual refinement with a spacial resolution of less than one camera pixel. By integrating this two-dimensional fit over its volume, a three-dimensional pixel volume is determined. For this analysis an axial symmetry of the sample around its vertical axis is assumed. This condition only holds for liquid samples.

In order to translate the pixel volume into a real volume, (four) reference measurements with calibrated steel spheres (ball bearings) of known radius and thus volume are made. The pixel volume of the reference spheres is determined under identical setup conditions as for the sample. This is done to minimize errors arising from a position uncertainty. The real volume, V_{real} is then calculated by

$$V_{real} = \frac{1}{6} \cdot \pi \cdot d^3 = \frac{4}{3} \cdot \pi \cdot r^3 \qquad (4.7)$$

where d is the diameter of the reference sphere. Thereby, a relation between pixel and real volume is obtained, which is distinct for each density measurement.

Lastly, the sample mass is used to derive the density according to

$$\rho(T) = \frac{m}{V(T)} \ . \qquad (4.8)$$

This data is then synchronised with the temperature data of the pyrometer, giving a temperature dependent density.

For density measurements certain specifications have been realised in order to optimise the measurement method. A cold light source with a high intensity around 500 nm is used as background illumination to increase the contrast during shadow casting. This wavelength is of particular interest, since the camera is equipped with a bandpass filter, which permits only light with a wavelength of 485 to 565 nm. This is done, because on the one hand the camera lens has a refraction index, which is wavelengths dependent and on the other hand, this improves the sharp definition of the image and cuts out possible reflections from positioning lasers and thermal radiation from the sample, especially at higher temperatures.

The camera records 250 frames per second. During analysis, 25 frames are averaged to one frame. The information of this frame is converted into one density data point. This is done to minimize noise, which occurs due to slight oscillations or vibrations of the sample. The temperature data, which is tracked at 100 Hz is interpolated and synchronized accordingly. This is necessary to minimize noise from the pyrometer signal and to adjust the temperature to the individual density data points. Hence, the step size between two density data points is determined by the sample's cooling or heating rate.

Density measurements on levitating samples are performed in the ESL 1 (chap. 3.3.1). Here, very stable levitations over a broad temperature range and throughout the undercooled state are feasible.

Measuring errors

Density is defined as mass per volume (see equation 4.8). The uncertainty in density is thus, determined by theses two parameters and calculated according to a Gaussian error propagation,

as

$$\Delta\rho = \sqrt{\left(\frac{\delta\rho}{\delta m}\,\Delta m\right)^2 + \left(\frac{\delta\rho}{\delta V}\,\Delta V\right)^2} \qquad (4.9)$$

$$\Delta\rho = \sqrt{\left(\frac{1}{V}\,\Delta m\right)^2 + \left(-\frac{m}{V^2}\,\Delta V\right)^2} \qquad (4.10)$$

$$\Delta\rho = \sqrt{\left(\frac{\rho}{m}\,\Delta m\right)^2 + \left(-\frac{\rho}{V}\,\Delta V\right)^2} \qquad (4.11)$$

$$\left(\frac{\Delta\rho}{\rho}\right)^2 = \left(\frac{\Delta m}{m}\right)^2 + \left(\frac{\Delta V}{V}\right)^2 . \qquad (4.12)$$

According to equation 4.12 the uncertainty in density is determined by the deviation in mass and volume in relation to the respective absolute value.

The deviation in mass is determined by taking the weight of every sample before and after an experiment. In levitation experiments mass loss occurs due to evaporation of sample material at higher temperatures. Care has been taken to reduce mass loss during density experiments to a minimum. Measurements exceeding a mass loss of 1 % of the initial sample mass are not considered in this work. This, is done in order to reduce the error arising from an uncertainty in mass as well as to ensure an uniform and consistent sample composition as given in table 4.1. Typical mass losses were found to be less than 0.5 % of the initial weight. With the assumption of a maximum mass loss of 0.5 %, the uncertainty in $\frac{\Delta m}{m}$ is estimated to be $\leq 0.5\,\%$.

Hence, the deviation in mass plays a minor effect on the uncertainty in density. In the following the uncertainty in density due to an uncertainty in determined sample volume is considered.

For this, the camera setup is effectively considered, as illustrated in figure 4.4.

Here, b is the image distance and and g is the object distance between lens and sample. For density measurements the camera is equipped with an endocentric lens system with a focal length of 200 mm and a teleconverter with a 2:1 magnification.

The ratio of sample size, S on the focal plane to image size, I on the image plane is given by

$$S = \frac{g}{b}\,I . \qquad (4.13)$$

While the length, b is fixed by the lens, the object or working distance, g is nominal within a certain range. The minimal working distance is limited by the dimensions of the vacuum chamber, while the maximum distance is limited by the focus of the lens. The optical magnification is given by the ratio $\frac{g}{b}$. Although, the real size of the sample can in principle be obtained by measuring $\frac{g}{b}$ in this measurement setup it is not determined by dimensions, but by calibration with the reference spheres, as discussed in the following.

The sample volume is determined by measurements with reference spheres, as explained in section 4.2.3. Calibrated ball bearing made of steel and with known radius and a deviation of a
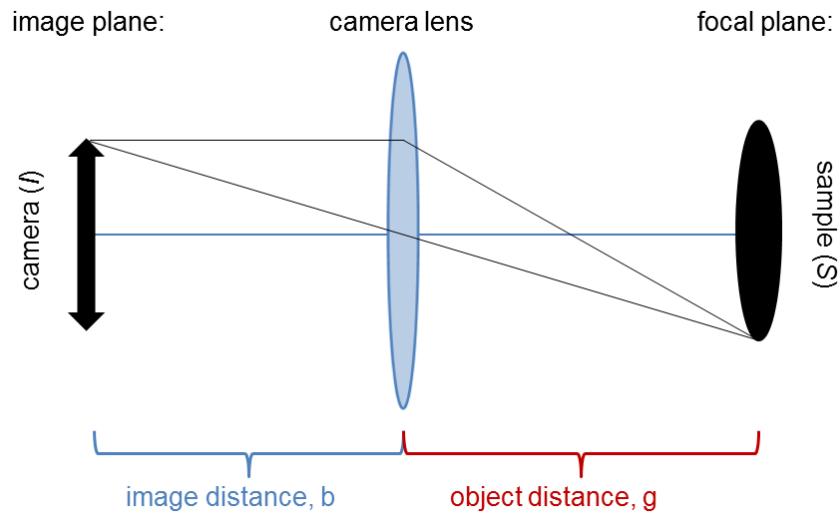
Figure 4.4 – Experimental setup of density measurements performed within the ESL1 (chap. 3.3.1). The setting is chosen in order to minimize errors arising from uncertainties in magnification and sample position. The camera system in this figure is simplified.

maximum of $0.5\,\mu$m in radius are used for this. Their pixel volume is determined exactly as in a density measurement using the in-house software Dibble Lights. But, since radius and thus volume are known, the reference spheres provide a linear relation of real volume to pixel volume. An example of this linear relation is shown in figure 4.5.
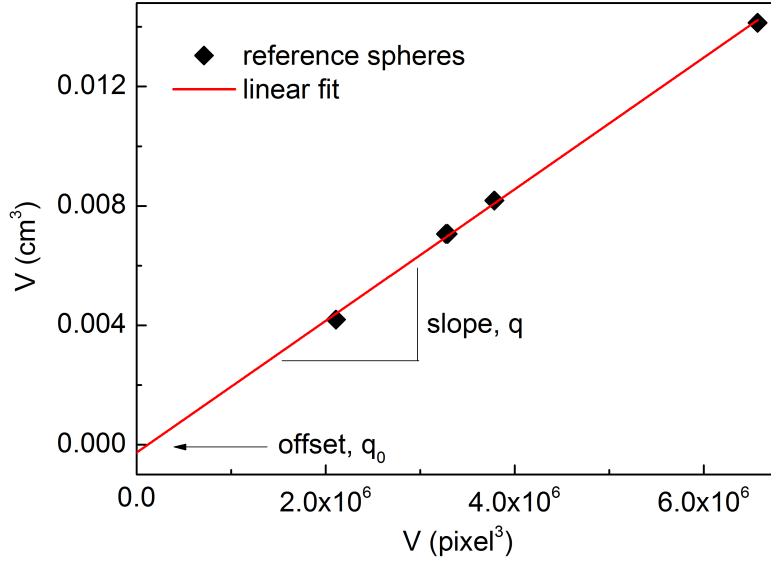
Figure 4.5 – Measurement of four reference spheres (ball bearings) for the density measurement of Vit106a presented in figure 5.7 (right). The linear relation obtained from real and pixel volume of the ball bearings was used to calibrate the density measurement.

The sample volume, V_{sample} is therefore given by

$$V_{sample} = q_0 + q \cdot V_{pixel} \, . \tag{4.14}$$

Here q_0 is the offset in y-axis, q the slope of the linear relation of pixel to real volume, and V_{pixel} the pixel volume of the reference spheres. In order to determine the uncertainty in sample volume, q_0, q, and V_{pixel} are considered independent of each other and their individual squared uncertainties are calculated in an error propagation.

$$\Delta V_{sample} = \sqrt{\left(\frac{\delta V_{sample}}{\delta q_0} \Delta q_0 \right)^2 + \left(\frac{\delta V_{sample}}{\delta q} \Delta q \right)^2 + \left(\frac{\delta V_{sample}}{\delta V_{pixel}} \Delta V_{pixel} \right)^2} \tag{4.15}$$

$$\Delta V_{sample} = \sqrt{\left(1 \cdot \Delta q_0 \right)^2 + \left(V_{pixel} \cdot \Delta q \right)^2 + \left(q \cdot \Delta V_{pixel} \right)^2} \tag{4.16}$$

$$\Delta V_{sample} = \sqrt{\left(\Delta q_0 \right)^2 + \left(\frac{V_{sample} - q_0}{q} \Delta q \right)^2 + \left(\frac{V_{sample} - q_0}{V_{pixel}} \Delta V_{pixel} \right)^2} \tag{4.17}$$

$$\left(\frac{\Delta V_{sample}}{V_{sample}} \right)^2 = \left(\frac{\Delta q_0}{V_{sample}} \right)^2 + \left(\frac{V_{sample} - q_0}{V_{sample}} \right)^2 \cdot \left(\left(\frac{\Delta q}{q} \right)^2 + \left(\frac{\Delta V_{pixel}}{V_{pixel}} \right)^2 \right) \, . \tag{4.18}$$

Based on equation 4.18 the influence of the individual terms on the uncertainty in sample volume is estimated. This is done on the example of Vit106, whose density measurement is presented in figure 5.7 (right).

In this case, Δq_0 is $2 \, x \, 10^{-5} \, \text{cm}^3$ and V_{sample} is $4 \, x \, 10^{-3} \, \text{cm}^3$, which corresponds to a spherical volume of $2 \, \text{mm}$ in diameter. Thus, the resulting value of the first term of equation 4.18 is 0.005 and 0.995 for the second term. This means that the first term contributes $0.5 \, \%$ to the total volume uncertainty and the second term contributes $1 \, \%$ (times the factor of the last term).

Now, the last term of equation 4.18, which consists of two summands is considered. In the calibration measurement of the Vit106 example used Δq is $1 \, x \, 10^{-11} \, \text{cm}^3/\text{pixel}$ and q corresponds to $4 \, x \, 10^{-9} \, \text{cm}^3/\text{pixel}$. This leads to a value of 0.0025 for the quotient $\frac{\Delta q}{q}$. V_{pixel} is the average amount of pixels detected when analysing 250 pictures of a single reference sphere. ΔV_{pixel} is the maximum deviation from V_{pixel}. Values for ΔV_{pixel} and V_{pixel} are in the order of $10^3 \, \text{pixel}^3$ and $10^6 \, \text{pixel}^3$, respectively. This results in a quotient of $\frac{\Delta V_{pixel}}{V_{pixel}} \approx 0.001$. Since, this value is so small $(0.1 \, \%)$ it is neglected in the following. Therefore, the last term of equation 4.18 is reduced to $\frac{\Delta q}{q}$. This term however, is multiplied with the previous term, which corresponds to a value of approximately $1 \, \%$. Since this makes no different mathematically the term $\frac{V_{sample} - q_0}{V_{sample}}$ is neglected. Therefore, this estimation lead to an uncertainty in sample volume influenced by

$$\left(\frac{\Delta V_{sample}}{V_{sample}} \right)^2 = \left(\frac{\Delta q_0}{V_{sample}} \right)^2 + \left(\frac{\Delta q}{q} \right)^2 . \tag{4.19}$$

According to this equation and the previous estimations the uncertainty in volume contributes approximately $0.75 \, \%$ to the total error.

The discussion above shows that the uncertainty in density is influenced by deviations in mass and sample volume. The uncertainty is however, mostly dominated by the uncertainty in sample volume, which in turn attributes to the accuracy of the calibration measurements. For all the measurements in this study, the uncertainty in density is quire similar and corresponds to approximately $1 \, \%$ of the absolute density. For reasons of clarity, error bars presented within this work are only given for the lowest temperature. This is done, because the largest error bars are found at the highest density.

The uncertainty calculation performed so far holds under the assumption that sample and reference spheres levitate in the exact same spot. However, small deviations in position, Δg are possible.

As stated earlier, the sample size can be described in terms of image distance to object distance. A deviation in sample size can thus be described as

$$S = \frac{\Delta S}{S_{average}} = \frac{\frac{\Delta g}{b} \cdot I}{\frac{g}{b} \cdot I} = \frac{\Delta g}{g} . \tag{4.20}$$

According to equations 4.20 the maximum uncertainty in sample position is limited by the deviation in sample position with respect to the object distance. Note, that the deviation in sample

position is limited by the setup of the electrode system of the ESL 1. It is designed in a way that the maximum deviation from the centre position, which is defined by a vertical axis through the geometrical middle of the bottom electrode, is $\pm 1.5\,\text{mm}$ in each direction. Position deviations within this magnitude still allow a stable levitation. Any deviation greater than that will cause an unstable levitation, which is not suitable for density measurements (see fig. 5.20). Therefore, a maximum position deviation of $\Delta g \leq 3\,\text{mm}$ is assumed. For a minimum working distance of 300 mm the deviation of the absolute density caused by an uncertainty in sample position is not larger 1 %. Experiments within this thesis are conducted with a working distance of around 350 mm.

4.2.4 Specific volume

The specific volume of a material is the ratio of its volume to mass. It is defined as the reciprocal of the material's density.

$$V_c = \frac{V}{m} = \frac{1}{\rho} \tag{4.21}$$

Here V_c is the specific volume, V the volume, m the mass and ρ the density.

4.2.5 Thermal expansion coefficient

In this section, it is shown that temperature dependent density measurements of the equilibrium melt and the undercooled state can be used to derive the thermal volume expansion coefficient of this very temperature region.

Thermal expansion describes the change of a body in length, area, or volume caused by a change in temperature. Its characteristic parameter, the thermal expansion coefficient, a is thus given in dependence of temperature or for a certain temperature range.

The volumetric thermal expansion coefficient, α of a liquid (or solid) is defined as

$$\alpha = \frac{\Delta V}{V_0 \Delta T} = \frac{V(T) - V_0}{V_0 \Delta T} \,. \tag{4.22}$$

Here $V(T)$ is the volume in dependence of temperature, V_0 the volume at 0 K, and ΔT the change in temperature. This equation can be rearranged to

$$V(T) = V_0 + \alpha V_0 (T - T_0) \tag{4.23}$$

where T is the temperature and T_0 is the temperature at 0 K. Volume in turn is defined as

$$V(T) = \frac{m}{\rho(T)} \tag{4.24}$$

where $V(T)$ is the temperature dependent volume, $\rho(T)$ the temperature dependent density, and m the mass. With this relation the volume expansion in dependence of temperature, $V(T)$, as

given in eq. 4.23 can be rewritten in terms of density

$$\frac{m}{\rho(T)} = \frac{m}{\rho_0} + \alpha \frac{m}{\rho_0} (T - T_0) \tag{4.25}$$

$$\frac{1}{\rho(T)} = \frac{1}{\rho_0} + \alpha \frac{1}{\rho_0} (T - T_0) \tag{4.26}$$

$$\frac{\rho(T)\,\rho_0}{\rho(T)} = \frac{\rho(T)\,\rho_0}{\rho_0} + \alpha \frac{1}{\rho_0} (T - T_0)\,(\rho(T)\,\rho_0) \tag{4.27}$$

$$\rho_0 = \rho(T) + \alpha\,\rho(T)\,(T - T_0) \tag{4.28}$$

$$\rho(T) = \frac{\rho_0}{1 + \alpha\,(T - T_0)} \tag{4.29}$$

Density is a temperature dependent property. A change in temperature is described as

$$\rho(T) = \rho_0 + \Delta\rho(T) \tag{4.30}$$

with ρ_0 being the density at $0\,\mathrm{K}$. This relation is then used to rewrite equation 4.29

$$\rho(T) = \rho_0 + \Delta\rho(T) = \frac{\rho_0}{1 + \alpha\,(T - T_0)} \tag{4.31}$$

$$\rho_0 = (\rho_0 + \Delta\rho(T)) \cdot (1 + \alpha\,(T - T_0)) \tag{4.32}$$

$$\rho_0 = \rho_0 + \Delta\rho(T) + \rho_0\,\alpha(T - T_0) + \Delta\rho(T)\,\alpha(T - T_0)\,. \tag{4.33}$$

Now, relation 4.30 is used again, to simplify equation 4.33 as follows

$$\rho_0 = \rho(T) + \rho_0\alpha(T - T_0) + \Delta\rho(T)\,\alpha(T - T_0)\,. \tag{4.34}$$

For small changes in density ($\Delta\rho \ll \rho$) terms of higher order can be neglected. Such small changes are in the range of $a \approx 10^{-5} - 10^{-6}$ for the expansion coefficient and $\Delta T \leq 10^{3}$ for the temperature. These values result in $\Delta\rho < 1\%\rho_0$. Hence, the last term of equation 4.34 is neglected and the (volumetric) thermal expansion coefficient is described in terms of a temperature dependent density as

$$\rho(T) = \rho_0 - \alpha\rho_0(T - T_0)\,. \tag{4.35}$$

This description of the (volumetric) thermal expansion coefficient differs from the volume and temperature dependent description (eq. 4.22) only with respect to the $\pm$ sign.

$$\alpha = \frac{\rho(T) - \rho_0}{\rho_0(T - T_0)} = \frac{\Delta\rho}{\rho_0\,\Delta T} \tag{4.36}$$

4.2.6 The oscillating drop technique for viscosity measurements

The oscillating drop technique is a containerless method to determine the viscosity of a liquid. It utilizes the fact, that viscosity is understood as internal friction and that hence, a freely oscillating liquid sphere is damped by precisely this property.

In the oscillating drop method [89], a surface oscillation is induced to a freely levitating droplet. Upon stopping the excitation of this oscillation, the free damping behaviour is recorded and analysed in order to determine the viscosity.

The decay behaviour of an induced oscillation is described by Lamb [63] as

$$\tau_{(n)} = \frac{1}{(n-1)(2n+1)} \cdot \frac{\rho\, r_0^2}{\eta} \tag{4.37}$$

where τ_n is the decay constant of the n-th oscillation mode, ρ the density, r_0 the radius of the droplet when it assumes a spherical shape, and η the melt viscosity. For a $n = 2$ mode, as used with the current setup the above equation simplifies to

$$\tau_{(n=2)} = \frac{\rho\, r_0^2}{5\eta} \;. \tag{4.38}$$

The relation between viscosity and decay behaviour, as given in two equations above, includes following assumptions [63, 53]:

- the sample levitates free of forces

- the sample assumes a spherical shape before and after the induced oscillation

- the sample exhibits only laminar flow

These conditions are never entirely fulfilled in ground based experiments. However, in ESL experiments no turbulent flow is induced inside the sample by the electrostatic field. Also, samples are sufficiently small to maintain a near spherical shape, because of their surface tension. Therefore, in electrostatic levitation the above conditions are considered to be approximately fulfilled.

A surface oscillation is excited by a single frequency, near the droplets resonance frequency (eigenfrequency). The oscillation should have small deflections of a maximum of 10 % of the average radius [14]. For the current setup an n = 2 and m = 0 mode [89] is the simplest mode to excite (and analyse). This oscillation is an axisymmetric elongation or compression along the vertical axis. It is realised by an additional sinusoidal voltage, which is added to the levitation voltage, U_z (see chap. 3.3.1). An example of a sample shadow as recorded upon different oscillation stages is shown in figure 4.6.

Note, that the maximum vertical elongation (fig. 4.6 a)) during an oscillation occurs along an axis, while the minimum vertical elongation (fig. 4.6 c)) along the vertical axis is also a maximum elongation along the horizontal plane. Therefore, the elongation in vertical direction (fig. 4.6 a)) appears more pronounced than the elongation in horizontal direction (fig. 4.6 (c)).
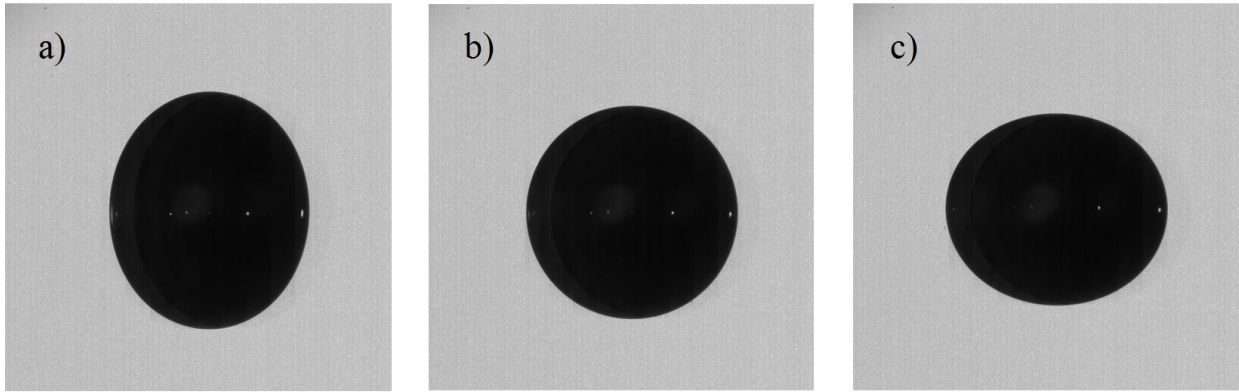
Figure 4.6 – Sample shadows as recorded upon different stages of an n = 2 and m = 0 oscillation mode. a) Maximum elongation along the vertical semi-axis. b) Initial spherical state without excitation c) Minimum elongation along the vertical semi-axis.

4.2.7 Viscosity measurement

Viscosity measurements conducted within this work are performed using the oscillating drop technique in combination with electrostatic levitation. This combination allows temperature dependent viscosity measurements of liquids over a broad temperature range.

The oscillation decay behaviour is recorded via shadow casting. For this, the levitating sample is illuminated by a backlight and its shadow is recorded from opposite the light source with a high speed camera. The temperature is tracked using a pyrometer. This part of the setup is identical to a density measurement.

The liquid sample is excited by an additional sinusoid voltage, which is added to the vertical levitation voltage, U_z (see figure 3.1). The oscillation mode is determined by the excitation frequency and amplitude. With the correct oscillation mode set, the excitation is stopped and the damping is recorded by the camera at 2000 Hz. These two processes are synchronised in order to start them simultaneously. The frame rate ensures accurate and continuous tracking of the decay behaviour. During the oscillation and decay process the temperature is kept constant.

All captured images are analysed in terms of their change in semi-axes over time. For this the in-house software TeVi is used [93, 115]. Here, an edge detection is performed, where pixels containing a certain grey value are analysed as edge pixels. These pixels are fitted with a polynomial function, enabling a virtual refinement with a spacial resolution of less than one camera pixel. Next, the centre of the fit is determined. From here, the length of the minor and major semi-axes in vertical and horizontal direction is determined. The change in semi-axes over time gives the decay- or damping behaviour of a liquid, as depicted in figure 4.7.

The corresponding damping constant is obtained by fitting the time dependent decay behaviour
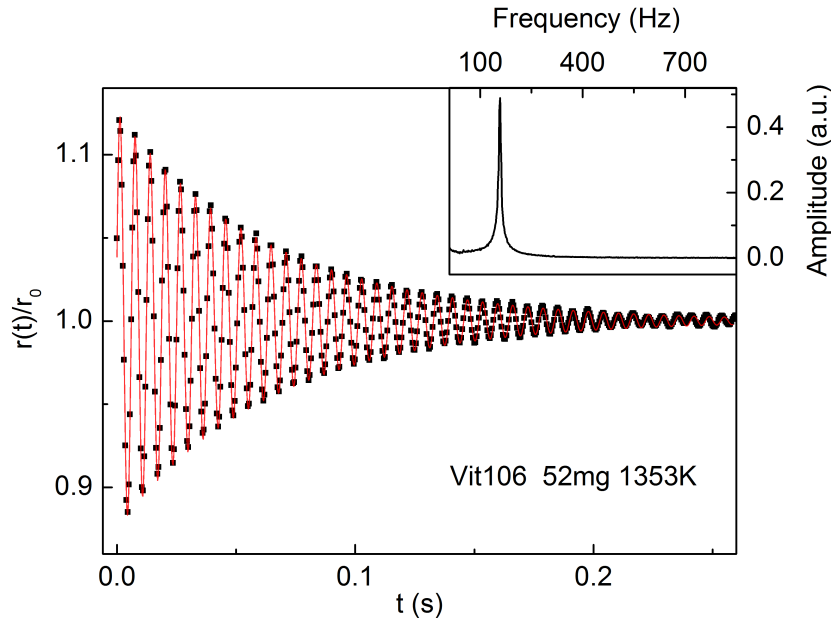
Figure 4.7 – Decay behaviour of a n = 2 and m = 0 surface oscillation at 1353 K. The damping behaviour is analysed in terms of the time dependent decay of the major semi-axis. The results are fitted using equation 4.39 in order to determine the damping constant.
The inset shows the corresponding excitation frequency, which is a single frequency near the droplets resonance frequency.

of figure 4.7 with equation 4.39.

$$r(t) = r_0 + A \cdot \sin(\omega t + \Phi) \exp\left(-\frac{t}{\tau}\right) \qquad (4.39)$$

Here r is either the minor or major semi-axis of the sample, r_0 the radius of the spherical sample (after the oscillation is damped), A the amplitude, ω the angular frequency, t the time, Φ the phase shift, and τ the damping constant. With the damping constant, τ and a rearrangement of equation 4.38 the viscosity, η of an axisymmetric surface oscillation induced by a single excitation frequency can be calculated according to

$$\eta = \frac{\rho \, r_0^2}{5 \, \tau_{(n=2)}} \qquad (4.40)$$

where ρ is the density and r_0 the radius of the spherical sample.

Viscosity measurements using electrostatic levitation (or other levitation techniques) in combination with the oscillating drop technique are technically challenging and require great precision during execution. Measurement artefacts arise easily from an insufficient quality of measurements. This, for instance is reflected in the fact that only within the last decades, the oscillating drop technique has been implemented and further developed [89, 77, 91].

The oscillating drop technique makes certain assumptions, which are not entirely fulfilled in (ground based) experiments (see chap. 3.2). This includes an electrically neutral droplet which levitates free of forces. This droplet is assumed to have a perfectly spherical shape and to oscillate in a defined n = 2 and m = 0 mode with no interior flow, except laminar flow.

Due to gravity it is impossible to levitate a droplet free of forces in ground based experiments. Microgravity platforms offer an improved initial situation, but even there, only levitation under reduced forces is possible as discussed in section 3.2. Therefore, electrostatically levitated droplets are not electrically neutral bodies, but always contains charge on the surface. This fact is neglected within ground based experiments.

The shape of a liquid droplet is considered spherical for small samples. These are samples with masses up to ~100 mg. Here, the uniform surface tension is sufficiently strong to counteract the deforming influence of gravity on a liquid sphere. Heintzmann [45] and Pommrich [85] demonstrated that viscosity measurements on samples smaller then 100 mg show no mass dependence. Therefore, droplets smaller then 100 mg are considered spherical.

Moreover, induced surface oscillations easily suffer artefacts. They arise from multiple oscillation modes or vibrations. It was found [45] that additional artefacts are sufficiently damped at lower temperatures, meaning temperatures in the vicinity of the sample's melting temperature. Here, artefacts have hardly any influence on the measurement. Whereas at higher temperatures (and viscosities lower than 20 mPas) additional artefacts form more easily, are barely damped and therefore distort measurements. Here, the excitation frequency easily splits into several frequencies, which extinct each other or form resonance frequencies, which re-excite each other. These effects are mostly observed for samples lager than 100 mg. Nevertheless, certain quality criteria for viscosity measurements are defined by [45, 85] to exclude possible side effects, as discussed above. These criteria are:

- The ratio of major, $r_0(z)$ and minor, $r_0(x)$ semi-axis after the oscillation decayed should not be greater than $\frac{r_0(x)}{r_0(z)} < 1.02$ [53]. Values greater than 1 indicate sample rotation. This flattens the poles, broadens the equator and violates the spherical shape.

- The amplitude of an induced oscillation should be by a factor three greater than the noise of a stably levitating sample.

- Upon stopping the excitation the oscillation shows an exponential decay behaviour without recurring oscillations [45].
  Any different behaviour indicates an oscillation mode different from the n = 2 and m = 0 mode.

All viscosity results presented within this work (chap. 5) fulfil the quality criteria discussed above. Viscosity measurements are obtained from samples smaller than 100 mg.

Besides, and unless stated otherwise viscosity measurements follow a certain temperature profile. That is heating the levitating droplet to ~150 − 350 K above its melting temperature to ensure a homogeneous liquid. Only then was the temperature reduced to the desired temperature where the viscosity measurement was performed.

Measuring errors

According to equation 4.40, the viscosity is calculated from three independent variables, density, ρ, sample radius, r, and decay constant τ, which all have an uncertainty themselves. Therefore, the error propagation of viscosity is calculated by the standard deviation, $\Delta\eta$.

$$\Delta\eta = \sqrt{\left(\frac{\delta\eta}{\delta\rho}\Delta\rho\right)^2 + \left(\frac{\delta\eta}{\delta r}\Delta r\right)^2 + \left(\frac{\delta\eta}{\delta\tau}\Delta\tau\right)^2} \tag{4.41}$$

The square single uncertainties can be rewritten using equation 4.40

$$\Delta\eta = \frac{r^2}{5\tau}\cdot\Delta\rho + \frac{2\rho r}{5\tau}\cdot\Delta r + \frac{\rho r^2}{5\tau^2}\cdot\Delta\tau \tag{4.42}$$

$$\Delta\eta = \frac{\rho r^2}{5\tau}\cdot\frac{\Delta\rho}{\rho} + \frac{\rho r^2}{5\tau}\cdot\frac{2\Delta r}{r} + \frac{\rho r^2}{5\tau}\cdot\frac{\Delta\tau}{\tau} \tag{4.43}$$

$$\Delta\eta = \eta\cdot\frac{\Delta\rho}{\rho} + 2\eta\cdot\frac{\Delta r}{r} + \eta\cdot\frac{\Delta\tau}{\tau} \tag{4.44}$$

$$\frac{\Delta\eta}{\eta} = \frac{\Delta\rho}{\rho} + 2\cdot\frac{\Delta r}{r} + \frac{\Delta\tau}{\tau} . \tag{4.45}$$

Based on equation 4.45 the influence of each parameter can be determined. According to the error analysis of density measurements in paragraph 4.2.3, the error in density is $\Delta\rho \leq 1\%$.

The uncertainty in radius is determined by the mass loss of a sample during levitation experiments. Care was taken during experiments not to lose more than 1 % of the sample mass, in order to ensure an exact and consistent sample composition. The mass is proportional to the third power of the radius, according to equation 4.7. Therefore, the uncertainty in radius is $\Delta r \leq \frac{1}{3}\%$. With these estimations, the uncertainty in density and radius is $\frac{\Delta\rho}{\rho} \leq \frac{1}{100}$ and $\frac{2\Delta r}{r} \leq \frac{1}{150}$, respectively. Since, these uncertainties are negligibly small, the first two terms of equation 4.45 are neglected.

The damping constant, τ thus dominates the uncertainty in viscosity as follows:

$$\Delta\eta = \eta\cdot\frac{\Delta\tau}{\tau} \tag{4.46}$$

Here τ is the damping constant of an optimal fit, determined according to equation 4.39. η is the viscosity calculated from τ. $\Delta\tau$ is the fit uncertainty of τ, which for instance includes the difference in τ for vertical and horizontal directions. It was found, that $\frac{\Delta\tau}{\tau}$ varies about 10 %.
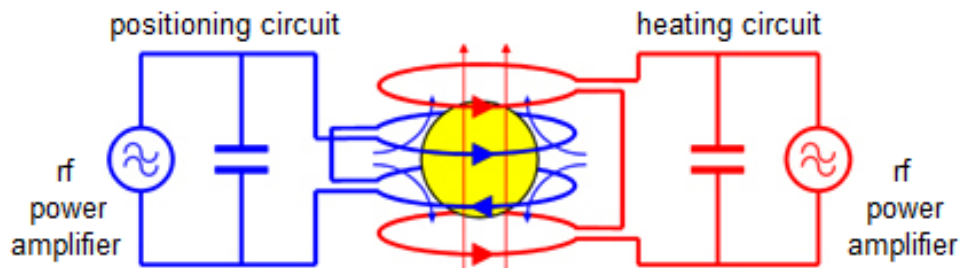
4.3 Electromagnetic levitation in microgravity (TEMPUS)

Electromagnetic levitation (EML) allows containerless processing of electrically conductive samples within a high-frequency alternating magnetic field. Electromagnetic levitation experiments in combination with the oscillating drop technique (section 4.2.6) and under microgravity conditions, as performed in the TEMPUS facility, [2] enable measurements of viscosity.

Here, samples are approximately 15 to 20 times larger than in ground based ESL experiments and are processed using smaller positioning forces. Experiments using the TEMPUS facility are performed on DLR parabolic flights in Bordeaux (France) [80].

Parabolic flights offer the opportunity to perform experiments under reduced gravity conditions (see chap. 3.2). For this purpose, a specially converted aircraft flies parabolic manoeuvres and thereby achieves 22 s of microgravity at each parabola [80].

The TEMPUS facility uses a two coil system for electromagnetic levitation under reduced gravity conditions, as shown in figure 4.8.

Figure 4.8 – TEMPUS facility coil setup: Two coil system for electromagnetic levitation under microgravity conditions [31].

An alternating current in a conductor, like the levitation coil forms a magnetic field around the conductor. This field induces eddy currents to an electrically conductive sample, located in the middle of the levitation coil. These eddy currents on the one hand cause a heating of the sample due to resistive losses, which are accompanied by fluid flow inside the sample [50, 29] and on the other hand induce another magnetic field, that is counter directed (with a $180°$ phase shift) towards the outer magnetic field. The resulting force, the Lorentz force, lifts the sample against gravitation and thereby levitates it. A suitable coil shape and alternating current frequency need no active positioning to gain a stable levitation. This is, because a potential minimum exists. Therefore, electromagnetic levitation is technically much easier to realize than electrostatic levitation.

---

[2] Tiegelfreies Elektromagnetisches Prozessieren Unter Schwerelosigkeit [88, 35, 92]

The two coil system, as depicted in figure 4.8 is an approach to decouple levitation and heating processes in electromagnetic levitation. This, however only works in microgravity conditions. One coil positions the sample, using a 150 kHz quadrupole field while the other coil offers a 350 kHz dipole field for inductive heating of the sample. Both coils can be operated individually.

Excitations of surface oscillations for viscosity measurements with the oscillating drop method are generated through the heating circuit. TEMPUS uses a single rectangular pulse of a tenth second to excite a surface oscillation.

However, this means that in the TEMPUS facility the sample can either be held at a constant temperature or an excitation pulse for the oscillating drop method can be set, since both actions are executed using the same heating circuit. Therefore, viscosity is measured upon free cooling and is determined over a temperature range. In this work, TEMPUS viscosities are displayed at their average temperature over their decay time. However, the complete temperature range is reflected by the error bar plus the temperature error calculated according to section 4.2.1. Errors are further discussed in chapter 5.1 (fig. 5.1).

In the TEMPUS facility samples are processed in a specimen changing cup in order to not lose them during experiments or in between parabolas. The temperature is contactlessly tracked with a single colour pyrometer, just like in ESL experiments (see 4.2.1). The sample is monitored with two cameras, one of which records images for analysis (see 4.2.7). The whole setup is operated under argon gas atmosphere.
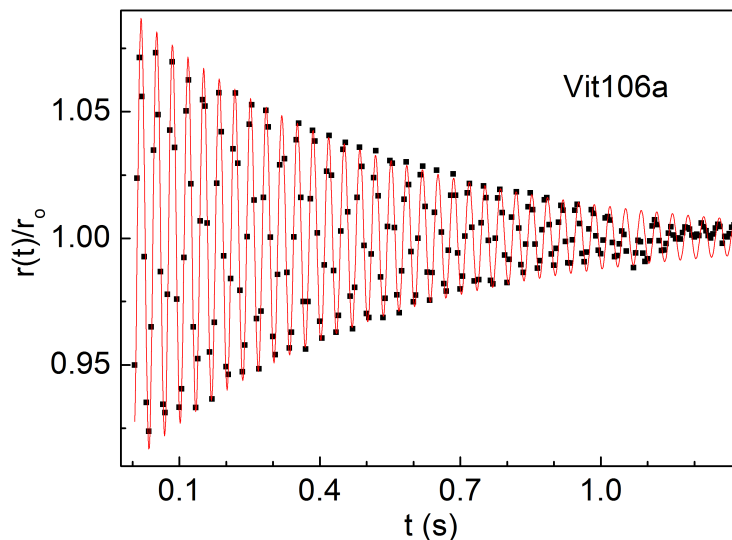
Figure 4.9 – Damping curve of a 1.4 g Vit106a sample around 1400 K recorded in the TEMPUS facility under microgravity conditions during the 23rd DLR parabolic flight campaign.

The analysis of TEMPUS viscosity experiments is performed similarly to ESL viscosity experiments (see section 4.2.7). All captured images are analysed using the in-house software TeVi.

However, samples processed in the TEMPUS facility are 2 - 3 times larger in diameter than ESL samples. Therefore, they take approximately 5 - 8 times longer to damp an oscillation, as shown in figure 4.9. (For a ground based ESL comparison see figure 4.7.)

During the decay of over $1\,s$, excellent microgravity conditions are required to investigate viscosities. Parabolic flights reach a μg quality of 10^{-1} down to 10^{-3} g [80], depending on wind and weather conditions. Additional vibrations are transferred from the aircraft to the TEMPUS facility and through the electromagnetic positioning field to the sample. They cause additional forces on the levitating sample and disturb the free damping behaviour. TEMPUS viscosities presented within this work (see fig. 5.2 and 5.3) were obtained on the 23rd and 24th DLR parabolic flight in September 2013 (Vit106a) and October 2014 (industrial AMZ4), respectively.

4.4 Differential Scanning Calorimetry

Differential scanning calorimetry is a thermal analysis method to determine the amount of heat absorbed or released by a sample during heating or cooling processes in comparison to a reference. It gives information about the glass transition, crystallisation, and melting temperature. Sample systems investigated within this thesis are multicomponent systems (see section 4.1) for which no phase diagram exists. But, since every sample system investigated by a levitation technique needs a temperature correction (see 4.2.1), reference temperatures are determined using differential scanning calorimetry.

In differential scanning calorimetry, a crucible containing a sample and an identical empty reference crucible are both subject to a defined temperature program. Due to the heat capacity change during phase transitions and exothermic or endothermic processes, a temperature difference between sample and reference becomes visible. By integrating this temperature difference over time, the heat flow and thus the change in enthalpy is calculated, as shown in figure 4.10.

In this work, a (404 C 'Netzsch') differential scanning calorimeter (DSC) was employed. Samples were placed in zirconium oxide (ZrO_2) crucibles, since these proved to be the least reactive crucibles.

Samples investigated passed a temperature program consisting of three heating and cooling cycles with isothermal stops of $10\,min$ at each minimum and maximum temperature. Heating and cooling rates were $10\,K/min$. Maximum temperatures are set to be almost $100\,K$ above the respective melting temperature. Every sample composition studied in this work was investigated by DSC in terms of its glass transition, solidus and liquidus temperature, as shown in table 4.1. Either solidus or liquidus temperature was then used for temperature calibrations of levitation experiments as discussed in section 4.2.1.

The temperature uncertainty of DSC measurements is given with $\pm 4\,K$ up to $1373\,K$.
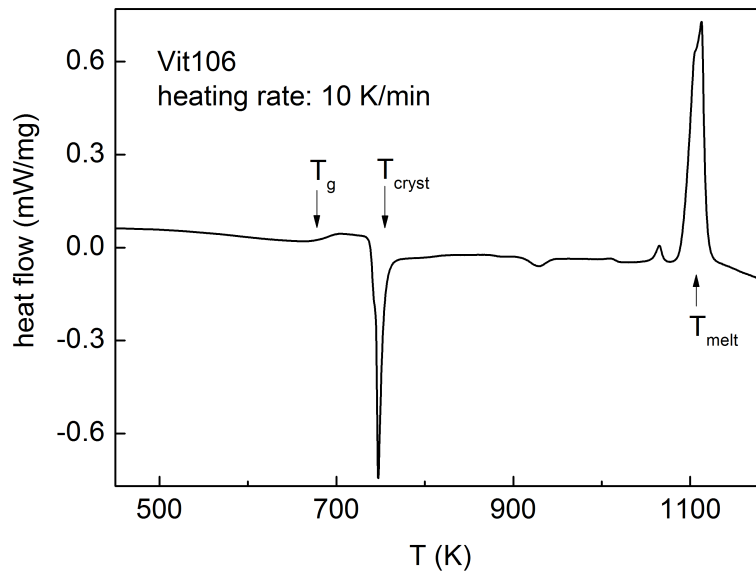
Figure 4.10 – DSC curve of an amorphous Vit106 sample upon heating at 10 K/min. Glass transition temperature, T_g, crystallisation temperature, T_{cryst}, and melting temprature, T_m are indicated.

## 4.5 High temperature concentric cylinder rheometer

Couette rheometry is a container-based method to determine high temperature viscosity of liquids at controlled shear rate and temperature.

Couette rheometer results presented within this thesis were conducted at the Chair of Metallic Materials at the University of Saarbrücken by William Hembree. Experiments as well as analysis were performed by Hembree and are only cited within this work in the course of a joint DFG research project (ME 1958/11-1).

A rheometer consists of a stationary and a moving part. The rheometer device used corresponds to DIN 53019, which is a Mooney-Ewart coaxial cylinder measurement system. A schematic setup of the shear cell is depicted in figure 4.11. Here, the cup which contains the liquid to be investigated is stationary and the cylinder, which is immersed into the cup for coaxial measurements is the moving part.

The shear rate is determined by the rotational velocity of the cylinder and the experimental setup geometry. The corresponding reaction torque on the cup is measured upon shearing and used to calculate the viscosity.

Samples are heated and molten inductively in the cup. Measurements are typically performed in the temperature range between liquidus temperature of the sample and a few hundred Kelvin above T_{liq}.
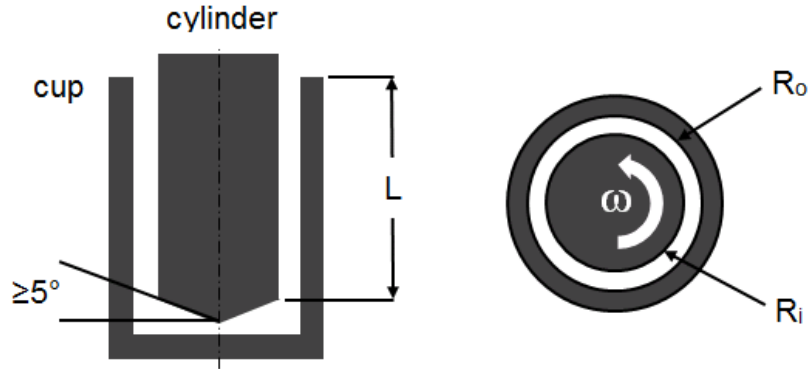
Figure 4.11 – Schematic of the conicylinder shear cell taken from Ref. [47]. (left) Side view of
cup and cylinder, where the cylinder is immersed into the cup by the immersion length, L.
(right) Top view of cup and cylinder, which rotates with the radial velocity, ω. Besides, the
inner radius of the cup, R_o and outer radius of the cylinder, R_i are marked.

The radial velocity, ω of the cylinder is computer controlled and can be adjusted to the desired
shear rate. The reaction torque, M on the cup is measured with a high sensitivity torque sensor.
The viscosity, η is calculated according to

$$\eta = \frac{(R_o^2 - R_i^2)M}{4\pi L(R_o^2 + R_i^2)^2 \omega c_L} \ .$$

(4.47)

R_o is the inner radius of the cup, R_i the outer radius of the cylinder, L is the immersion length of
the bob, and c_L is a correction factor, which considers the torque contribution from the conical
apex of the cylinder.

Experiments are performed under argon atmosphere. Samples were first heated $300\,\mathrm{K}$ above
their respective liquidus temperature to ensure a homogeneous melt. Then a gradually increased
shear rate profile was applied in clockwise and counter clockwise direction, while the melt was
cooled at a rate of $0.33\,\mathrm{K\,s^{-1}}$ until just prior to the onset of crystallization. The process was im-
mediately repeated only that the melt was heated at a rate of $0.33\,\mathrm{K\,s^{-1}}$ back to the starting tem-
perature.
This heating and cooling process was repeated three times in total for different shear rates. For
further information on Couette measurements and analysis see Hembree [47].

4.6   In situ high energy synchrotron x-ray diffraction

ESL experiments in combination with in situ high energy x-ray investigations were carried out on
the PETRA III P07 beamline at DESY (Deutsches Elektronen-Synchrotron , Hamburg). This setup
allows studying time-resolved structural information of BMGs on the atomic scale.

For this purpose, the mobile ESL (chap. 3.3.2) was installed at the PETRA III P07 beamline as shown in figure 4.12. The PETRA III P07 beamline is one of the most brilliant storage ring based x-ray sources worldwide. For the current study hard x-rays, thus radiation of very short wavelengths was used. These high energy x-rays are capable of penetrating through small volumes, like ESL samples (~ 100 mg) and thus provides information on the bulk. Figure 4.14 provides a schematic of this experimental setup.
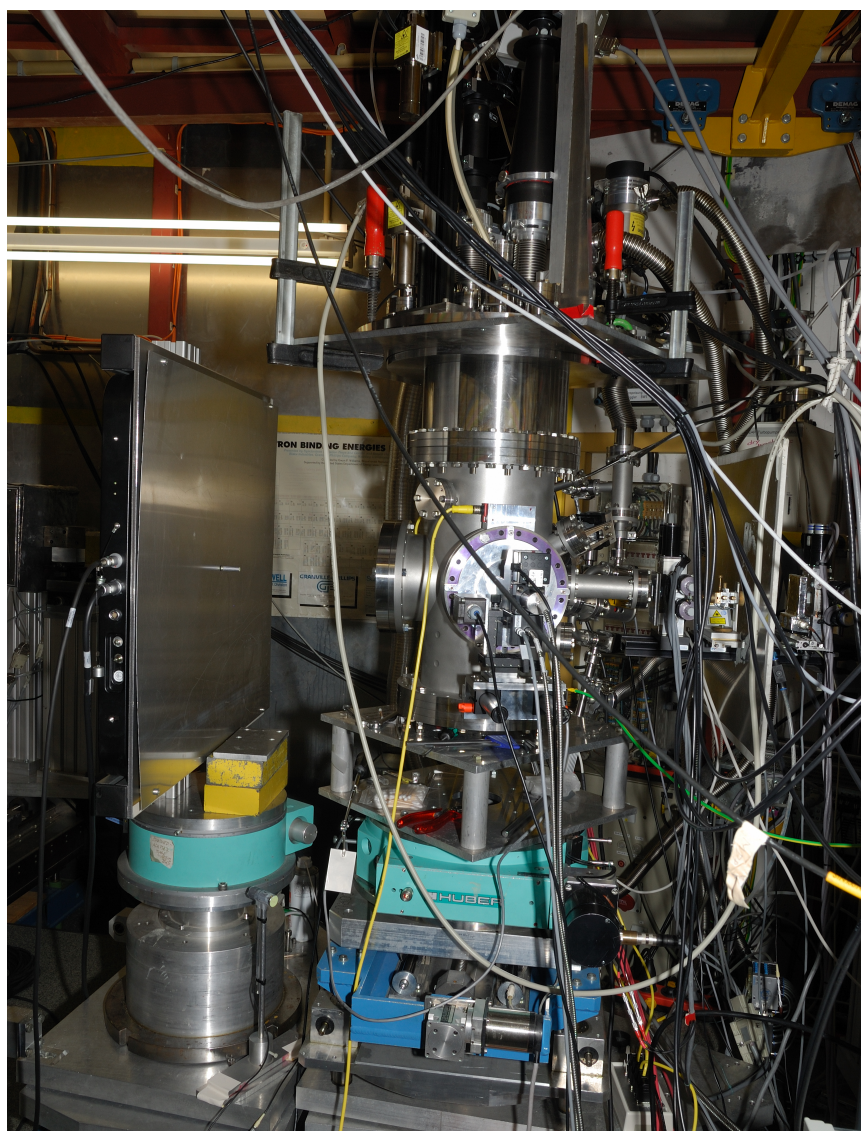
Figure 4.12 – The mobile electrostatic levitator (chap. 3.3.2) installed at the PETRA III P07 beamline at DESY (Hamburg). The detector with beam stop is found on the left hand side in the photo, while the mobile ESL (or rather its vacuum chamber) is installed on a height-adjustable platform in the very middle of the picture. High energy x-rays approach the setup through a window in the vacuum chamber (right hand side in figure). They are diffracted by the sample and impinge on the detector. For a schematic setup see figure 4.14.

Within this work diffraction experiments on levitating liquid samples were performed using radiation with a photon energy, E_{ph} of 100 keV. This corresponds to a wavelength, λ of 0.124 Å, according to equation 4.48

$$E_{ph} = h \cdot \nu = \frac{h \cdot c}{\lambda} \tag{4.48}$$

where h is Planck's constant, ν the frequency, and c the speed of light. The beam size was 0.8 x 0.8 mm².

Diffraction experiments were carried out in the transmission mode. In figure 4.12, the primary beam approaches from the right hand side and penetrates through the sample. The remaining primary beam as well as the diffracted shares pass through an exit window located in the middle of figure 4.12. The exit window is equipped with a beam stop in order to absorb the primary beam, which is not diffracted. The beam stop prevents beam damage on the detector and reduces background noise. Still remaining primary x-rays as well as the diffracted shares impinge on the detector installed in a certain distance from the mobile ESL and opposite to the incident primary beam (see fig. 4.12 left hand side). Here, a second additional beam stop is installed, in order to avoid beam damages on the detector. The diffracted x-rays impinge on the detector according to their diffraction angle and form so-called diffraction patterns, as illustrated in figure 4.13.
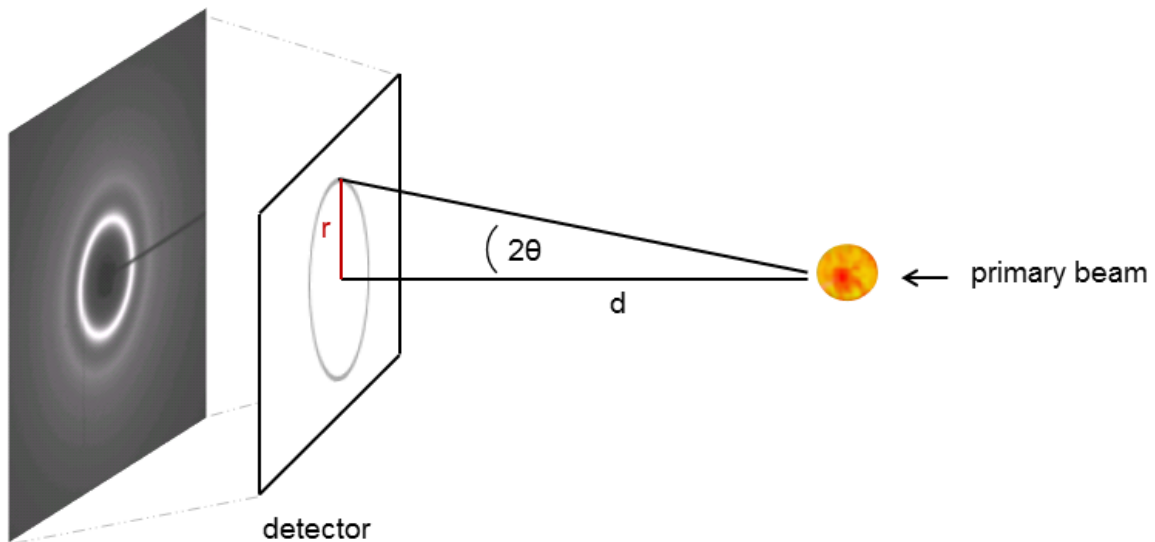
Figure 4.13 – Diffraction geometry and experimental setup of the mobile ESL installed at the PETRA III beamline.

In this schematic the primary beam approaches from the right, penetrates the sample, and scatters onto the detector on the left hand side. The distance between sample and detector is given

by d, while the diffraction angle, 2Θ is defined as

$$2\theta = \tan^{-1} \frac{r}{d} \tag{4.49}$$

according to the trigonometric function of a right triangle. The radius r originates in the symmetric centre of the diffraction patterns and describes them according to its length. Different radii are obtained by integrating $r + dr$. The radius in turn, can be subdivided into even smaller distances. The distance, q depends on the setup and is determined according to

$$q = \frac{4\pi}{\lambda} \sin(\theta) \tag{4.50}$$

with λ being the wavelength of $0.124\,\text{Å}$. By combining equation 4.49 and 4.50, q is described as

$$q = \frac{4\pi}{\lambda} \sin\theta = \frac{4\pi}{\lambda} \sin\left(\frac{1}{2} \tan^{-1} \frac{r}{d} \right). \tag{4.51}$$

Based on equation 4.51, q is the smallest distance that can be resolved in a diffraction experiment. It is also a multiple of the diffraction angle 2Θ.

For detection a two-dimensional Perkin Elmer XRD1621 CsI bonded amorphous silicon detector was used with 2048×2048 pixels and a pixel size of $200 \times 200\,\mu\text{m}^2$. This detector enables intensity investigations in dependence of the diffraction angle (2Θ) and with an excellent temporal resolution. For heating/cooling experiments, as conducted within this work (section. 5.10) data with a temporal resolution of $1\,\text{s}$ was acquired. The exposure time was $1\,\text{s}$ as well. The beginning of a heating/cooling experiment was synchronised with the recording of diffraction patterns. Additionally, this synchronisation was re-checked by crystallisation events of the sample.

The pyrometer temperature was corrected according to section 4.2.1. An additional uncertainty in sample temperature to the pyrometer correction results from the temperature - diffraction pattern correlation. It is estimated to be $\pm 10\,\text{K}$.

In order to obtain the intensity distribution, $I(Q)$ over the diffraction angles a background subtraction and a correction for sample absorption, fluorescence and inelastic (Compton) scattering is applied to the two-dimensional x-ray diffraction pattern before integrating them. This is done using the data analysis software Fit2D [43]. To obtain the structure factor, $S(Q)$ correction for Laue diffuse scattering and normalisation to the atomic x-rays form factor are applied to the intensity, $I(Q)$ using data analysis software PDFgetX2 [87]. Further details for the correction can be found in [34]. The position of the first intensity maximum was extracted by a cubic spline interpolation method, which according to [99] gives the most reliable peak position.

Note, that within this work x-ray diffraction is used to distinguish between the crystalline and liquid state of a sample. X-ray diffraction of liquids, yields no defined structural analysis, but a smeared-out distribution of mean positions of atoms in the liquid. Moreover, the temperature evolution of liquid structures is monitored.

The minimum amount of crystallisation detectable is estimated to be $\leq 5\,\%$ of the sample mass.
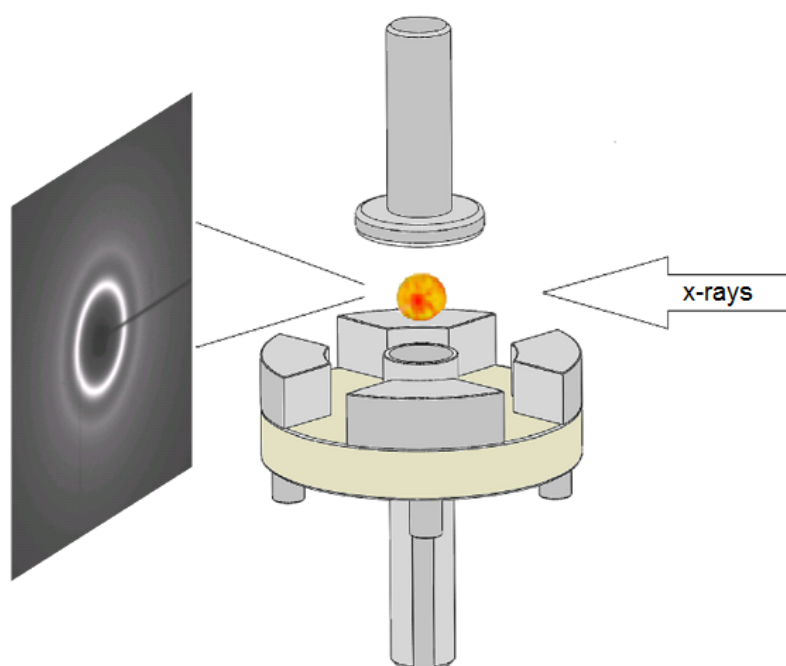
Figure 4.14 – Schematic setup of an x-ray diffraction experiment in combination with electrostatic levitation. An electrode system with levitating sample, which is screened ny x-rays is shown. The resulting diffraction patterns are recorded by the 2D detector and are later analysed in terms of structural information.

Chapter 5

Results and Discussion

This chapter presents results of the experimental methods introduced and discussed in chapter 4. The first section of this chapter deals with the accuracy of high temperature viscosity measurements. For this, the results of three different measurement methods are compared. These methods are Couette rheometry, electrostatic, and electromagnetic levitation in combination with the oscillating drop technique and the latter under reduced gravity conditions.
Only then are further properties of the liquid and undercooled state of several BMGs investigated to see whether they provide information on an underlying transition. These properties include viscosity, density, volume expansion, thermal expansion coefficients, and the heat capacity.
Last, in situ structural investigations combined with ESL are conducted in order to exclude crystallisation as possible origin for an underlying transition. This is followed by studies of structural changes in the liquid and undercooled melt.

5.1 Accuracy of viscosity measurements in metallic melts

Changes in the temperature dependence of the melt viscosity of Vitreloy 1 [114, 111] have been suspected to be an indication of a liquid-liquid transition. However, in literature high temperature viscosity data scatters over two orders of magnitude for this very BMG [111, 69, 76, 46]. This shows that measuring high temperature viscosity of metallic melts is still not a trivial task. This is mainly because of the high reactivity of Zr-based metallic melts with crucible material. But, in order to review indications of a liquid-liquid transition accurate data is required. Therefore, in this section high temperature viscosity data obtained by different measurement methods is compared in terms of its accuracy and to exclude systematic errors arising form measurement artefacts.
These methods are Couette rheometry and electrostatic as well as electromagnetic levitation in combination with the oscillating drop technique and the latter under reduced gravity conditions. These methods represent different approaches to determine high temperature viscosity. On the

one hand via containerless (levitation techniques) and on the other hand via container-based methods (rheometry). In addition, these methods are selected in analogy to the measurement methods used to determine the viscosity data on Vitreloy 1, which scatters over two orders of magnitude [111, 69, 76, 46]. In order to exclude any influence from sample material on these measurements, samples used for different measurement techniques are prepared from the same batch (as discussed in section 4.1).

First, the viscosity of Vit106a is measured using electrostatic levitation in combination with the oscillating drop method (for the oscillating drop method see section 4.2.6). The resulting viscosity data is presented in figure 5.1. It covers a temperature range of roughly 400 K from around 1500 K down to approximately 1115 K, thus close to the liquidus temperature of Vit106a. The viscosity in this temperature region decreases monotonically with increasing temperature from approximately 275 mPas down to 10 mPas. This viscosity range is typical for measurements using the oscillating drop technique in combination with ESL. Above 275 mPas the induced surface oscillation on the sample is damped too quickly for an accurate determination of a damping constant to calculate the viscosity, while below 10 mPas and under laboratory conditions small disturbances of the surface oscillation can distort the damping behaviour.
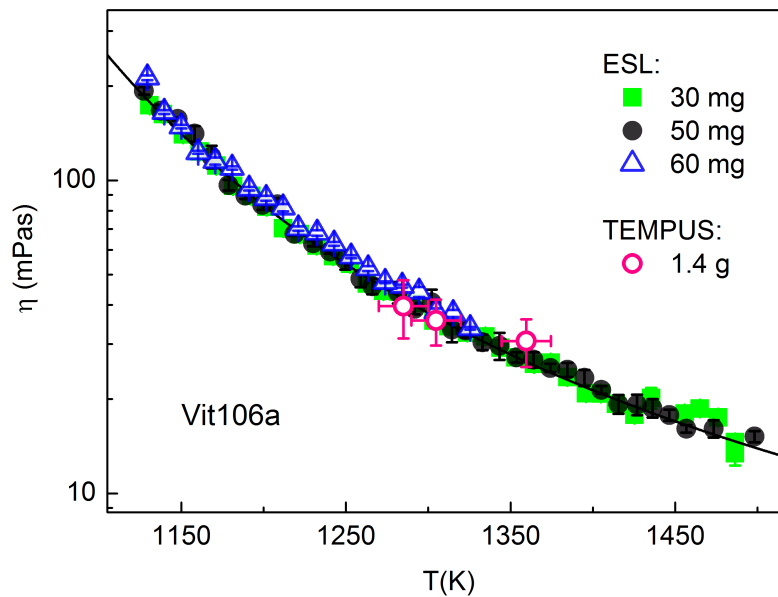
Figure 5.1 – High temperature viscosities of Vit106a determined by electrostatic and electromagnetic levitation in combination with the oscillating drop technique the latter under microgravity conditions (TEMPUS). Different sample masses show no mass dependence between viscosities obtained under normal gravity conditions using ESL and reduced gravity conditions using the TEMPUS facility.

The analysis of viscosity measurements using the oscillating drop technique considers a droplet free of external forces [89]. These conditions are not fulfilled in ground based ESL experiments due to the presence of gravitational force and positioning fields. These forces depend on the mass of the sample. (For local disequilibrium forces on a levitating sample see section 3.2). Therefore, different masses are investigated, since measuring artefacts would become obvious in a mass dependence of the viscosity.

Here, viscosity measurements with three different sample masses are performed. No deviations between the individual measurement results are found, as shown in figure 5.1. Each sample was excited with a frequency close to its eigenfrequency, which in turn corresponds to the sample mass. It was ensured that all quality criteria of viscosity measurements, as discussed in section 4.2.7 are fulfilled for these measurements. The resulting viscosities of the three measurements are consistent with each other. Hence, no mass dependency exists. This demonstrates that the damping behaviour of the individual sample is not influenced by external disturbances. Thus, the measurements presented in figure 5.1 are not affected by external disturbances. Instead, they demonstrate the excellent reproducibility of viscosities determined by electrostatic levitation in combination with the oscillation drop technique over the investigated range of viscosities.

Still, these experiments are subject to gravitational force. In order to reduce this force and thereby its influence on the measurement technique, experiments under reduced gravity conditions are performed. In the TEMPUS facility, the positioning field is much smaller than in ground based experiments. Also, the gravitational field is reduced to approximately 5 %. This is done by using electromagnetic levitation in combination with the oscillating drop technique in the TEMPUS facility. (For more information on the TEMPUS facility see section 4.3)

In the TEMPUS facility, a two coil system is used to decouple heating and levitation processes in order to enable viscosity measurements in an electromagnetic levitation facility. Apart from the heating task the heating coil is also used to generate pulses for surface oscillations.

Viscosity measurements at constant temperature are not possible in the TEMPUS facility. On the one hand because every surface oscillation pulse heats up the sample as well. Thus, every pulse is accompanied by an increase in temperature. On the other hand because a constantly applied heating field induces internal flow inside the sample. This, however is not permissible according to the requirements for viscosity measurements as discussed in section 4.2.6. Consequently, the heating coil can not be turned on all the time to keep the sample temperature constant and hence, viscosities can only be determined upon free cooling in the TEMPUS facility.

The viscosities measured in the TEMPUS facility are displayed in figure 5.1. They agree with viscosities obtained by the ESL technique within the measurement uncertainty. TEMPUS samples are approximately 3 times larger in diameter than samples processed in a ground based ESL. Therefore, they take around 5 - 10 times longer to damp an oscillation, which under reduced gravity conditions takes at least 1 s in time (see TEMPUS damping curve in figure 4.9). This means, TEMPUS viscosity data is determined upon cooling over at least 1 s. During this time the tem-

perature can change up to 30 - 40 K, depending on the starting temperature. Hence, TEMPUS viscosities are always determined over a temperature range. This is reflected in the error bars of the temperature.

The uncertainty in viscosity is attributed to sample size, instability during the levitation process, and the estimated influence of the uncertainty in temperature (ΔT) on the viscosity. Vibrations from the aircraft due to wind, weather, and flight conditions are always present and cause a position instability. Therefore, parabolic flights reach a reduced gravity level of $\pm$ 0.05 g [80]. Vibrations are transferred from the aircraft to the TEMPUS facility and through the electromagnetic positioning field to the sample. These facts cause an uncertainty in the analysis of the damping constant to calculate the viscosity. Beyond that the uncertainty in viscosity includes an estimation of the influence that the temperature uncertainty will have on the viscosity.

TEMPUS offers a good option to conduct comparative and complementary viscosity measurements for ground-based experiments. Although the uncertainties are larger than in ground based ESL experiments TEMPUS results confirm that the influence of gravitational forces on a levitating sample can be neglected in ground based ESL viscosity measurements. Moreover, the TEMPUS experiments as well as the mass variation in ESL experiments show that no measuring artefacts exist on the oscillating drop technique, as long as external perturbations are small [45]. This finding even holds for samples of the gram range.

For an enhanced precision of viscosity data determined under reduced gravity conditions, electrostatic levitation needs to be brought into microgravity, as prepared by [78, 79].

As a next step, viscosity data determined with the oscillating drop method is compared to viscosity data determined by Couette rheometry[1]. This is done for the four BMGs Vit106a, Vit106, Inoue 4, and high purity AMZ4. (For an overview of all investigated BMGs see section 4.1.)

Viscosities determined by Couette rheometry[1] are measured upon cooling and reheating of the melt, as indicated by filled and open triangles respectively, while viscosities determined by the ESL technique consist of two individual measurements with different sample masses as indicated by open and filled squares.

The resulting viscosities of the individual BMGs are displayed in graph a) - d) of figure 5.2. ESL and Couette rheometer results are in general agreement with each other. All viscosities decrease monotonically with increasing temperature. ESL data covers a temperature region of 400 K, from around 1100 K to approximately 1500 K. The viscosity in this temperature region reaches from ~ 275 mPas down to 10 - 15 mPas. Couette rheometer results cover a temperature region from 100 to 250 K, starting from ~ 1150 K onwards. The viscosity in this region reaches from just above 100 mPas down to 15 - 20 mPas for individual measurements. ESL measurements cover a broader temperature range than Couette rheometer measurements. In addition, they reach down to (fig. 5.2 a), b)) and below (fig. 5.2 c), d)) the respective liquidus temperature as well as to temperatures

---

[1]Experiments were performed and analysed by W. Hembree (University Saarland)
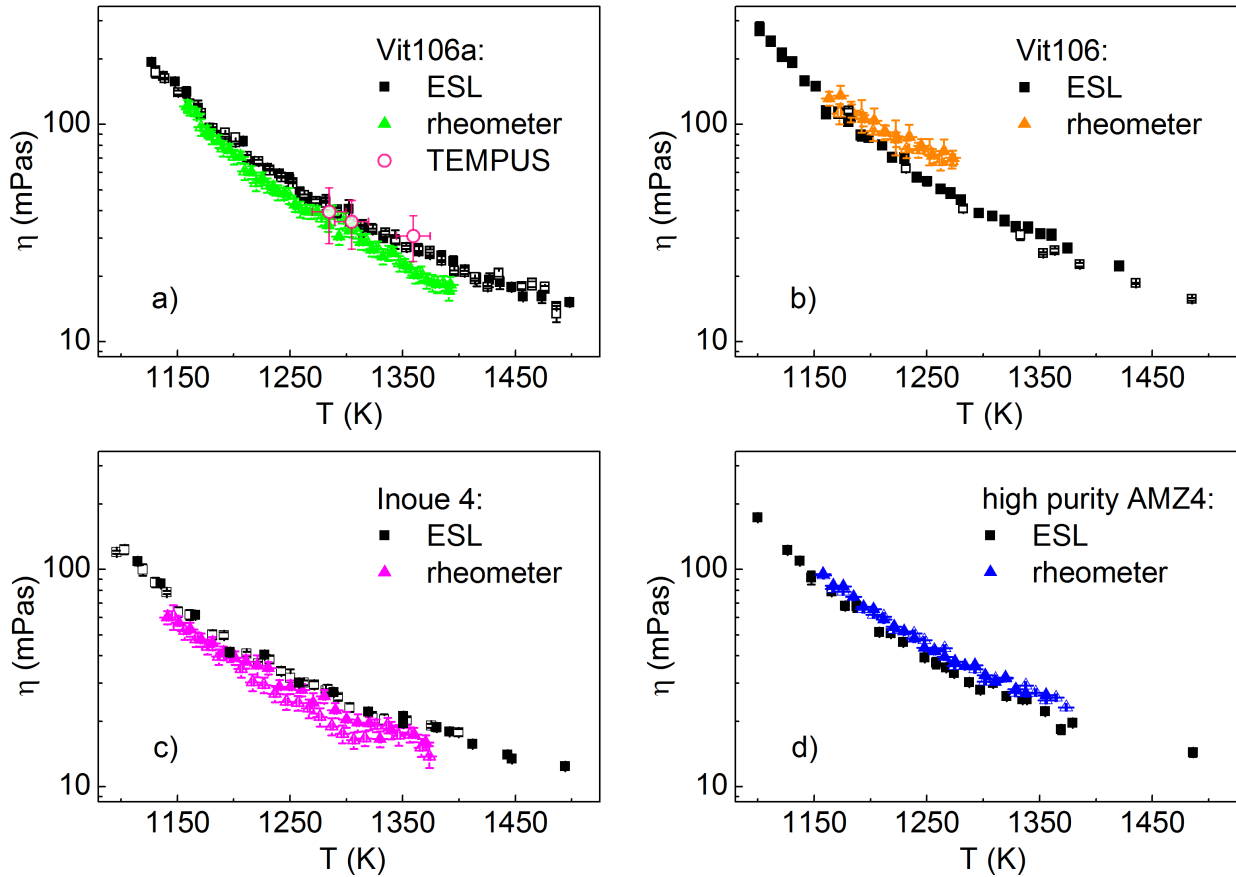
Figure 5.2 – High temperature viscosities of the BMGs Vit106a (a), Vit106 (b), Inoue 4 (c), and high purity AMZ4 (d) determined by Couette rheometry (triangles) and electrostatic (squares) and electromagnetic levitation (circles) in combination with the oscillating drop technique, the latter under microgravity conditions (TEMPUS). Couette rheometer experiments were performed and analysed by W. Hembree (University Saarland)

above 1400 K. (For individual liquidus temperatures see table 4.1.)

Graph a) of figure 5.2 displays viscosity results of Vit106a. Data determined by Couette rheometer and ESL technique coincides well at lower temperatures, but deviate towards higher temperatures. Here, Couette rheometer results display a lower viscosity than ESL results. Additional TEMPUS data coincides with ESL data (as discussed above). Couette rheometer data deviates (from TEMPUS and ESL data) at higher temperatures to lower viscosities.

Graph b) presents viscosities of Vit106. Here, again viscosities coincide at lower temperatures, but deviate towards higher temperatures. This time Couette rheometer results deviates towards higher viscosity values.

Graph c) shows viscosity data of Inoue 4. Couette rheometer data is slightly lower than ESL data

and scatters little towards higher temperatures. However, both data sets show a similar temperature dependence.

Graph d) displays viscosity results of high purity AMZ4. Here, Couette rheometer and ESL results agree very well within the common temperature range. The Couette rheometer data is insignificantly higher than the ESL data.

Thus, ESL and Couette rheometer results on high purity AMZ4 are in good agreement, while results on Vit106a, Vit106, and Inoue 4 deviate at temperatures above ~1250 K. This suggest either a reaction or beginning reaction with the crucible material and/or a violation of the laminar shear conditions on the rheometer side or an indefinite oscillation mode on the ESL side. Since previous ESL experiments proved the accuracy of this method and that no mass dependence on the oscillating drop technique exists, the issue is expected to be on the rheometer side and is probably related to reactions at elevated temperature.

In conclusion, viscosities determined by ESL in combination with the oscillating drop technique and by Couette rheometry coincides within an absolute measurement error of 20 %. ESL in combination with the oscillating drop technique has the advantage of covering a broader temperature range and offering access to the undercooled state. It thereby enables viscosity measurements at and below the liquidus temperature. Finally, this method allows a precise determination of viscosities in the range of 10 to 275 mPas.

This stands in contrast to Couette rheometer measurements, which require equilibrium melt conditions (above T_{liq}) and can thus only measure until just prior to the onset of crystallisation. However, a Couette rheometer can measure viscosities up to the Pas range. This means, in highly viscose systems Couette rheometry will achieve results at lower temperatures than the ESL technique. This, however, does not apply to the investigated systems.

The sample compositions investigated so far are all made of high purity starting materials. For applications of BMGs, the purity of the starting materials is an important cost driver. However, industrial grade materials usually contain more impurities. It is therefore important for cost-efficient production to find out whether measurements of thermophysical properties are affected by the quality of the starting materials.

Therefore the influence of impurities on the starting material is investigated on the example of AMZ4. Here, two different grades of AMZ4 were prepared. High purity AMZ4, as already investigated in figure 5.2 d) and industrial AMZ4. (For more information on AMZ4 see section 4.1.) The high temperature viscosity of both grades AMZ4 is measured using Couette rheometry, electrostatic and electromagnetic levitation in combination with the oscillating drop technique and the latter under microgravity conditions.

First, Couette rheometer measurements of industrial and high purity AMZ4 are performed as shown in figure 5.3 (left). These measurements cover a temperature range of around 200 K and a viscosity range of 20 to 175 mPas. They differ in absolute viscosity by a factor of approximately 2,
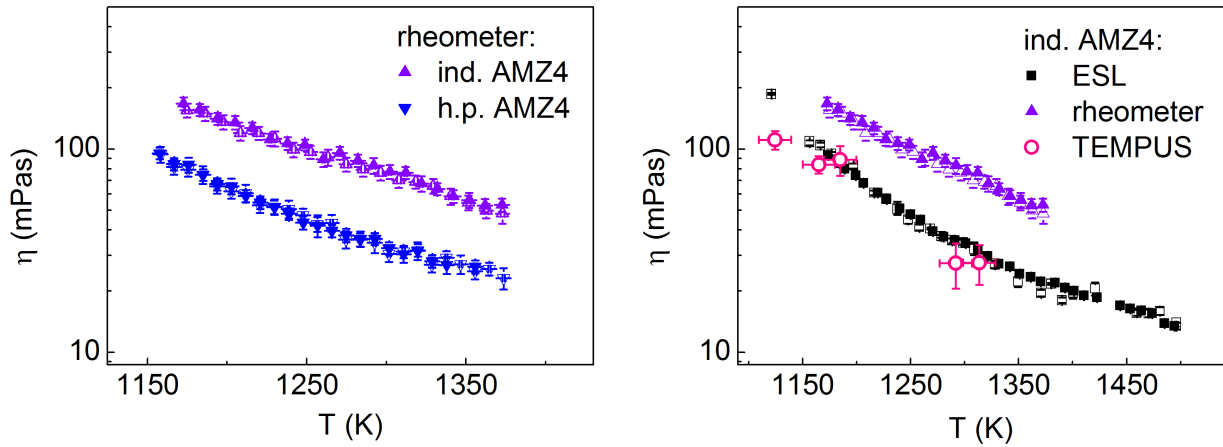
Figure 5.3 – Melt viscosities of high purity and industrial AMZ4 determined by Couette rheometry [a], electrostatic and electromagnetic levitation in combination with the oscillating drop technique and the latter under microgravity conditions (TEMPUS [b])

(left) Couette rheometer measurements of industrial and high purity AMZ4. Open symbols are determined upon heating, while filled symbols are determined upon cooling.

(right) Melt viscosities of industrial AMZ4 determined using Couette rheometry, the ESL technique, and the TEMPUS facility. Open and filled ESL symbols indicate different sample masses.

[a] Experiments are performed and analysed by W. Hembree (University Saarland)

[b] Experiments are prepared and analysed by W. Hembree (University Saarland)

but show a similar temperature dependence.

Results from comparative measurement on high purity AMZ4 using also the ESL technique are shown in figure 5.2 d). They are in good agreement with each other.

In the case of industrial AMZ4 viscosities are remeasured using ESL and EML in combination with the oscillating drop technique and the latter under reduced gravity conditions (TEMPUS). Results of all three viscosity measurement techniques are shown in figure 5.3 (right). Here, ESL data covers a temperature range of around 400 K and a viscosity range of 15 to 200 mPas. This data is in good agreement with TEMPUS data obtained under reduced gravity conditions. However, the Couette rheometer viscosities vary from the two data set (of ESL and TEMPUS) by a factor of approximately 2 towards higher viscosities.

When comparing only ESL viscosities of high purity and industrial AMZ4 it is found that these results deviate much less from each other than when comparing only Couette rheometer viscosities. ESL viscosities of high purity and industrial AMZ4 are shown in figure 5.5. Nevertheless, this ESL data shows a small difference between the individual viscosities of high purity and industrial AMZ4.

Thus, these investigations of different grades of AMZ4 reveal the following two findings. First, according to ESL measurements material impurities, such as oxygen cause a small difference in the temperature dependent viscosity behaviour (see industrial and high purity AMZ4 in figure 5.5). And second, material impurities influence the Couette rheometer technique. This manifests itself by a factor of two (for AMZ4) larger rheometer viscosity due to sample-container interactions.

In summary, in this section it was shown that ESL in combination with the oscillating drop technique is an accurate and reliable method to determined melt viscosities regardless of the quality of the starting materials. This technique has the advantage of covering a twice as wide temperature range of viscosities than Couette rheometry, namely up to 400 K. In addition, it offers access to the undercooled melt. This means, the ESL technique allows measuring viscosities of the undercooled melt up to 275 mPas. Hence this method is well suited for low viscosity systems. Furthermore, it was shown that the oscillating drop technique, as used in ground based experiments, suffers not disturbances from gravitational effects and that it is free of measuring artefacts, since no mass dependence exists on this method.

The Couette rheometry technique, in contrast measures viscosities up to the Pas range. However, it requires equilibrium melts above the liquidus temperature. This method is hence suited for high viscous systems with low melting points and for systems made of high quality starting materials.

With the knowledge of this section that electrostatic levitation provides reliable and accurate high temperature viscosity data, this method is used in the following to investigate besides viscosity further other thermophysical properties of the melt and undercooled melt of BMGs. Such properties are density, specific volume, thermal expansion and specific heat capacity as well as structural properties.

5.2 High temperature viscosity

Busch et al. [111] found that the high temperature viscosity of Vitreloy 1 exhibits a hysteresis-like behaviour, as shown in figure 5.4. The corresponding data was conducted by Couette rheometry and the finding was interpreted as a result of a strong-to-fragile transition.

In order to investigate whether such behaviour can also be found in other BMG melts the viscosity of the BMG investigated within this work (see section 4.1) is studied using electrostatic levitation in combination with the oscillating drop method. ESL viscosity measurements of this section are performed in accordance with Couette rheometer measurements of Busch et al. [111] on Vitreloy 1. There, different temperature dependencies were obtained for measurements staring from different maximum temperatures. Therefore, for all (ESL) viscosity data obtained in this section, the melt is first heated to a temperature well above T_{liq} (as described in section 4.2.7). The maximum temperatures for homogenising the melt have been randomly altered from 100 to
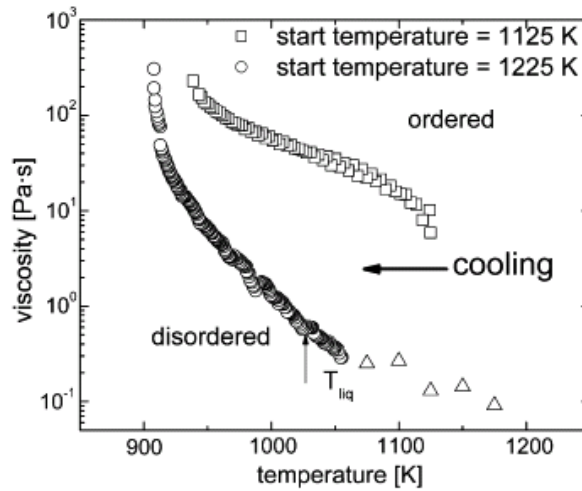
Figure 5.4 – Viscosity as function of temperature for continuous cooling with an average cool-
ing rate of $2\,\mathrm{K\,s^{-1}}$ using a constant clockwise shear rate. When cooling from 1125 K ($\square$), the
viscosity stays about two orders of magnitude higher than when cooled from 1225 K ($\bigcirc$). For
the latter run, the data above 1045 K is not shown since the sensitivity of the torque sensor
does not allow for accurate data. Data in this region ($\triangle$) is represented by isothermal viscosity
measurements. This figure is taken from Way et al., reference [111].

350 K above the respective liquidus temperature for the individual sample systems. The melt was
then cooled to the desired temperature, the temperature was kept constant and the viscosity was
measured. The results are presented in figure 5.5 and figure 5.6 with different axis representa-
tions.

All BMGs investigated show a continuously decreasing viscosity behaviour between 275 and
10 mPas with increasing temperature. They cover a temperature range of ~ 400 K, from around
1100 K to approximately 1500 K. Different BMGs exhibit different temperature dependencies. But
no anomalies in their courses or approaches for a hysteresis are found. Besides, different over-
heating temperature show no effect on the viscosity behaviour.

These results show no similarities to the hysteresis-like behaviour found in the melt of Vitreloy 1
[111]. In order to verify once more that there is no hidden hysteresis in the melt above the liq-
uidus temperature, the viscosity of Vit106a (as an example) is measured also during heating. In
this experiment, viscosity data upon heating is obtained by slowly heating the levitating sam-
ple to a few Kelvin above its calorimetric liquidus temperature, where the viscosity is then de-
termined. (For T_{liq} see table 4.1.) This process is repeated multiple times and each time the
temperature at which the measurement takes place is increased by about 10 K. Viscosities upon
cooling are determined as described in section 4.2.7. The results are depicted in figure 5.7.

The viscosities of Vit106a determined upon heating and cooling show different temperature de-
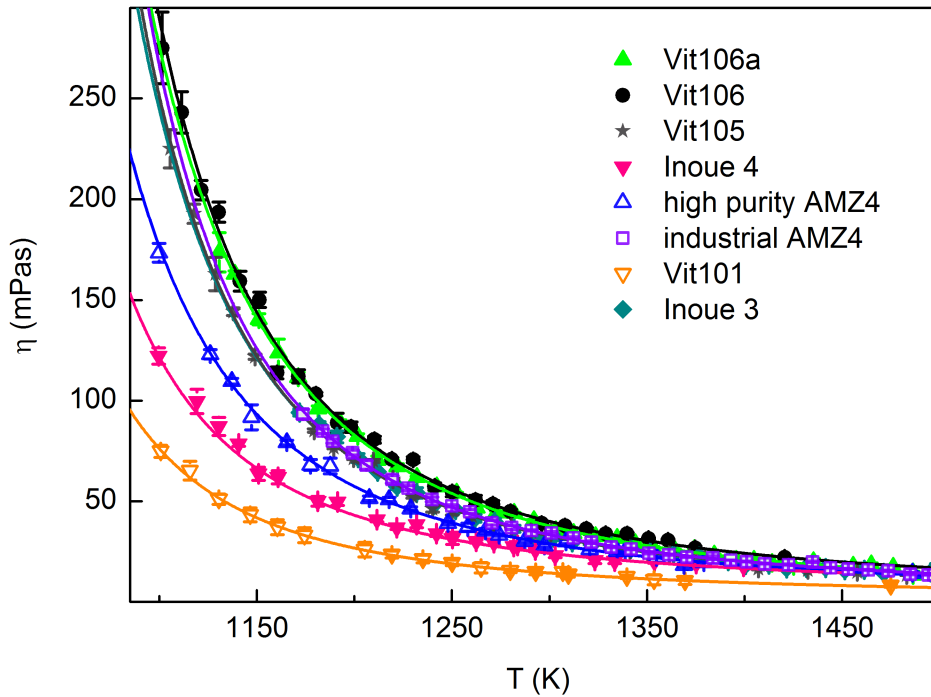
Figure 5.5 – High temperature viscosities of various BMGs determined by electrostatic levitation in combination with the oscillating drop technique.

pendencies below 1160 K. Here, the viscosity data upon heating is approximately 30 mPas higher than the data upon cooling. Above 1160 K both viscosities coincide and decrease monotonically with increasing temperature until just above 1300 K.

According to DSC measurements, the calorimetric solidus and liquidus temperatures of Vit106a are T_{sol} = 1089 K and T_{liq} = 1113 K (See table 4.1). Thus, the temperature of 1160 K is nearly 50 K above T_{liq}. However, these temperatures (T_{sol} & T_{liq}) were determined at a heating rate of 10 K/min. Completing a melting process at this heating rate takes around 144 s. Passing the temperature region of interest, thus from T_{sol} to 1160 K takes accordingly about 420 s.

In ESL viscosity experiments the temperature is controlled manually. This means, the laser power used for heating from below T_g to above T_{liq} depends on the person performing the experiment. For the viscosity experiments performed within this work, heating through the melting process took around 80 - 100 s, while heating from T_{sol} up to ~1160 K took about 150 - 170 s (according to time-temperature profiles of this work).

This means, the time scales for heating from T_{sol} to 1160 K are smaller by a factor of 2.5 - 2.8 in ESL experiments than in DSC measurements. Therefore, the possibility that the Vit106a sample is only partially molten below 1160 K exists, even though it is above its calorimetric liquidus temperature. This could be a possible explanation for the difference in viscosity behaviour upon heating and cooling of Vit106a below 1160 K.
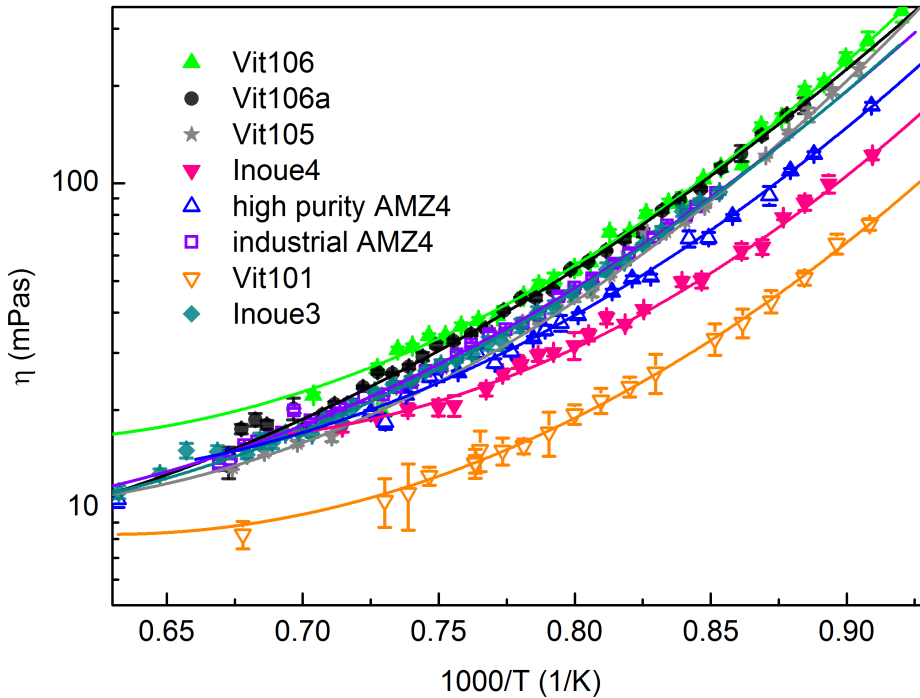
Figure 5.6 – High temperature viscosities of various BMGs determined by electrostatic levitation in combination with the oscillating drop technique. Viscosities are displayed in an Arrhenius plot on a logarithmic scale and as function of their inverse temperature.

Density measurements, for instance provide an easy approach to gather information on crystallisation.

To try this, a density measurement on Vit106a is performed in order to compare time scales of the heating process of Vit106a through the temperature region of interest (T_{sol} to ~ 1160 K) and in combination with density and crystallisation information to time scales of DSC and viscosity experiments. For this, the temperature dependent density was determined upon free radiation cooling from a maximum temperature to below T_g and upon subsequent reheated back to the starting temperature. The resulting density is shown in figure 5.8. The density increases linearly from almost 6.6 to about 6.9 g/cm^3 during cooling from 1550 to 640 K. Upon reheating it deviates from the linear behaviour at around 875 K. Here, the density stays constant upon further heating. This process is directly followed by an abrupt decrease in density at a barely changing temperature between 1090 K and 1105 K. Last, the density decreases linearly until it matches the temperature dependent density upon cooling at around 1160 K. Above this temperature the densities upon heating and cooling coincide.

Upon free radiation cooling of Vit106a no deviations from the linear density behaviour are found, indicating that Vit106a was cooled into its glassy state without crystallisation setting in. This is
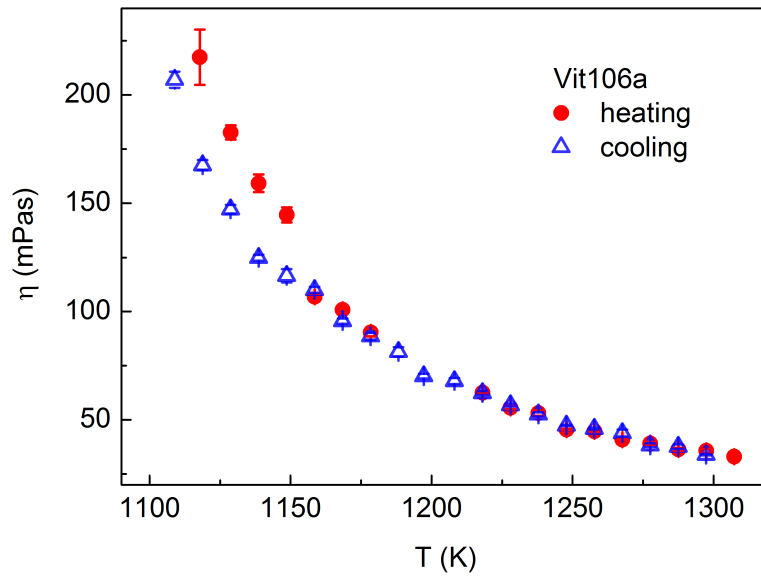
Figure 5.7 – Viscosities of Vit106a measured with the ESL technique upon heating from the solid
state (red circles) and upon cooling from the homogenised melt (blue triangles).

later confirmed by x-ray experiments in section 5.10. Upon heating, the glass crystallises first
before melting takes place. This is clearly visible in figure 5.8. The crystallisation process sets
in at 875 K. It is accompanied by an release in crystallisation energy, thus a sudden increase in
temperature, which becomes visible in a low data rate per time between 895 K and 1040 K. The
crystallisation process is directly followed by the melting process, which sets in at 1090 K. This
is in excellent agreement with DSC experiments, where T_{sol} was determined to be 1089 K and
indicates the beginning of the melting process. However, upon passing the calorimetric liquidus
temperature of 1113 K the densities upon cooling and reheating do not coincide. This indicates
that there might still be crystalline parts present (between T_{liq} and ~ 1160 K). When taking a look
at the time necessary for melting Vit106a and heating it until 1160 K, it is found that this takes
only about 5 to 6 s in density measurements. Meaning that the temperature region of interest
in density experiments is passed about 25 - 35 times faster than in viscosity measurements and
70 - 85 times faster than in DSC experiments with a heating rate of 10 K/min.

But while it is possible to determine densities for viscosities upon cooling, it is not possible to
do so for viscosities upon heating. Here, no assurance that the sample is completely in its liquid
state exists and thereby the axial symmetry around the sample's vertical axis, which is necessary
for a density measurements is not guaranteed either. (For requirements of density measurements
see section 4.2.3.)

It is hence, assumed that crystalline parts still remain in the otherwise molten liquid between
T_{liq} and 1160 K, because there is simply not enough time to complete an entire melting process.
Above 1160 K time and temperature are obviously sufficient to complete the melting process of
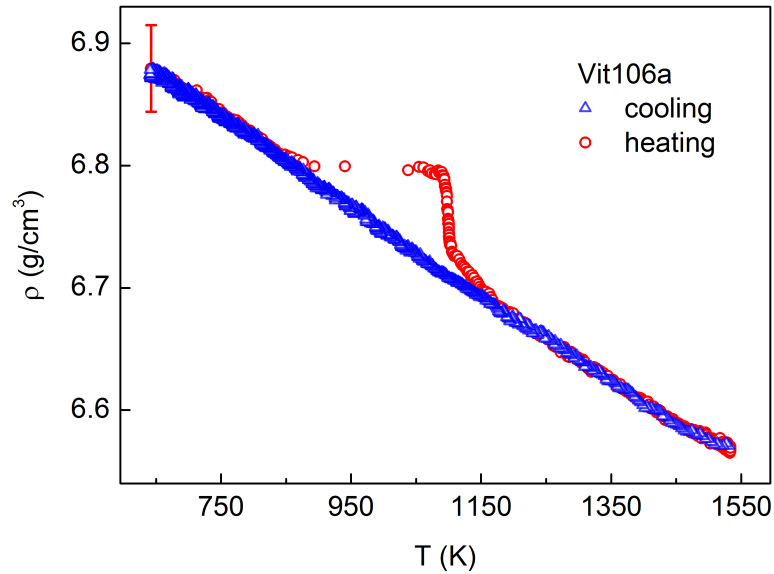
Figure 5.8 – Density of Vit106a measured upon free radiation cooling (blue triangles) from the melt throughout the undercooled state to below T_g and upon subsequent reheating (read circles) back to the starting temperature. Crystallisation and melting of the sample upon reheating are clearly visible and set in around 875 K and at 1090 K, respectively.

Vit106a. Since, both density and viscosity experiments provide coinciding results above 1160 K for heating and cooling processes it is concluded that the viscosity measurement upon heating and below 1160 K faces a similar issue of remaining crystalline parts in the melt than the density measurement. It is therefore concluded that these crystalline parts falsify the viscosity measurement. Furthermore, the viscosity of a mixture of solid and liquid states is usually larger than the viscosity of a pure liquid state. The different temperature dependencies in the viscosity of Vit106a below 1160 K are hence caused by an crystallisation issue and not by thermophysical properties of Vit106a.

In summary, melt viscosities of several Zr based BMGs were conducted using electrostatic levitation in combination with the oscillating drop technique. The resulting viscosities reveal no indication for a hysteresis-like behaviour as found in the melt of Vitreloy 1 by [24]. Additional experiments on the example of Vit106a and upon heating from the solid state showed that at temperatures just above the calorimetric liquidus temperature crystallisation can influence viscosity measurements. This finding demonstrates the importance of homogenising the melt before conducting viscosity experiments.

Altogether no indications for a liquid-liquid transition were found in the high temperature viscosities of the investigated BMGs. Therefore, other parameters like density, packing fraction, thermal expansion, or heat capacity, will be investigated in the following, to see whether they

show indications for a possible transition.

5.3   High temperature density

Besides viscosity, density is taken into account, as a possible parameter which might give information on the liquid-liquid transition. Density is a material property which can be tracked throughout the undercooled state using the ESL technique. It is therefore used to check whether any unusual or distinctive features in the undercooling region exist.

Here, the temperature dependent densities of the investigated BMGs (see section 4.1) are measured according to the description of section 4.2.3. A measurement of the temperature dependent density during a complete heating and cooling cycle, thus upon cooling from the equilibrium melt to below T_g and subsequent reheating back to the starting temperature was already shown in figure 5.7 (right) and discussed.

In this section only temperature dependent density measurements upon cooling from the equilibrium melt are presented because the path upon reheating is masked by crystallisation. Hence, the lowest temperature until which density can be tracked is determined by the onset temperature of crystallisation. Only in the case of Vit106a and Inoue 4 is it possible to track the density until temperatures in the vicinity of T_g, since these BMGs can be vitrified below T_g. Only here, is the cooling rate, which corresponds to free radiation cooling sufficient to vitrify the BMGs. For the remaining BMGs the cooling rate (upon free radiation cooling) is too small to vitrify them below T_g.

Figure 5.9 shows the temperature dependent densities of the investigated BMGs upon cooling determined by using the ESL technique. (For information on the method see section 4.2.3.) According to the respective time-temperature profiles no crystallisation occurred during these measurements. Besides, an entire or mostly entire crystallisation process of a sample is accompanied by a pronounced change in density, as illustrated in figure 5.7 (right) upon reheating at around 950 - 1090 K. In this section, the densities displayed in figure 5.9 are those of liquids or glasses of the alloys.

All densities increase linearly with decreasing temperature. The individual measurements show no deviations from their linear behaviour. Even Vit106a, which was cooled to below its glass transition temperature, shows no distinctive signs indicating a transition or crystallisation.

Except for Vit101 all densities show an equal slope at different absolute values. Vit101, which is a Co-Ti based system, shows a slightly different temperature dependency.

In conclusion, temperature dependent densities of the investigated BMGs upon free radiation cooling from the equilibrium melt and throughout the undercooled state were investigated. The individual densities revealed no deviations from a linear behaviour and thus, show no indications for a transition. Therefore, two scenarios are possible. Either no transition occurs in the inves-
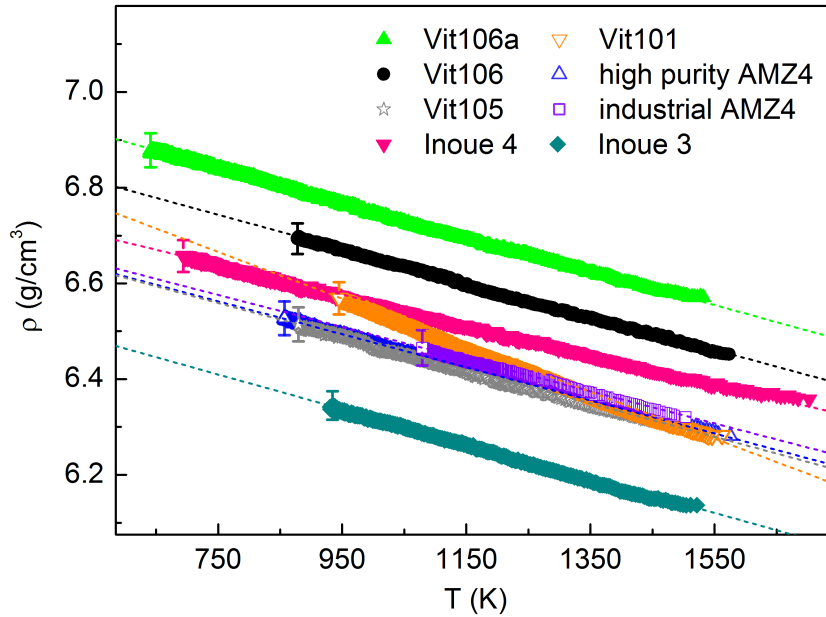
Figure 5.9 – Densities of the BMGs investigated within this work determined upon free radiation cooling from the equilibrium melt and throughout the undercooled state. Experiments are conducted using electrostatic levitation.

tigated BMGs between T_{liq} and T_g, or a transition exists, but is not associated with a change in density. In either cases, density gives no information on a strong-to-fragile transition or the underlying mechanism.

5.4 Comparison of viscosity, atomic volume, and packing fraction

Up until here, the BMGs introduced in section 4.1 are investigated in terms of their density behaviour of the melt and undercooled state as well as in terms of their melt viscosities. In order to characterise possible classifications and relations within the investigated BMGs the parameters studied are used to calculate the averaged atomic volume and the packing fraction at different temperatures, namely at 1250 K and at the respective liquidus temperature of the individual BMGs. This data is displayed in combination with corresponding viscosity data and liquidus temperatures.

In addition, data on Vitreloy 1 is given [118]. According to Way et al. [111] the melt viscosity of Vitreloy 1 shows indications for a strong-to-fragile transition and therefore Vitreloy 1 serves as comparison.

Furthermore, Yuan et al. [120] found that the melt viscosity increases upon alloying Al. This finding will also be considered and reviewed for the investigated BMGs in the following. Further
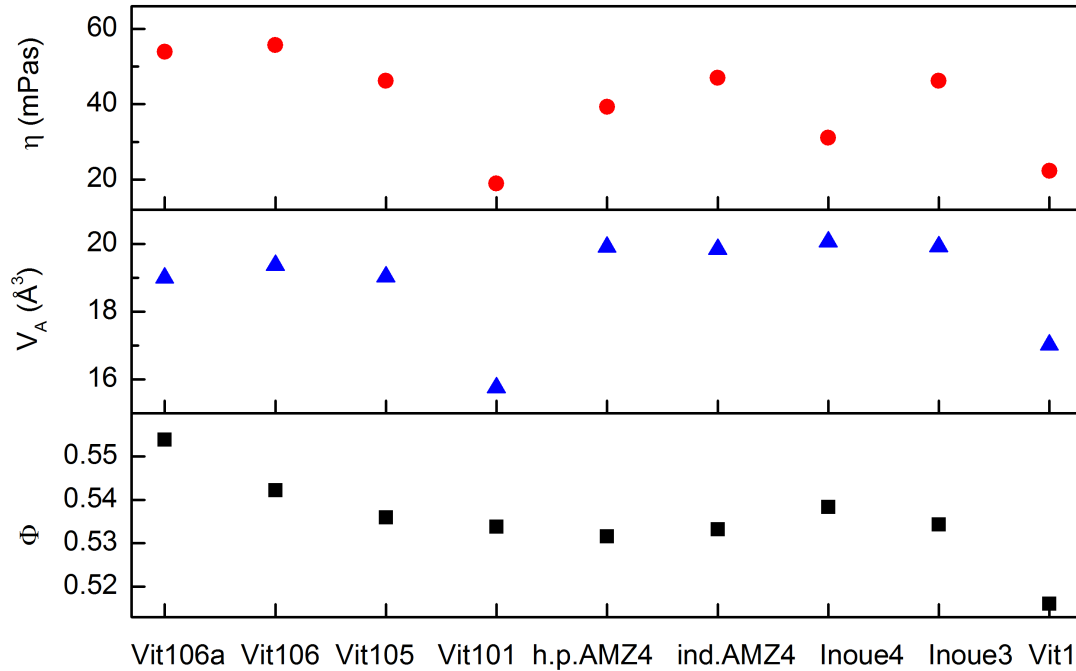
Figure 5.10 – Comparison of viscosity (η), averaged atomic volume (V_A), and packing fraction (Φ) of the investigated BMGs as well as of Vitreloy 1 [118] at 1250 K.

aspects of discussion are the number of components in the BMGs [98] and the glass forming ability, in terms of undercooling properties in ESL experiments.

Figure 5.10 shows viscosity (η), averaged atomic volume (V_A), and packing fraction (Φ) of the investigated BMGs as well as of Vitreloy 1 at 1250 K. Viscosities vary between 20 and 55 mPas, while the atomic volumes vary between 15 and 20 Å^3. The packing fractions cover a range of 0.51 to 0.55.

Vit106a, Vit106, Vit105, AMZ4, as well as Inoue 3 and 4 show a high viscosity compared to the remaining BMGs Vit101 and Vitreloy 1. These two BMGs exhibit a clearly lower viscosity and contain no Al. Hence, this finding is consistent with the finding of Yuan at al. [120] in Zr-(Cu,Ni)-Al alloys. However, it is not clearly recognisable from figure 5.10 that the viscosity increases with the amount of Al. Inoue 3, which possesses the largest amount of Al (15 %) displays a lower viscosity than for example Vit106a, Vit106, or Vit105, which all contain 10 % Al.

Vit106a, Vit106, Vit105, AMZ4, as well as Inoue 3 and 4 also exhibit a larger atomic volume than Vit101 and Vitreloy 1. Thus, the BMGs containing no Al show a lower atomic volume.

The packing fraction is defined as volume of atoms per averaged atomic volume. For Vit101 and Vitreloy 1 the packing fractions show no comparable correlation. Vit101, for instance displays a similar packing fraction than other Al-containing BMGs, such as Vit105 or Inoue 3, while Vit-

reloy 1 exhibits by far the lowest packing fraction among the investigated BMGs.

Thus, similar to Zr-(Co,Ni)-Al alloys [120] the presence of Al increases the viscosity and provides a larger atomic volume. However, this finding gives no quantitative relations (at least not within the Al concentration range (7.5 - 15 %) investigated).

Next, figure 5.10 is discussed in terms of the number of components of the respective BMGs. The viscosity of the five component systems (Vit106, Vit106a, and Vit105) is among the highest viscosities, while viscosities of the four and three component systems (AMZ4, Inoue 3, and 4) are on average slightly lower. No difference between three and four component BMGs are visible. Yet, this finding only holds for Zr-Cu based BMGs. In addition, the differences in viscosity (of the Zr-Cu based BMGs) are not particularly pronounced, viscosities for Vit105 (five components), industrial AMZ4 (four components), and Inoue 3 (three components) for instance do coincide.

The corresponding atomic volumes can be categorised in two groups (for the Zr-Cu based BMGs). One group is formed by the five component BMGs and displays an atomic volume of ~ 19 Å^3, while the other group is formed by the three and four component BMGs and exhibits an atomic volume of ~ 20 Å^3. Again, no difference between three and four component systems is found. However, a correlation between viscosity and atomic volume seems to exist.

No categorisations can be applied to the packing fractions. The packing fractions of the five component BMGs already cover almost the full range. In contrast to this, Vit105, Inoue 4, and Inoue 3, which are five, four, and three component systems respectively possess similar packing fractions, but different viscosities. Thus, the amount of components tends to increase the viscosity and leads to a grouping of atomic volumes within one base system. However, no difference between three and four component glasses is found. No correlation has been found between the amount of components and the packing fraction.

In order to derive the packing fraction from the macroscopic density, thus the experimentally determined density two assumptions are made. First, atoms are statistically distributed. And second, a certain radius is assumed for the individual atoms when calculating the volume. In this case, covalent radii of Pauling [82] were taken. This choice, however is arbitrary. It also means that chemical short range orders as discussed by Voigtmann et al. [110] are not reflected. Despite these assumptions, this approach works quite well when calculating the packing fraction in Pd-Ni-P alloys [25]. Here, constant packing fractions entail similar dynamics and an increase in the packing fraction leads to slower dynamics. This is reflected in an increasing viscosity.

The presence of Al in an alloy, however qualitatively violates this correlation. Yuan et al. [120] found that the melt viscosity increases upon alloying Al. However, this increased viscosity is not related to an increased packing fraction, but rather to an reduction in the packing fraction. Yuan et al. [120] found further that chemical interactions of Al with transition metal atoms cause liquid dynamics of metallic melts to slow down. Additionally, a strong bonding between Al and Cu atoms was found by Cheng et al. [27], which they claimed results in a shorter interatomic distance between these two atoms. Thus, the presence of Al in glass-forming alloys violates the
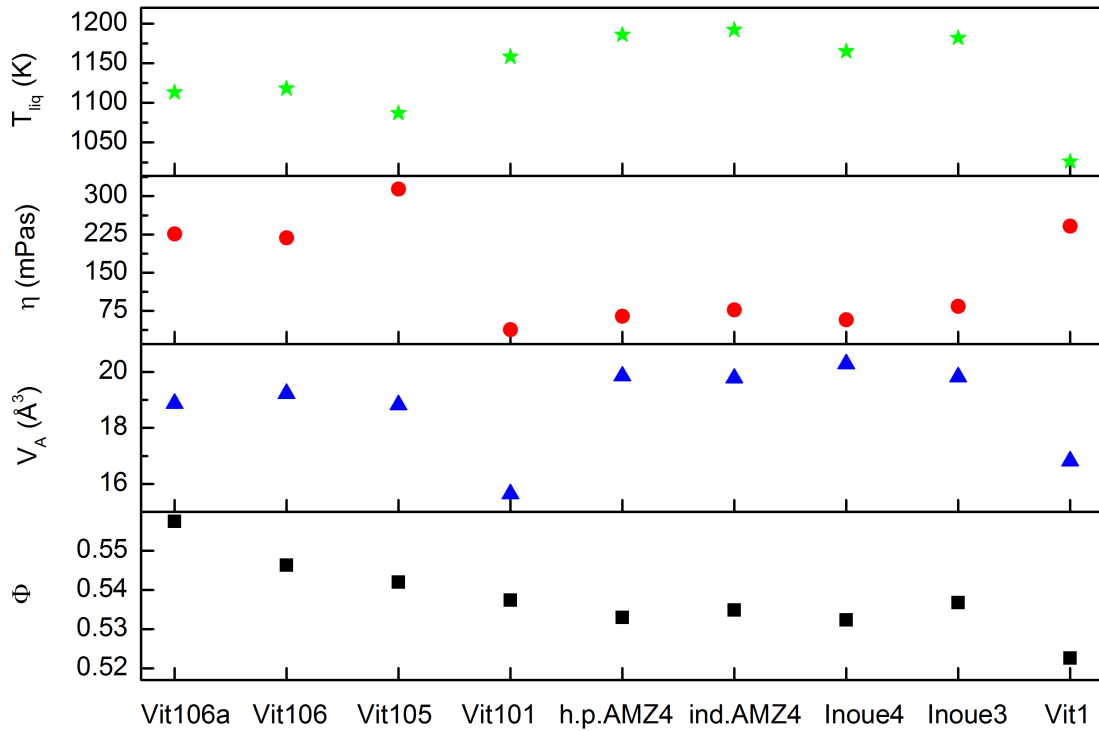
Figure 5.11 – Comparison of viscosity (η), averaged atomic volume (V_A), packing fraction (Φ), and liquidus temperature (T_{liq}) of the investigated BMGs as well as of Vitreloy 1 [118] at the liquidus temperature.

conditions assumed above for calculating the packing fraction.

In the investigated BMGs it is found that the packing fraction does not correlate with the viscosity. Even the atomic volume, which contains no radii assumptions does not seem to correlate either. This is in contrast to the finding made in Pd-Ni-P alloys [25] and suggest a pronounced chemical short range order.

Holland-Moritz et al. [49] found that Ni atoms preferably accumulate to Zr atoms in the liquid state. Recent findings of Peng et al.[84] on liquid Al-Au alloys report that the effective atomic size of Al depends on the local environment of the Al atom, meaning that the size depends on the composition of the mixture [84].

These literature findings suggest some sort of accumulation between certain types of atoms and even a bond shortening between specific types of atoms in the liquid state due to chemical interactions.

In conclusion , this considerations proposes that chemical interactions contribute to liquid structure and dynamics via chemical short-range order. This, in turn leads to the conclusion that a difference in viscosity (or atomic volume) can not be explained by simple packing effects or vice versa, not even when taking into account the number of components or the Al content.

Viscosity, atomic volume, and packing fraction are compared once more in the following. This time at the respective liquidus temperatures of the individual BMGs and with respect to this temperatures. The data is shown in figure 5.11. Viscosities vary between 38 and 315 mPas, while the atomic volumes still vary between 15 and 20 Å^3. The packing fractions cover a range of 0.52 to 0.56 and the liquidus temperatures are found in between 1026 and 1192 K. This time, viscosities vary more, while the atomic volumes and calculated packing fractions remained almost unchanged in comparison the figure 5.10.

First, figure 5.11 is discussed in terms of number of components. Here, it is noteworthy that viscosity of five component BMGs is at least greater than 200 mPas, regardless of the base system. Viscosities of three and four component BMGs are significantly lower, namely in the range between 40 to 85 mPas. This finding indicates that the amount of components increases the viscosity at the liquidus temperature.

When taking a look at the liquidus temperatures it becomes obvious that T_{liq} decreases with an increasing number of components. The five component BMGs display liquidus temperatures between 1026 and 1118 K, while three and four component BMGs exhibit liquidus temperatures between 1158 and 1192 K.

The atomic volume, however is virtually unchanged in comparison to figure 5.10. Five as well as three and four component BMGs still form two groups of atomic volumes of ~ 19 Å^3 and ~ 20 Å^3, respectively. No difference between three and four components systems is found. However, this finding only holds for Zr-Cu based BMGs. It is therefore concluded that the atomic volume does not depend on T_{liq}.

The corresponding packing fractions show no connection to the amount of components. Since the previous discussion dealt with possible reasons for this phenomenon, the packing fraction is not discussed at this point.

These considerations showed that no universal viscosity, atomic volume, or packing fraction exists at the liquidus temperature.

Next, figure 5.11 is discussed in terms of the glass forming ability in ESL undercooling experiments. For Vit106a, Inoue 4, and Vitreloy 1 the cooling rate corresponding to an ESL free radiation cooling experiment is large enough to vitrify these BMGs below T_g. Vit106a and Vitreloy 1 exhibit a high viscosity at T_{liq} (in comparison to the remaining BMGs). This could facilitate the glass formation. Inoue 4, however is the exception, since it displaying a much lower viscosity of 57 mPas.

Thus, the glass forming ability depends strongly on the individual composition of the BMG and can not be explained generally.

In summery, the comparison of viscosity, atomic volume, packing fraction, and liquidus temperature at different temperatures showed that in general the amount of Al increases the absolute viscosity, but enlarges the atomic volume. Meaning Al causes a more loose packing density in a viscous system. Further packing considerations revealed that the packing fraction is dominated

by effective atomic sizes, which depend on the composition of the BMG. It was also found that the amount of components in glass-forming alloys decreases the liquidus temperature, which in the case of the investigated BMGs leads to an increased viscosity at T_{liq}. These findings lead to the conclusion that chemical interactions play an important role in liquid structures and dynamics.

5.5   Determination of high temperature fragilities

The fragility concept as proposed by Angell [5] is used to describe the degree of deviation from the Arrhenius behaviour. Therefore, fragility is often referred to as steepness index [113].
In this section, the high temperature fragility is determined from different melt viscosities. This is done on the example of Vit106a and with respect to the VFT-fit performance and uncertainty.

For this, three sets of experimentally determined viscosity data are used, as shown later on in figure 5.12 and 5.13. They are determined using ESL in combination with the oscillating drop technique (red circles, this work) as well as Couette rheometry. The rheometer data is taken from W. Hembree [47] (filled black triangles) and Evenson et al. [38] (open blue square).
All three measurements show continuously decreasing viscosities with increasing temperatures, but with different temperature dependencies. To determine this relation precisely in experiments is of great challenge as discussed earlier in section 5.1. To what extent these different temperature dependencies influence a VFT-fit and the resulting fragility is estimated in the following.

As a first step, all three data sets are fitted with a VFT-fit according to the following equation:

$$ln\left(\eta\right) = \ln\left(\eta_0\right) - \left(\frac{E_A}{k_B \cdot (T - T_0)}\right) . \tag{5.1}$$

Here, η is the viscosity, η_0 is 4×10^{-5} Pas, E_A the activation energy, k_B the Boltzmann constant, T the temperature, and T_0 the temperatures at which the barriers with respect to flow would approach infinity [5].
All three fits are performed in an identical manner and assuming η to be 10^{12} Pas at T_g. The fit results are displayed in table 5.1.

	ESL (this work)	W.Hembree [47]	Evenson et al. [38]
T_0 (K)	530.6 ($\pm$ 1.2)	534.4 ($\pm$ 2.4)	536 ($\pm$ 0.7)
D^*	9.9 ($\pm$ 0.22)	9.6 ($\pm$ 1.07)	9.4 ($\pm$ 0.22)

Table 5.1 – VFT-fit parameters, namely the VFT-temperatures, T_0 and fragility parameters, D^* of three different data sets of Vit106a. Parameters are determined assuming $\eta = 10^{12}$ at T_g.

Values for T_0 and D^* are similar for all three data sets, but not necessarily within the error bars. T_0 values are between 530 and 536 K, while fragilities vary between 9.4 and 9.9. Still, results of the

different measurements are roughly in agreement with each other. However, when taking a look at the individual VFT-fits through the experimentally determined data, as done in figure 5.12 it becomes obvious that the fits don't match the data very well. The fits barely reflect the individual slopes, hence the different temperature dependencies.
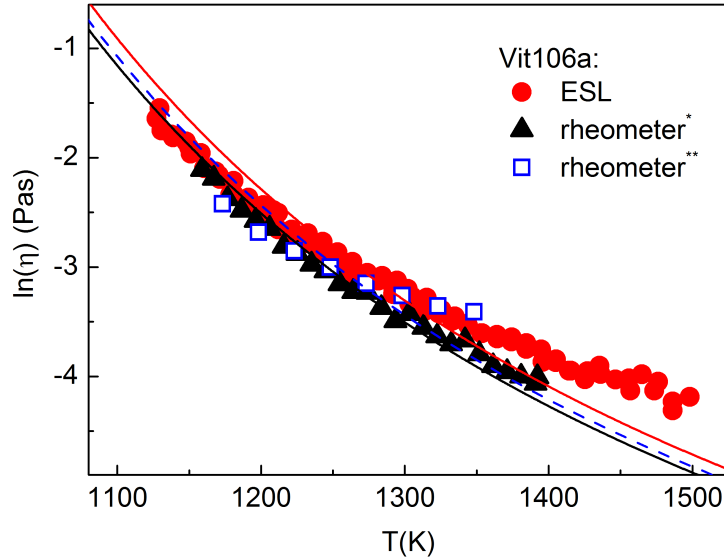

Figure 5.12 – Three different viscosity measurements of Vit106a, obtained by ESL in combination with the oscillating drop technique (red circles, this work) and Couette rheometry (black tri-angles, * Hembree [47] and open blue squares, ** Evenson et al. [38]). VFT-fits are performed according to equation 5.1 and assuming $\eta = 10^{12}$ Pas at T_g.

According to the fit parameters the absolute error of the VFT-temperature, T_0 is within 1.2, 0.7, and 2.4 K for the experiment performed within this work, the data of Evenson et al.[38], and the data of W. Hembree [47], respectively. The absolute error of the fragility parameter D^* is within 0.22 for the experiment performed within this work and the data of Evenson et al.[38] and within 1.07 for the data of W. Hembree [47]. However, these uncertainties refer only to the estimated standard deviations of the VFT-fits and do not reflect the quality of the fit.

In order to improve the quality of the VFT-fits the fit function (as given in equation 5.1) is al-tered. First, η_0 which is set to be 4×10^{-5} Pas for many metallic glass formers [22, 96], was set free. However, this barely changed the fit quality (not shown). η_0 kept values between 1×10^{-4} and 3×10^{-5} Pas. Therefore η_0 was set back to 4×10^{-5} Pas for further tests. Next, the fitting was repeated without a given value for the viscosity at T_g. This time, the individual relations of vis-cosity to temperature are much better reflected by the fits, as shown in figure 5.13.

The corresponding VFT-parameters are displayed in table 5.2. T_0 varies in between ~ 0 and 416 K, while D^* varies between 14.2 and 23.1. The data of Evenson et al. [38] yields no physical mean-ing for D^*.
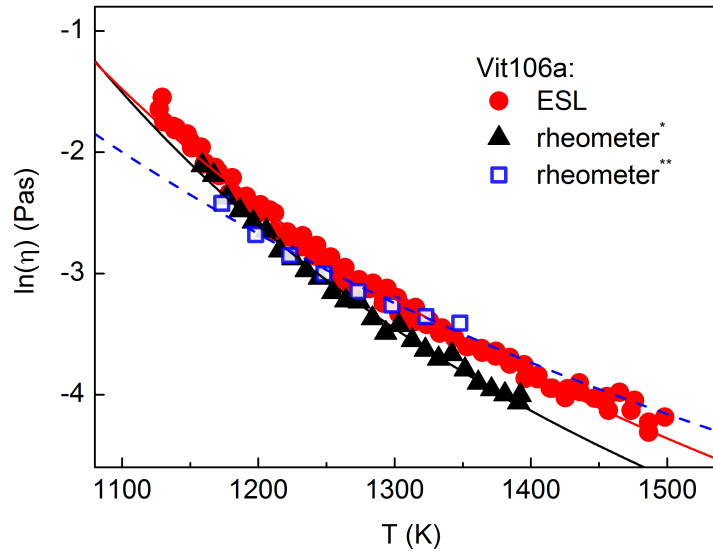
Figure 5.13 – (left) High and low temperature viscosities of Vit106a with individual VFT fittings assuming no fixed value for T_g. Low temperature data was obtained by three point beam bending [37], while high temperature data was obtained by Couette rheometry [38, 47] and ESL technique (this work).

(right) Close up of the temperature range from 1100 K to 1500 K.

Here, T_0 and D^* values cover a far greater range when assuming no given value for η at T_g, even though experimental data is unchanged. Additionally, the fittings show a great uncertainty in reproducing the fragility.

This uncertainty, however is mathematically justified, since the fragility reflects the slope of the fit at T_g. High temperature data varies only over one order of magnitude. This stands in contrast to the low temperature data, which varies over three orders of magnitude. Hence, high temperature fitting parameters are barely defined and offer a by far greater range of possible fitting options. Fitting errors are found to increase by a factor of 10. This is reflected in the respective fragilities and VFT-temperatures of table 5.2. This table shows that if no reference value, such as η at T_g is assumed, the high temperature fragility can not be determined reliably and reproducibly from a VFT-fit.

This means the effort to determine high temperature viscosities accurately, as discussed in section 5.1 is not reflected in VFT-fits.

In conclusion, high temperature VFT-fits always need a reference value at clearly lower temperature such as in the vicinity of T_g. But, even if the high temperature VFT-fits possess such a reference value, the absolute values of the high temperature fragility D^* possess a great uncertainty of up to 11% of D^*. The accuracy of experimentally determined viscosity-temperature dependencies is not necessarily reflected correctly by VFT fittings.

	ESL (this work)	Hembree [47]	Evenson [38]
T_0 (K)	300 ($\pm$ 10.7)	415.4 ($\pm$ 13.8)	(-3.58 ($\pm$ 78.5))
D^*	23.1 ($\pm$ 7.5)	14.2 ($\pm$ 3.38)	n/a

Table 5.2 – VFT-fit parameters, namely the VFT-temperatures, T_0 and fragility parameters, D^* of three different data sets of Vit106a. Parameters are determined assuming no given value for η at T_g.

5.6 High temperature fragility

In this section, the fragility is derived from the experimentally determined melt viscosities of all investigated BMGs and as displayed in figure 5.5. This is done despite the great uncertainties in high temperature VFT-fits, as discussed in the previous section.

Shadowspeaker et al. [98] found that in Ni-Nb based metallic glass-forming alloys the fragility parameter, D^* increases monotonically with the number of components. A similar trend was found for the fragility of Zr-based alloys [98]. This finding is reviewed in the following. Furthermore, the fragility data is compared to another set of high temperature data determined from Couette rheometer measurements by W. Hembree [47].

For this purpose, the individual melt viscosities determined in this work (and as shown in figure 5.5) are displayed on a logarithmic scale and as a function of their inverse temperature, normalised with respect to their individual glass transition temperature. Such Angell plot is shown in figure 5.14.

The individual viscosities all show a monotonically decreasing viscosity behaviour with increasing temperatures. However, they form two groups, each with its own temperature dependence and thus (similar) fragility. This arrangement in groups occurred, even though individual and absolute viscosities vary from each other (as can be seen in figure 5.5) as well as individual glass transition temperatures (for T_g see table 5.3). Within one fragility group, T_g varies up to 50 K. Vit101 and high purity AMZ4 form one fragility group, while the remaining BMGs form the other group. At first sight, it is not apparent according to which criteria these different fragility groups form. In any case the formation is not caused by the presence of Al, since high purity AMZ4 contains Al and Vit101 doesn't. Also the number of components is no criterion, since five (Vit106a,Vit106,Vit105), four (Inoue4, industrial AMZ4), and three (Inoue3) component BMGs form one fragility group.

The high temperature fragility values (D^*) are determined from the data of figure 5.14 and via the Vogel-Fulcher-Tammann equation (see equation 2.3). The resulting fragilities as well as the corresponding T_0's are given in table 5.3 along with individual glass transition temperatures. Ad-
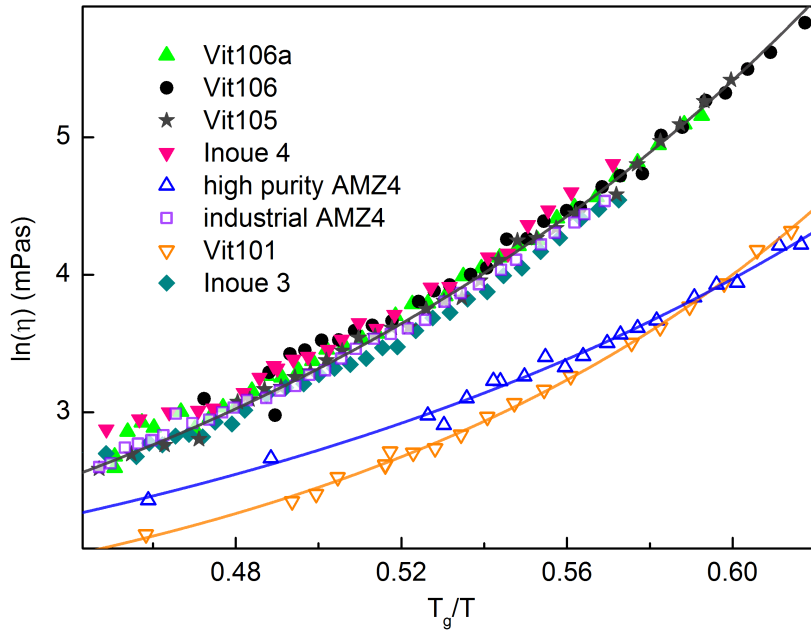
Figure 5.14 – Melt viscosities of the investigated BMGs determined by electrostatic levitation in combination with the oscillating drop technique. Viscosities are displayed on a logarithmic scale and as function of their inverse temperature, normalised with respect to their individual glass transition temperatures.

ditionally, high temperature fragility parameters determined from Couette rheometer measurements of W. Hembree [47] are given.

The fragility parameter D* determined from ESL experiments confirms the formation of two groups of similar fragilities. High purity AMZ4 and Vit101 exhibit a fragility parameter of 7.3 and 7.5, respectively, while the remaining BMGs exhibit a fragility parameter of around 10.

Such clear division in different groups is not reflected in the fragility parameters determined from Couette rheometer experiments of [47]. Here, D* values vary between 7.4 for high purity AMZ4 and 17.4 for Vit101. Couette rheometer and ESL fragilities of Vit106a, Vit106, Inoue3, Inoue4, and high purity AMZ4 are in agreement, while fragility parameters of Vit101, Vit105, and industrial AMZ4 deviate from each other.

The reason for these differences are found in the VFT-fit performance (as discussed in detail in section 5.5) as well as in the respective experimental data obtained by the two different methods ESL and rheometry. They provide slightly different viscosity values and cover different temperature ranges, as discussed in section 5.1. Couette rheometry covers a smaller temperature region than the ESL technique. The smaller temperature range leads to a larger uncertainty in the fit parameters, as reflected in the uncertainties given for Couette rheometer fragilities in table 5.3.

Shadowspeaker et al. [98] found that in Nb-Ni based alloys the fragility parameter D* increases with the number of components. This finding is reviewed for the high temperature fragilities

	T_g (K) $^a_{DSC}$	T_0 (K) $^b_{ESL}$	D^{*b}_{ESL}	T_0 (K) $^c_{rheometer}$	$D^{*c}_{rheometer}$
Vit106a	670	530(± 1.2)	9.9(± 0.2)	536(± 0.7)	9.4(± 0.23)
Vit106	671	533(± 1.4)	9.8(± 0.34)	526(± 3.3)	10.4(± 1.2)
Vit101	676	564(± 1.6)	7.5 (± 0.53)	462(± 10.6)	17.4(± 3.99)
Vit105	663	527(± 1.3)	9.8(± 0.44)	(266(± 21.9))	(55(± 55))
Inoue 3	671	532(± 1.9)	9.8(± 0.6)	522(± 3.6)	10.7(± 1.4)
Inoue 4	628	494(± 1.5)	10.2(± 0.58)	497(± 1.4)	9.9(± 0.54)
AMZ4 (ind.)	668	533(± 1.2)	9.6(± 0.43)	514(± 2.1)	11.3(± 0.81)
AMZ4 (h.p.)	726	608(± 2.3)	7.3(± 0.6)	606(± 1.6)	7.4(± 0.41)

[a] Determined by DSC at 10 K/min at the DLR, Cologne.

[b] High temperature parameters determined from ESL experiments (this work).

[c] High temperature parameters determined from rheometry experiments by W. Hembree [47]

Table 5.3 – High temperature VFT-fit parameters as well as calorimetric glass transition temperatures of the investigated BMGs determined from ESL, Couette rheometer, and DSC experiments.

given in table 5.3 and determined from ESL viscosity experiments. The three component glass Inoue3 exhibits a fragility parameter of 9.8. The four component systems Inoue4 and industrial AMZ4 possess a similar fragility of 10.2 and 9.8, respectively. Only high purity AMZ4 displays a clearly lower fragility of 7.3. The remaining five component glasses Vit106a, Vit106, and Vit105 exhibit a fragility of 9.9 or 9.8. This shows that the fragility stays constant with increasing number of components in Zr-Cu based BMGs.

Thus, the finding of Shadowspeaker et al. [98] for Nb-Ni based alloys can not be transferred to Zr-Cu based alloys.

In conclusion, high temperature fragilities were determined from experimental ESL viscosity data of the investigated BMGs. It was found that the investigated BMGs form two different fragility groups with different temperature dependencies. The reason for this is not apparent, but does neither depend on the Al content nor on the number of components.

5.7 High and low temperature fragilities

In this section the fragility concept is used once again. This time, to combine high and low temperature fragilities. This is done despite the large uncertainties of the absolute high temperature fragilities, as discussed in the previous section.

For this, the high temperature viscosities of Vit106a, as discussed in the previous section (5.6) are combined with low temperature viscosities of Vit106a from Evenson et al. [38]. Data, as well as the corresponding VFT-fits are presented in figure 5.15.
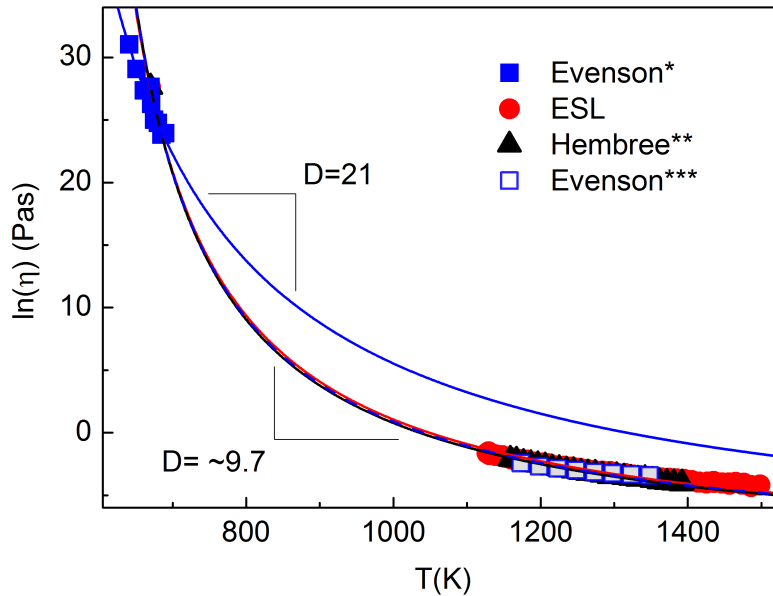
Figure 5.15 – High and low temperature viscosity data of Vit160a with individual VFT-fittings assuming η to be 10^{12} Pas at T_g. Low temperature data (filled blue squares) is taken from (*) Evenson et al. [38] and is determined by three point beam bending, while high temperature data is obtained by Couette rheometry (black triangles: (**) W. Hembree [47], open blue squares: (***) Evenson et al. [38]) and ESL technique (red circles: this work).

The low temperature viscosities of Evenson et al. [38] are determined by three point beam bending in the vicinity of T_g, while the high temperature data is taken from Couette rheometer experiments of (**) W. Hembree [47] and (***) Evenson et al. [38] as well as from ESL experiments performed within this work. Both (high and low temperature) data sets are fitted using equation 5.1. From these fits, the fragility was determined to be $D = 21$ for the low temperature data and $D = ∼ 9.7$ for the high temperature data. Figure 5.15 shows clearly that viscosities between 600 and 1500 K can not be fitted using one VFT-fit. High and low temperature fragilities do not match. Not even when taking the large uncertainty of the high temperature fit into account. The reason for this is not apparent.

This finding was also made by Evenson et al. [38], not only for Vit106a but also for Vit106, Vit105, and Vit101. In the following, this finding is reviewed for all investigated BMGs. High and low temperature fragilities as well as fit parameters are displayed in table 5.4 using the data obtained by ESL experiments within this work and by three point beam bending experiments of W. Hembree [47] and Evenson et al. [38].

	T_0 (K) $^a_{3PBB}$	D^{*} $^a_{3PBB}$	T_0 (K) $^b_{ESL}$	D^{*} $^b_{ESL}$
Vit106a	409	24.1 [38]	530($\pm$ 1.2)	9.9($\pm$ 0.2)
Vit106	343	36.9 [38]	533($\pm$ 1.4)	9.8($\pm$ 0.34)
Vit101	473	16.1 [38]	564($\pm$ 1.6)	7.5($\pm$ 0.53)
Vit105	435	20.5 [38]	527($\pm$ 1.3)	9.8($\pm$ 0.44)
Inoue 3	406	24.1	532($\pm$ 1.9)	9.8($\pm$ 0.6)
Inoue 4	373	24.8	494($\pm$ 1.5)	10.2($\pm$ 0.58)
AMZ4 (ind.)	396	25.6	533($\pm$ 1.2)	9.6($\pm$ 0.43)
AMZ4 (h.p.)	395	24.8	608($\pm$ 2.3)	7.3($\pm$ 0.6)

[a] Low temperature data determined by three point beam bending from Evenson et al. [37, 38] and W. Hembree [47].
Fittings are performed and revised by W. Hembree.
[b] High temperature parameters determined from ESL experiments within this work.

Table 5.4 – High and low temperature VFT-fit parameters of the investigated BMGs determined from three point beam bending ([38, 47]) and ESL experiments experiments.

Table 5.4 presents high temperature fragilities determined from ESL viscosities of this work as well as low temperature fragility data taken from Evenson et al. [37, 38] and W. Hembree [47]. Low temperature fragilities of three point beam bending experiments cover a range of $D^{*} = 16.1$ - 36.9 and show a stronger behaviour than ESL high temperature fragility parameters, which are more fragile and cover a smaller range of $D^{*} = 7.3$ - 10.2. In all the investigated BMGs high and low temperature fragilities do not match. Here, the difference in fragility is by far larger than the uncertainty in the high temperature fragility. Hence, the difference in high and low temperature fragility lies outside the error of determining the high (and low) temperature fragility.

For Vit106a, Vit106, Vit105, and Vit101 this finding is interpreted as a strong-to-fragile transition [38], which gives rise to an underlying dynamic crossover. Since this fining also holds for the remaining BMGs, it is taken as an indication for a generally underlying transition phenomenon in BMGs. However, in the region of the expected transition viscosity measurements are not possible.

High and low temperature fragilities (of table 5.4) are displayed once more. This time in combination with fragilities of the metallic glass Zr-Ni, as shown in figure 5.16.

Data for Zr-Ni is taken from viscosity experiments of Heintzmann et al. [46] and from Busch et al. [21]. Since no viscosity measurements of Zr-Ni in the vicinity of T_g exist, Busch et al. determined the onset temperature of the glass transition at different heating rates and normalized it to the onset temperature of the glass transition measured with a rate of 0.0167 K/min. This data was plotted against the inverse heating rate and fitted with a VFT-type equation. For $Mg_{65}Cu_{25}Y_{10}$ and
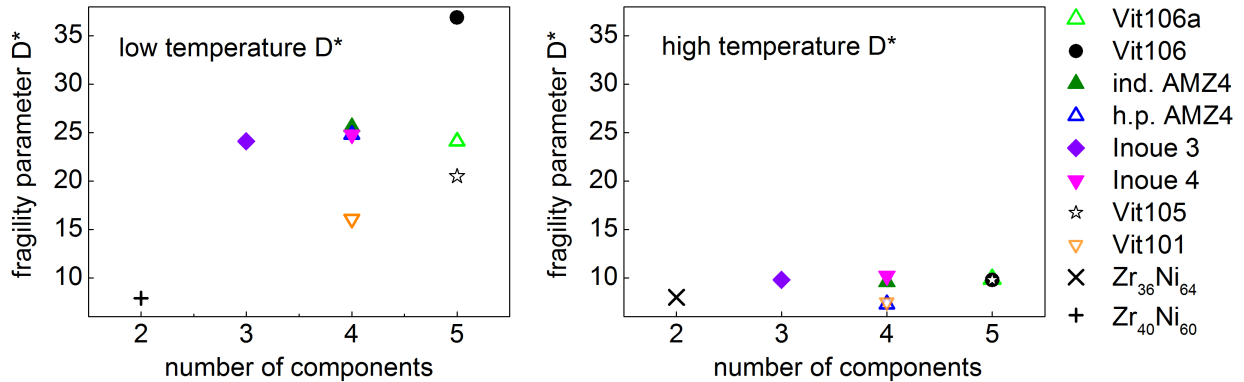
Figure 5.16 – High and low temperature fragilities in dependence of their number of compo-
nents. (Left) Low temperature fragilities are determine from three point beam bending exper-
iments by W. Hembree (see table 5.3), while high temperature fragilities (right) are determined
within this work. $Zr_{40}Ni_{60}$ and $Zr_{36}Ni_{64}$ data was taken from [21] and [45], respectively.

two Be-bearing alloys, the so determined fragility parameters proved to be in excellent agreement
with values obtained from fitting corresponding viscosity data [21]. It is therefore assumed that
the same holds for the Zr-Ni data. In addition, no significant changes in viscosity behaviour are
expected for a $4\,at\,\%$ decrease in Ni content in a $Zr_{36}Ni_{64}$ alloy, as discussed in reference [45].
In figure 5.16 low temperature fragilities cover a region of 8 to 36.9, while high temperature fragili-
ties cover only a region of 8 to 10.2. It is striking that only the low temperature fragilities of
the three and more components BMGs show a strong behaviour (with a fragility of $D^* = 16.1 -
36.9$), while the two component metallic glass Zr-Ni doesn't. In fact, Zr-Ni displays a very similar
fragility at low (7.9) and high temperatures (8).
This suggests that the underlying transition phenomenon is connected to the multiple number
of components in glass-forming alloys. It is however, not connected to the Al-content or the base
system.

In conclusion, high and low temperature fragilities of the investigated BMGs are determined and
reveal a stronger behaviour of the BMGs in the vicinity of T_g than in the liquid state. This in-
dicates a dynamical crossover from a fragile to a strong state (and vice versa). However, this
transition was only found in glass-forming alloys consisting of three or more components, not in
binary glass-forming alloys. Therefore, the underlying transition is possibly linked to the multi-
ple number of components in a BMG. But, since it is found in all investigated BMGs it gives rise
to a generally underlying transition phenomenon in BMGs.

5.8 Specific heat capacity over constant emissivity

Up until here, indications for a strong-to-fragile transition are only found in the high and low temperature fragility of the investigated BMGs. In this section a thermodynamic property, namely the specific heat capacity is considered. It can be derived from the free radiation cooling behaviour of a freely levitating sample, as shown in section 4.2.2.

This is done using the example of Vit106a, because it undercools below T_g without crystallising, as shown in the time-temperature profile in figure 5.17 (left). The corresponding quotient of specific heat capacity and constant epsilon is derived according to section 4.2.2 and the result is shown in figure 5.17 (right).
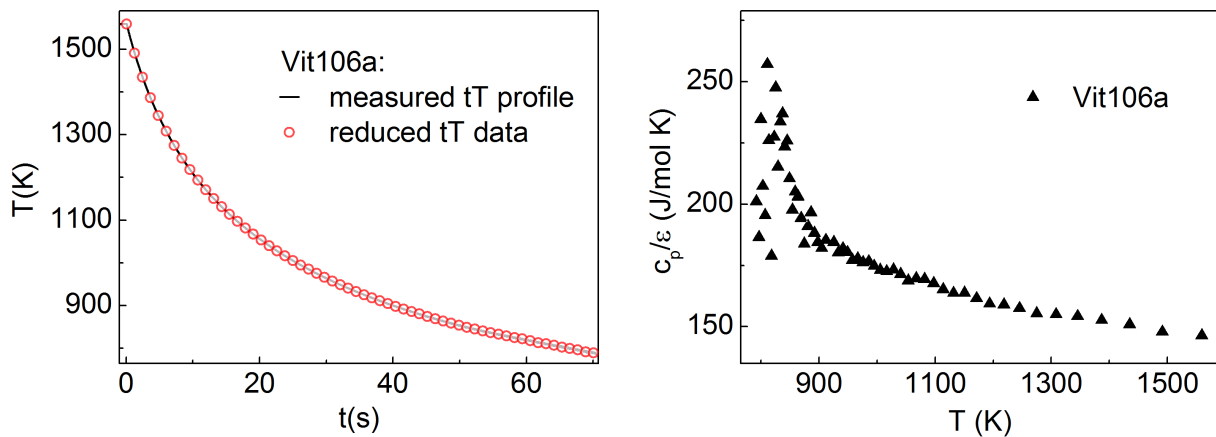
Figure 5.17 – (left) Free radiation cooling curve of a Vit106a sample starting from 1560 K with a reduced amount of data as shown by red circles.
(right) The corresponding c_p/ε curve, determined as explained in section 4.2.2

Between 1560 K and ~ 900 K c_p/ε increases slightly, but consistently. This is expected from equation 5.2. Just below 900 K a pronounced peak in c_p/ε is found, indicating a dissipation of heat. However, no obvious corresponding event is found in the time-temperature profile. Therefore, the origin of this heat release is in the first instance not obvious. Since the peak occurs in the undercooled state, crystallisation or partial crystallisation would be a plausible explanation. Additionally, this peak is an exothermic signal, which supports the crystallisation interpretation.

ESL undercooling experiments of BMGs, which can not be solidified amorphously below T_g, (thus Vit106, Vit105, Vit101, Inoue 3, etc.) show a pronounced recalescence peak in their time-temperature profile, which indicates the event of complete crystallisation. Therefore, in the case of Vit106a, as presented in figure 5.17 a complete crystallisation process can be ruled out, but small fractions of (nano-) crystalline phases are possible. Evidence about such possible crys-

tallisation process provide ESL experiments in combination with x-rays. Such experiments are performed within this work. They are presented and discussed in section 5.10 ff.

A similar behaviour of c_p/ε is found for the case of Inoue 4 (not shown). There too, a pronounced peak in c_p/ε occurs without distinct sign in the corresponding cooling curve. The onset of the Inoue 4 peak is found at around 865 K. Inoue 4, besides Vit106a, is the only other investigated BMG which can be vitrified below T_g in ESL free radiation cooling experiments. This is not possible for the remaining BMGs. There, ESL cooling rates are too slow and crystallisation sets in before a possible transition takes place.

In summary, Vit106a and Inoue 4 which can be solidified amorphously below T_g without crystallisation provide an exothermic signal in their undercooled state. Since the origin of this signal is unclear from the c_p/ε results alone, it will be investigated in section (5.10 ff.)

5.9   Specific volume and thermal expansion coefficient

Volume as a function of temperature provides information on phase transitions. A discontinuous volume course indicates a first order phase transition, while a continuous volume course implies a second order transition, as discussed in section 2.3. Therefore, volume seems a suitable parameter to characterise possible phase transitions, such as the LLT is assumed to be one. In this section, specific volume which can be derived from the density according to section 4.2.4 is compared to measurements of Li et al. [91] and analysed whether it provides any distinct features in its volume course over temperature.

Li et al. [91] reported on a hysteretic behaviour of specific volume as function of temperature for the BMG Vit106, as shown in figure 5.18. They argue that it is a first order phase transition from a low density to a high density liquid [91], which is not caused by crystallisation. This finding is reviewed in the following. For this, and in the scope of this work a comparative measurement on Vit106 is performed in order to determine the specific volume in dependency of temperature, as shown in figure 5.19 (left).

Both measurements are conducted upon free radiation cooling from around 1500 K down to approximately 850 K and upon subsequent reheating back to the starting temperature. Results, however are partly in contrast to each other.

The measurement of Li et al., as displayed in figure 5.18 shows a change in slope upon cooling at around 1000 K and possibly again around 900 K. Upon reheating, the specific volume coincides for about 100 K with the volume upon cooling, before a deviation is observed. Here, the volume upon heating stays constant with increasing temperature (until ~ 1125 K), followed by a sudden volume increase and a slower increase until both volumes match each other again at the starting temperature of 1500 K,
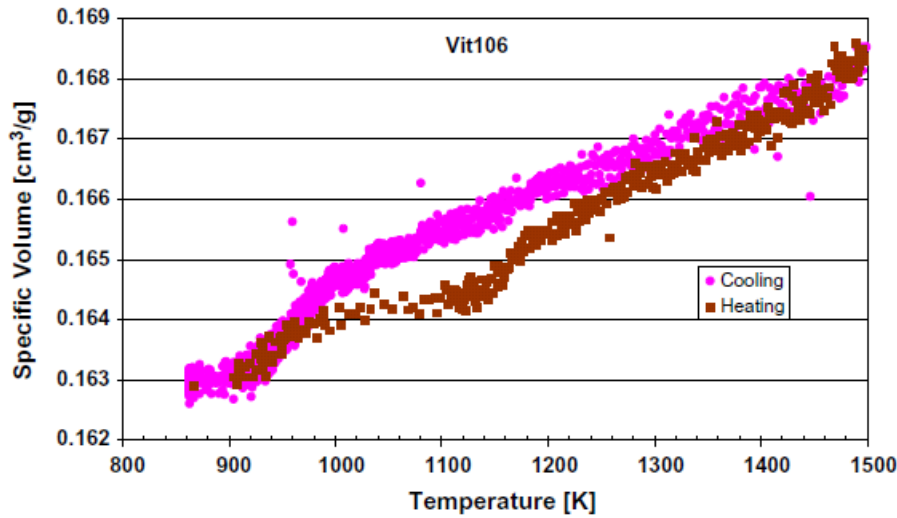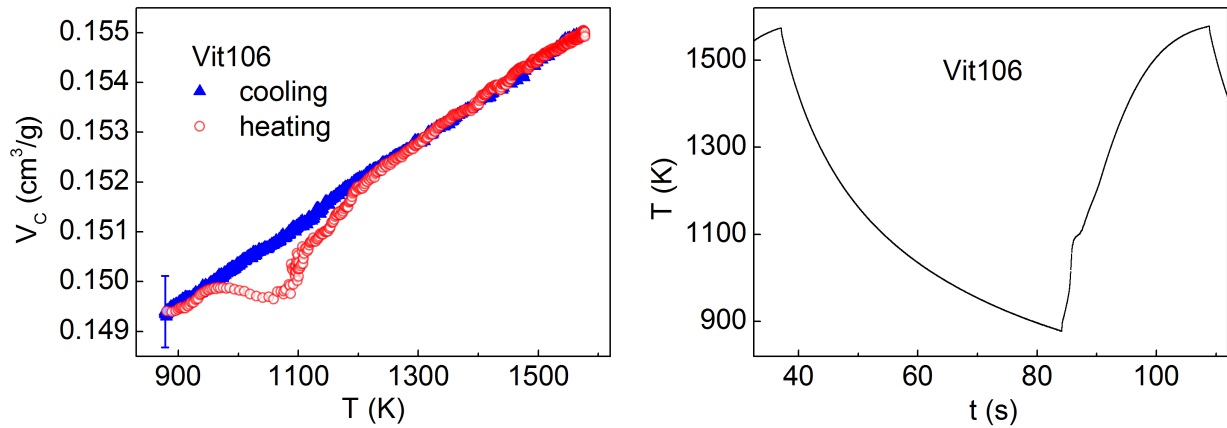
Figure 5.18 – Specific volume as function of temperature of Vit106 upon a complete cooling and reheating cycle. The data is taken from Li et al. [91].

Li et al. claimed that the change in slope of the volume-temperature relationship upon cooling arises not from crystallisation, but from a first order phase transition, because no signal, such as a recalescence, is seen in the corresponding time-temperature profile [91].

The measurement conducted within this thesis is presented in figure 5.19 and shows a continuous linear decrease in volume upon free radiation cooling all the way down to ~ 880 K. Upon reheating, the specific volume also coincides for about 100 K with the volume upon cooling, before a deviation is observed. Here, the volume upon heating stays constant with increasing temperature (until ~ 1075 K), followed by a sudden volume increase and a slower increase until both volumes match each other again at 1200 K.

When taking a look at the corresponding time-temperature profile in figure 5.19 (right) indeed, no indications for crystallisation or a recalescence are visible upon cooling from 1575 down to 880 K. However, upon reheating a peak is clearly observed, where the temperature suddenly and drastically increase. This temperature peak starts at around 960 K and finishes at ~ 1100 K and exceeds the slope of the initial heating rate upon reheating (880 - 960 K). The starting temperature of the peak matches the starting temperature of the deviation in volume upon heating from the volume upon cooling. The last part of the peak, which can also be considered as a melting plateau finishes at around 1100 K. This temperature is in agreement with the liquidus temperature of Vit106 (for $T_{liq,Vit106}$ see table 4.1). Thus, this temperature peak upon reheating is interpreted as crystallisation, which is directly followed by the melting process. This hypothesis is also supported by measurements of Bendert et al. [15].

The volume increase associated with crystallisation in clearly visible in the specific volume course of the experiment performed in this section (figure 5.19 (right)) as well as in the experiment of

Figure 5.19 – (left) Specific volume as function of temperature of Vit106. The measurement is performed within this thesis. (right) The corresponding time-temperature profile upon cooling and reheating back to the measurement starting temperature.

Li et al. [91]. Unambiguous information whether or not this volume increase is due to crystallisation provide for instance ESL experiments in combination with x-rays, as performed in the following sections.

Hitherto, it is assumed that an amorphous BMG of the deeply undercooled state undergoes a crystallisation process upon heating before melting takes place and the glass enters the liquid state.

Additional experiments, which are not displayed in this work showed that undercooling and subsequent reheating experiments (back into the liquid state) without visible crystallisation in the time-temperature profile or a melting process taking place, are only possible for small undercoolings up to a maximum of $\Delta 75 \, K$.

The finding of Li et al. [91] of a change in the linear specific volume-temperature behaviour upon free radiation cooling could not be confirmed by a comparative experiment on Vit106.

Along with this finding, comes the fact that the two measurements differ not only in their volume-temperature relation upon cooling, but also in their absolute specific volume values. The measurement, which is conducted within this work displays a lower specific volume than the measurement of Li et al. [91]. In addition, both measurements show a different slope upon cooling from around $1500 \, K$ down to $\sim 1000 \, K$. This is reflected in their thermal expansion coefficients, which are 5.5×10^{-5} ($\pm 0.2 \, \%$) K^{-1} for the measurement of Li et al. [91] [2] and $5.67 \times 10^{-5} \, K^{-1}$ ($\pm 0.2 \, \%$) for the measurement performed within this work. (For information on the thermal expansion coefficient see section 4.2.5.) This suggests an issue in the calibration process, either

---

[2]The error given by Li et al. [91] is normalised to the liquidus temperature. For comparison, the same was done for the error determined for the expansion coefficient within this work.
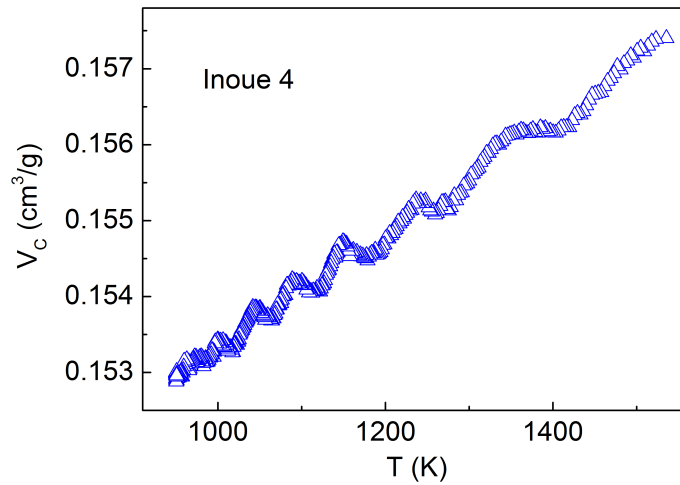
Figure 5.20 – Specific volume as function of temperature of Inoue 4 upon cooling. The measurement is performed on an unstable levitation process and with a reduced object distance of g < 300 mm. The resulting volume fluctuations have no physical meaning, but are due to circular movements of the sample.

upon converting pixel to real volume or due to a position uncertainty.

Within this work, special attention has been paid to minimise errors arising from the calibration process as extensively discussed in section 4.2.3. Position detection uncertainties can arise from an unstable levitation. If a levitating sample moves considerably towards and away from the camera, the relation between analysed pixel volume and real volume constantly changes. This becomes apparent as volume (or density) fluctuations in the results. The effect can be intensified by an inappropriate experimental setup (see discussion in section 4.2.3). Hence, volume (and density) measurements require a very stable levitation.

An example of a volume measurement conducted from an unstable levitation and determined with reduced object distance (g < 300 mm) is shown in figure 5.20. Here, significant fluctuations in volume are visible, which have no physical meaning, but are due to circling movements of the sample during the measurement. Therefore, levitation stability, calibration and experimental setup of the experiment performed by Li et al. [91] are worth reviewing.

Furthermore, the specific volume of the remaining investigated BMGs was determined (not displayed). All BMGs show a continuously linearly decreasing volume upon free radiation cooling until just prior to the onset of crystallisation or in the case of Vit106a until below T_g. This means, non of the investigated BMGs shows a change in slope upon cooling as found in ESL experiments by Li et al. [91]. The corresponding thermal expansion coefficients of the investigated BMGs were determined and are given in table 5.5 as well as the temperature ranges from which the coefficients were determined and the absolute error.

	temperature range (K)	a (K^{-1})
Vit106a	640 – 1515	5.62 x 10^{-5} ($\pm$ 0.0044)
Vit106	875 – 1575	5.67 x 10^{-5} ($\pm$ 0.0047)
Vit105	880 – 1535	5.26 x 10^{-5} ($\pm$ 0.011)
Vit101	945 – 1560	7.16 x 10^{-5} ($\pm$ 0.005)
Inoue 4	700 – 1700	4.64 x 10^{-5} ($\pm$ 0.011)
Inoue 3	930 – 1520	5.55 x 10^{-5} ($\pm$ 0.0074)
AMZ4 (ind.)	1080 – 1500	5.04 x 10^{-5} ($\pm$ 0.011)
AMZ4 (h.p.)	860 – 1575	5.2 x 10^{-5} ($\pm$ 0.0091)

Table 5.5 – Thermal expansion coefficients of the investigated BMGs and the respective temperature range from which the coefficients are determined.

In conclusion, the specific volume of the investigated BMGs revealed a continuous linear decrease in volume upon free radiation cooling until just prior to the onset of crystallisation or until below T_g and thus, provides no indication for an underlying transition. This is in contrast to the finding of Li et al. [91]. Moreover, the thermal expansion coefficients were determined as given in table 5.5.

5.10 In situ structural investigations using x-rays

Up until here, indications for an underlying transition are found in the high and low temperature fragility of the investigated BMGs (see section 5.7). The peak in the c_p/ε course (section 5.8) could also be associated with the strong-to-fragile transition. However, it must be verified first that crystallisation as origin of the peak can be excluded. These indications suggest that an underlying transition presumably takes place in the undercooled state.

Therefore, further investigations focus only on the BMG Vit106a. This is done, because Vit106a can be reliably cooled into the glassy state in ESL experiments independent of its sample mass and therefore, possibly transitions are not masked by crystallisation.

In this section, ESL experiments are combined with in situ structural investigations using high energy x-rays. This is done, in order to investigate the origin of the specific heat capacity signal as well as to exclude crystallisation processes.

For this purpose, the mobile ESL (see section 3.3.2) was brought to the German Electron Synchrotron (DESY) and operated in the high intensity source for synchrotron radiation, PETRA III (for more information on this technique see section 4.6). This setup enables time-resolved in situ structural information on levitation experiments.

Free radiation cooling experiments on Vit106a were performed upon cooling from the equilibrium melt through the undercooled regime into the glassy state, but with simultaneous time-

resolved structural information. These cooling experiments are performed in analogy to those of section 5.8.

Several heating and free radiation cooling cycles were performed on a single sample. Figure 5.21 shows two cooling curves of such experiments (in the following referred to as cooling experiments a) and b)), where the sample was heated to 1500 K and kept at this temperature for approximately 30 s. Subsequently, the heating laser was switched off and the sample was left to free radiation cooling.
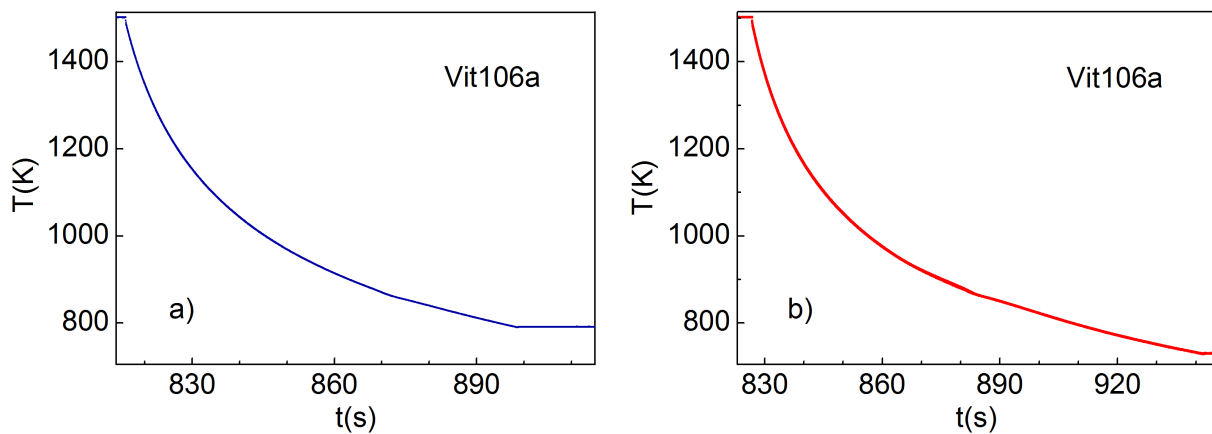
Figure 5.21 – Time-temperature profiles of free radiation cooling experiments on Vit106a. (left) Cooling cycle a) of Vit106a from 1500 to 790 K. (right) Cooling cycle b) of Vit106a from 1500 to 730 K, determined from the identical Vit106a sample as cooling cycle a).

The two time-temperature profiles of figure 5.21 show no significant difference in their cooling behaviour. Both curves show a time dependent temperature decay with a temperature dependence of $t^{\frac{1}{3}}$ (as expected from eq. 4.2) and no indications of a recalescence.

Cooling curve a) (figure 5.21 (left)) reaches its final temperatures at 790 K, while cooling curve b) reaches it at 730 K (figure 5.21 (right)). The temperature of 790 K is maintained by the heating laser while 730 K is the lowest detection limit of the pyrometer and hence, not the actual sample temperature. The two time-temperature profiles of figure 5.21, which are both derived of the same sample lead to the conclusion that the sample solidified amorphously in both cases.

The c_p/ε signals corresponding to the two cooling experiments (a) and b)) are derived from the time-temperature profiles of figure 5.21. The resulting c_p/ε signals are shown in figure 5.22.

The c_p/ε signals increase marginally, but consistently upon cooling from 1500 K once until ~ 880 K (cooling experiment a)) and once until ~ 950 K (cooling experiment b)). There, in each case a peak in c_p/ε is found. However, differently pronounced.

In case of cooling experiment a), a single peak in c_p/ε is found at a onset temperature of ~ 880 K. In the case of cooling experiment b), an additional (pre-)peak is found with a onset temperature
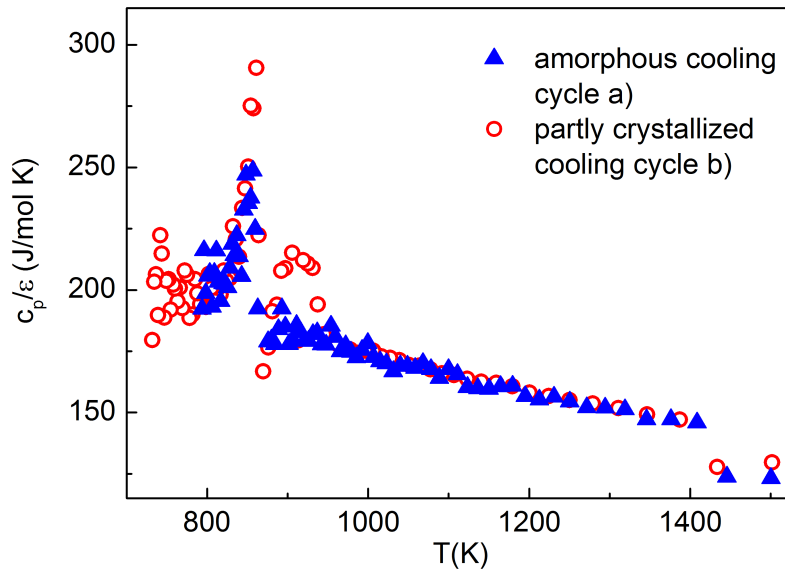
Figure 5.22 – Two c_p/ε signals derived from the free radiation cooling experiments already presented in figure 5.21. Blue triangles belong to the evidently amorphous cooling cycle of 5.21 and 5.23 a), while red circles belong to the partially crystallised cooling cycle of 5.21 and 5.23 b).

of ~ 950 K. This peak is more pronounced than the peak of the cooling experiment a). It covers the same area of peak a) as well as additional area. In order to identify the influence of crystallisation on the two cooling experiments and their c_p/ε signals the corresponding structural information of the two cooling experiments are analysed and displayed in figure 5.23.

Here, the intensities in dependence of the resolved distance q are displayed, providing direct information on if and when crystallization sets in. For clarity, intensities are only displayed in the undercooled temperature regime in 50 K steps starting from 1000 K down to the respective final temperature. Curves are also shifted for clarity.

Figure 5.23 (left) contains the structural information belonging to the time-temperature profile of the cooling experiments a) as displayed in figure 5.21 (left). It shows the smooth patterns of an amorphous structure lacking a long-range order. During undercooling below T_{liq} the first and second peak increase in intensity. Further intensity peaks are not sufficiently pronounced. None of the patterns reveal any Bragg peaks or indications for such. Leading to the conclusion that the sample of cooling experiment a) is completely vitrified as already indicated by the time-temperature profile.

Figure 5.23 (right) contains the structural information belonging to the time-temperature profile of cooling experiment b) as shown in figure 5.21 (right). Above 950 K it presents smooth patterns of an amorphous structure. At around 900 K small Bragg peaks start to form on the second peak.
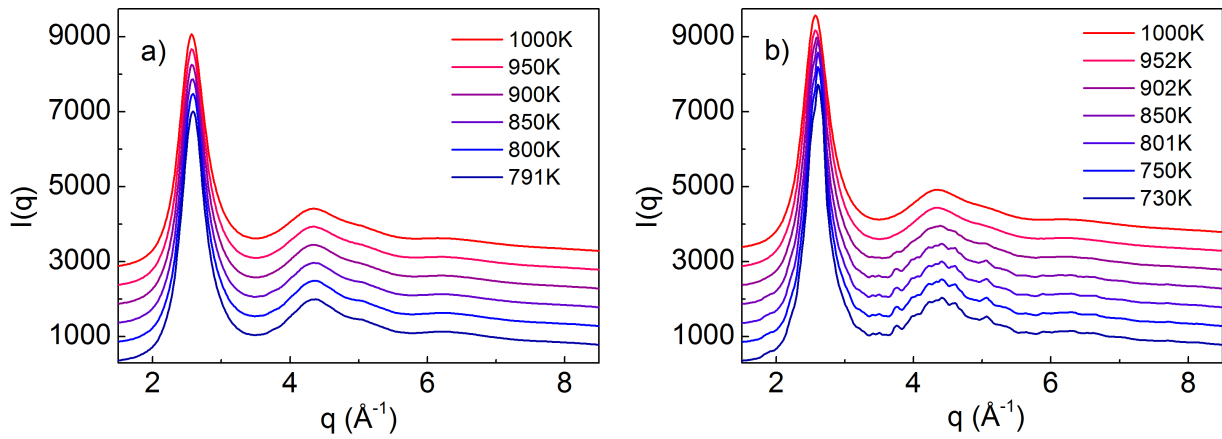
Figure 5.23 – In situ structural information on Vit106a upon free radiation cooling experiments. The corresponding time-temperature profiles are displayed in fig. 5.21. Curves are shifted for clarity.

(left) Intensity distribution of Vit106a upon cooling from 1500 down to 790 K. The corresponding time-temperature profile is shown in figure 5.21 (left).

(right) Intensity distribution of the identical Vit106a sample, which cooled from 1500 to 730 K. The corresponding time-temperature profile is displayed in figure 5.21 (right).

They become more pronounced towards lower temperatures. Also the maximum of the first peak starts sharpening around 900 K and increases in intensity. This, becomes more pronounced towards lower temperatures. The formation of Bragg peaks as well as the sharpening and increase of peaks indicate the formation of crystals. But since the characteristics of the Bragg peaks are fairly small, probably only small fractions of the sample crystallised.

The corresponding time-temperature profile (see figure 5.21 (right)) however, shows no indications for crystallisation. This information is in contrast to the result of the structural x-ray investigations and leads to the conclusion that x-ray investigations are much more sensitive to crystallisation or partial crystallisation than the time-temperature profile.

Note, that until 790 K the two cooling experiments do not differ from each other. They follow exactly the same process. The difference, thus the partial crystallisation, sets in long before this temperature (of 790 K) is reached.

Therefore, these two cooling experiments reveal that time-temperature profiles alone are not sufficient to detect partial crystallisation. Only in situ x-ray (or similar) investigations are precise enough to provide such information.

For the c_p/ε signals shown in figure 5.22 this means that the c_p/ε peak of cooling experiment a), where the sample solidified amorphously as demonstrated in figure 5.22 (left) does not arise from crystallisation. While the c_p/ε peak of cooling experiment b) is at least partly due to the formation of small crystalline fractions. Hence, the c_p/ε signal found in the undercooled state

of Vit106a (see section 5.8) does not arise from crystallisation. It is therefore associated with a strong-to-fragile transition. However, small fractions of crystallisation easily contribute the c_p/ε peak. This manifests in an increased c_p/ε onset temperature and a more pronounced c_p/ε peak.

In conclusion, undercooling experiments with identical process parameters do not necessarily take the same course. It is not evident from a time-temperature profile whether a sample solidifies amorphously or whether small crystalline fractions formed. Therefore, an in situ process control is indispensable.

This in situ control, in turn revealed that the c_p/ε peak found in the undercooled state of Vit106a does not arise from crystallisation. The c_p/ε signal is therefore, associated with an underlying transition. However, small fractions of crystallisation can contribute to the c_p/ε peak. This is reflected in an increased c_p/ε onset temperature, a more pronounced c_p/ε peak, and structural information.

5.11   Enthalpy determination of the thermal signal

In this section, the enthalpy corresponding to a c_p/ε peak of the undercooled state of Vit106a is determined. For this, specific heat capacities measured by Gallino et al. [40] using an optimised differential scanning calorimetry method are employed.
This study on the c_p/ε peak is than further extended and covers this and the next section.

First, a free radiation cooling experiment on Vit106a was performed. Note, that this experiment was performed without an in situ process control, thus small fractions of crystallisation can not be excluded. However, the (according to the time-temperature profile) vitrified sample was preserved and further investigated in terms of the crystallisation issue in section 5.12.
Next, the c_p/ε course was determined according to section 4.2.2 and as shown in figure 5.24 together with data of Gallino et al.[40]. The ESL c_p/ε data increases slightly upon cooling between 1300 K and ~ 925 K. Followed by a c_p/ε peak with an onset temperature of 925 K. This onset temperature is in between the c_p/ε onset temperatures determined from in situ controlled experiments (section 5.10), which showed that an c_p/ε onset temperature of ~ 880 K was free of crystallisation, while an c_p/ε onset temperature of ~ 950 K wasn't. Thus, small fractions of crystallisation are possible for the experiment performed and analysed within this section.

The emissivity was determined using the data of Gallino [40] and eliminated from the ESL c_p/ε measurement results. For this, the linear region of the ESL c_p/ε course, thus the temperature region between 960 K and 1330 K was fitted with the same Kubaschewski fit as used by Gallino et al.[40] for the undercooled liquid. This Kubaschewski fit is given by

$$c_p^{liq}(T) = 3\,R \,+\, a\,T \,+\, b\,T^{-2}\,.\tag{5.2}$$

Here R is the universal gas constant, T the temperature, and a and b are fitting constants of

a = 0.00565 and b = 5.697 x 10^6 according to Gallino et al. [40]. The hereby obtained c_p^{liq} was divided by the experimentally determined c_p/ε data. The resulting emissivity was averaged and multiplied with the ESL c_p/ε data.
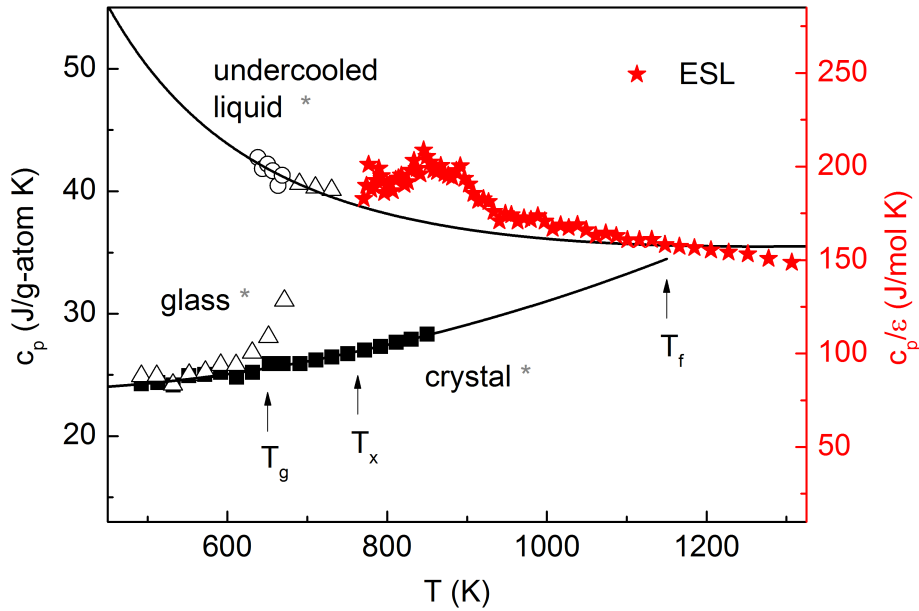
Figure 5.24 – Specific heat capacities for Vit106a as function of temperature. Data marked by * is taken from Gallino et al. [40]. Triangles represent data of the equilibrium liquid as well as of the glass. Squares represent the crystalline solid and circles the undercooled melt. Red stars represent the measurement conducted within this work by ESL technique.

The enthalpy of the ESL c_p/ε peak, ΔH_{ESL} is determined by integrating the area under the peak. It corresponds to ΔH_{ESL} = ~ 0.5 kJ/g-atom K. According to Gallino et al. [40] the enthalpy of crystallisation for Vit106a corresponds to ΔH_x= 6.38 kJ/g-atom K (for 0.333 K/s). Hence, the enthalpy of the ESL c_p/ε peak corresponds to ~ 8 % of the enthalpy of crystallisation.

Since crystallisation is the biggest issue upon investigations of the undercooled melt, it is rechecked in the following section whether partial crystallisation contributes to the signal in heat capacity and if so, to what extent.

5.12   Scanning electron microscopy

Structural investigations demonstrated that the c_p/ε peak in the undercooled state of Vit106a is not caused by crystallisation (see section 5.10). However, partial crystallisation can contribute to this peak. In the previous section the enthalpy corresponding to a c_p/ε peak was estimated. However, no structural information corresponding to this peak (of section 5.11) exist. Therefore,

it is investigated in this section whether and if so, to what extend crystallisation influenced the heat capacity peak. This is done using optical microscopy and scanning electron microscopy (SEM).

For this, the sample was fixed in embedding material (PolyFast) and sanded off to the half. The remaining volume cross section of the sample was first investigated by optical microscopy with polarised light. Figure 5.25 presents an image obtained by this technique. The bottom right part of the figure shows the embedding material in different shades of green, while the top left part of the figure shows about a quarter of the spherical cross section of the sample volume in pink. Colours are caused by polarization filters and do not represent real colours.
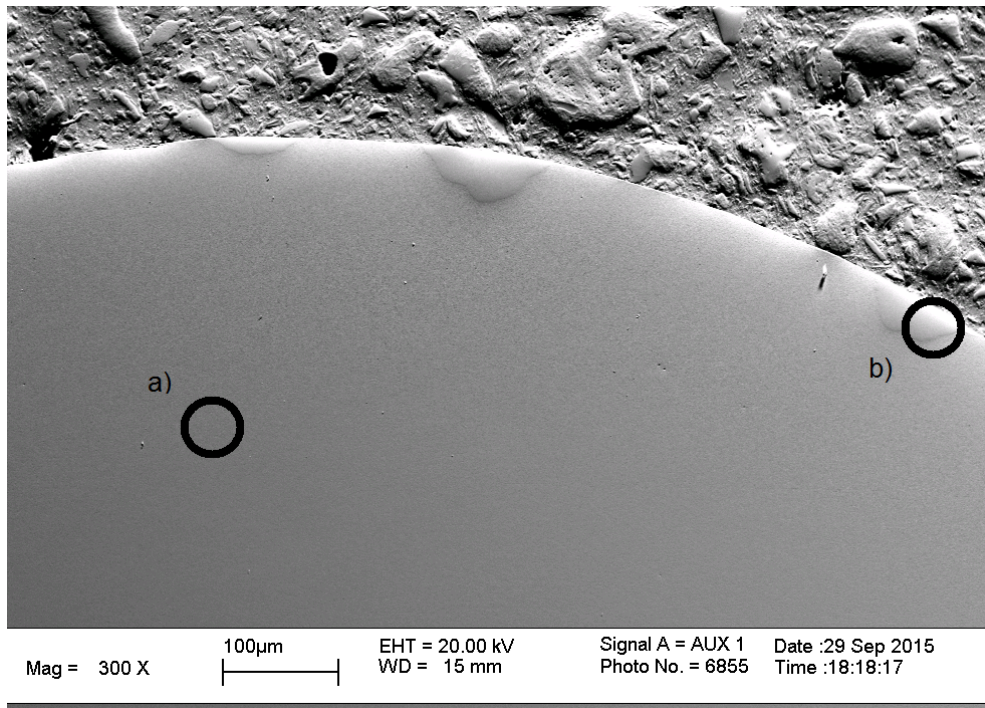
The bulk of the volume cross section of the sample shows an optically homogeneous phase (represented in pink). The grey shadows dominating this phase are caused by the lens. The sample edge towards the embedding material shows little patterns of colours different from the bulk, these patterns are rather orange and purple. They indicate different phases from the bulk. These patterns are located irregularly along the edge, but don't cover the entire edge. Their structure is further investigated using scanning electron microscopy.

For this, the as prepare sample was investigated by SEM, for a start with a forward scattering detector (AUX 1). Figure 5.26 shows the obtained image.

Again, an image section of the same sample volume cross section, as already displayed in figure 5.25 is shown. This time the embedding material is found at the top of the image, while the re-
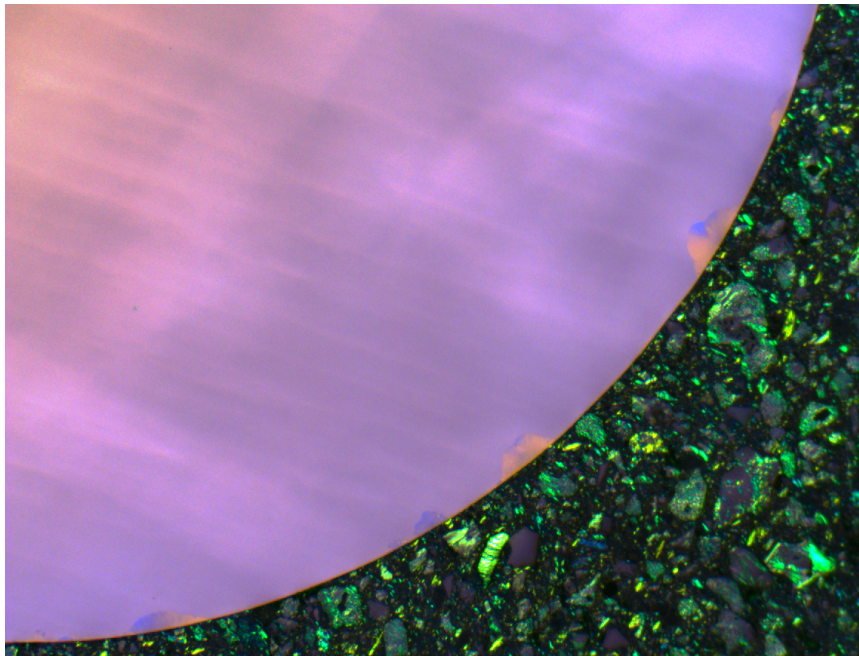
Figure 5.25 – Optical microscope image of a volume cross section of a spherical Vit106a sample. This sample was vitrified in the ESL free radiation undercooling experiment of section 5.11.

Figure 5.26 – Scanning electron microscope image of the same volume cross section of Vit106a, as already investigated in figure 5.25. The corresponding c_p/ε course is displayed in figure 5.24. The areas a) and b), as marked by the black circle represents bulk parts as well as edge patterns, respectively.

maining part of the image shows a section of the sample's volume cross section. The bulk of the sample displays a homogeneous phase, whereas irregular patterns are found along the sample edge, just like in figure 5.25.

The forward scattering detector used to create this image generates the image due to electron-electron interactions. Here, the primary electrons are deflected by a typically small angle. Bright regions represent regions facing the detector, since here an increased number of scattered electrons reaches the detector compared to regions facing away from the detector.

For this image, as well as for later electron backscattering diffraction (EBSD) investigations, the sample is tilted 70° from the horizontal. Due to this tilt elevations become more pronounced, even though the sample surface is principally flat. This becomes particularly clear in the embedding material.

EBSD investigations were carried out in the bulk and the patterns along the edge. These areas are indicated in fig. 5.26 by black circles marked with a) and b). EBSD is a crystallographic characterisation technique to study the structure of a material. Here, the primary electron beam is inelastically scattered on atoms of the material forming a divergent source. If electrons impinge on a crystallographic plane and fulfil the Bragg condition constructive interference occurs. The resulting diffraction images show diffraction patterns of strip slightly brighter than the back-

ground, which are also called Kikuchi bands or lines.

EBSD investigations of the bulk were performed, but revealed no diffraction patterns at all, as shown in figure 5.27 a). This confirms the absence of crystallographic structures and verifies that the bulk exhibits an amorphous structure.

Investigations of the patterns along the sample edge revealed diffraction patterns (Kikuchi lines), as shown in figure 5.27 b).
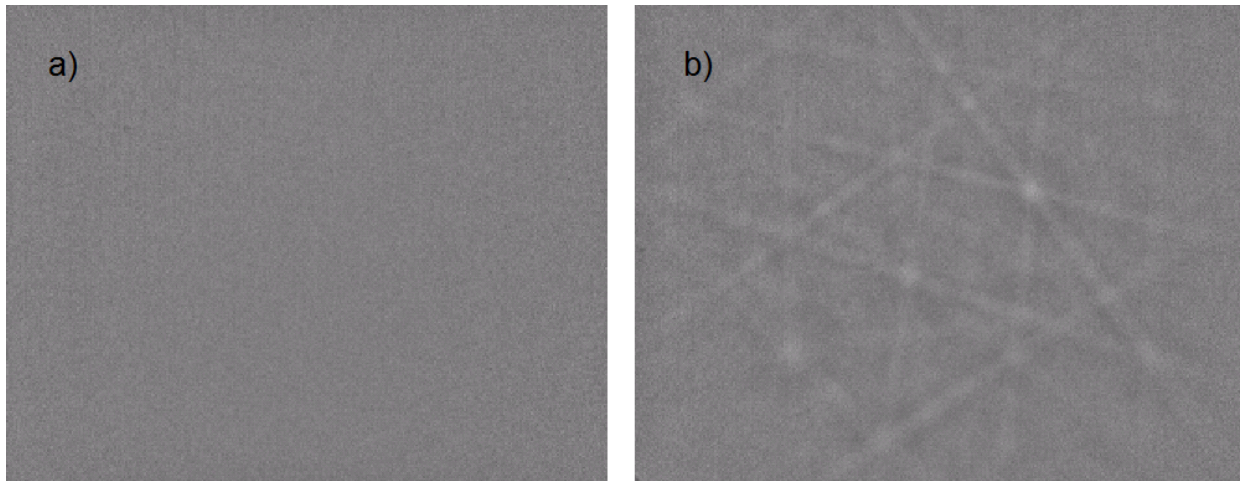
Figure 5.27 – Electron backscattering diffraction (EBSD) images of a) the bulk showing no diffraction patterns and b) edge patterns showing diffraction patterns (Kikuchi patterns).

This proves the existence of small fractions of crystalline phases along the sample edge. Note, that these crystalline fraction do not cover the entire sample surface (see figure 5.26). SEM images of the complete volume cross section (which are not displayed within this thesis) showed that the crystalline patterns do not cover the entire sample surface. They are located irregularly on the surface and only form a small part of the surface. This, in turn means that the emissivity is barely influenced and ε approx constant holds.

However, no statement can be made about the temperature at which these crystalline fractions formed, since corresponding in situ studies on this sample do not exist. Yet, it is assumed that these crystalline parts formed at around 925 K, thus at the onset temperature of the corresponding c_p/ε peak (see section 5.11). This means that small fractions of crystals contributed to the c_p/ε peak and thus also to the enthalpy (ΔH_{ESL}) determined for the this peak in section 5.11.

In the following, it is estimated to what extent the crystalline fractions contribute to the enthalpy of the c_p/ε peak, (ΔH_{ESL}) determined in section 5.11.

For this, the SEM image of figure 5.26 is reused in order to estimate the amount of surface crystallisation, as demonstrated in figure 5.28.

The area or rather the volume between surface edge and black lines in figure 5.28 represents the crystalline fractions. It is estimated to be half the volume of the sample's outer shell. This shell is
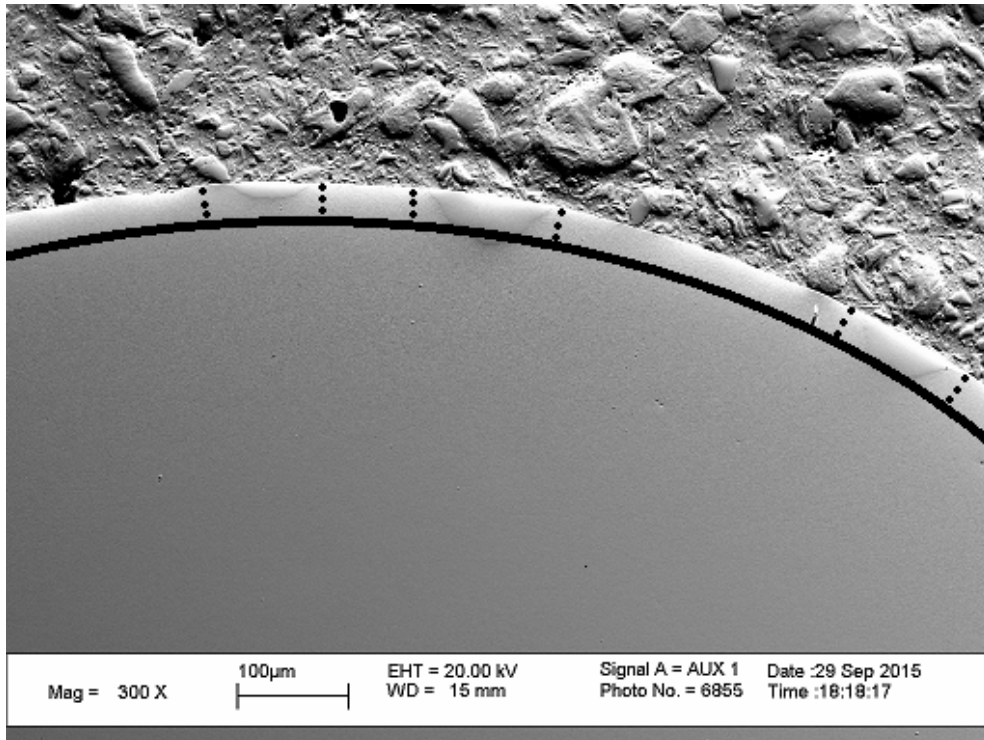
Figure 5.28 – Scanning electron microscope image of the Vit106a volume cross section already investigated in figure 5.25 and 5.26. The corresponding c_p/ε course is displayed in figure 5.24. The area or rather volume enclosed between sample edge and black line represents the estimated amount of surface crystallisation.

defined by the surface and the black solid line as shown in figure 5.28 These dimensions estimate the shell to be 1.5 % of the sample's diameter. This, in turn corresponds to 4 % of the sample volume. Thus, half of this volume, namely 2 % of the sample volume is estimated to be crystallised. This is a generous assumption, because it considers a slightly greater amount of crystalline fractions than indicated by the individual crystalline edge parts. According to Gallino et al. [40] the enthalpy of crystallisation for Vit106a is $\Delta H_x = 6.38$ KJ/g-atom K, thus 2 % crystallisation would correspond to an crystallisation enthalpy of 0.128 KJ/g-atom K.

However, the enthalpy corresponding to the heat capacity signal of this sample was determined to be ~ 0.5 KJ/g-atom K in section 5.11. This, is nearly four times the amount of enthalpy than estimated for the small crystalline fractions.

This shows that the c_p/ε signal in the undercooled melt of Vit106a arises not solely due to crystalline fractions. However, small crystalline fractions can contribute to the c_p/ε signal.

In conclusion, SEM investigations in combination with EBSD showed that a vitrified Vit106a sample can form small crystalline fractions on its surface. An enthalpy estimation demonstrated that these crystalline fractions are not sufficient to cause the c_p/ε peak in the undercooled state, however they can contribute to it.

5.13 Structural changes in the undercooled melt of Vit106a

Up to now, it was shown that the c_p/ε signal found in the undercooled state of Vit106a does not arise from crystallisation or at least not from crystallisation alone (see section 5.10 and 5.12). Yet, the origin of this signal is unknown. In order to investigated a possible origin studies of the atomic structure are performed.

For this, in situ structural investigations of ESL experiments in combination with x-rays are performed at the PETRA III P07 beamline (DESY). (For information on this method see section 4.6.) In this section, an initially amorphous Vit106a sample was heated with 100 K/min to ~ 1500 K, kept there for 30 s and afterwards left to free radiation cooling back into the glassy state (for the corresponding time-temperature profile see figure 5.31 (left)). The position of the first maximum of the total structure factor (S(q)), q_{max} was determined for this experiment upon heating and cooling. Furthermore, the in situ structural monitoring was used to detect crystallisation.
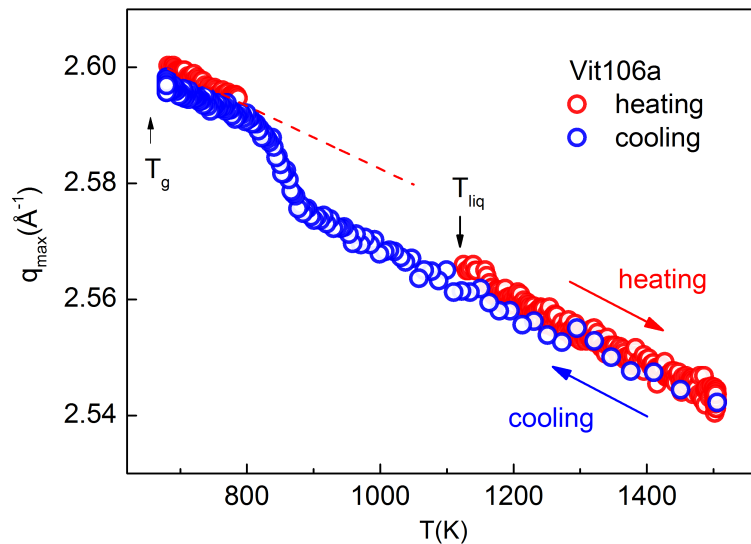

Figure 5.29 – Position of the first maximum of the total structure fractor (S(q)), q_{max} during heating of an initially amorphous Vit106a sample and upon free radiation cooling back into the glassy state.

First, the position of the first maximum in S(q), q_{max} was analysed and is presented in figure 5.29. During heating q_{max} decreases with increasing temperatures between 680 K and 780 K and between 1120 K and 1505 K. In between these two temperature regions the amorphous sample crystallises and melts. For reasons of clarity this data is not shown in figure 5.29. A linear extrapolation, however shows that the q_{max} data of the undercooled liquid does not match the q_{max} data of the liquid state (during heating). Upon cooling q_{max} increases with decreasing temperatures from approximately 1500 K to 880 K. It matches the data during heating until a sudden

increase in q_{max} is found between ~880 K and ~800 K. After this increase the q_{max} data upon cooling matches the data during heating again. Since q_{max} reflects an inverse spacing, an increase in q_{max} reflects a decrease in interatomic distance whereas a decrease in q_{max} reflects an increase in interatomic distance.

In order to ensure that the shift in q_{max} upon cooling between ~880 K and ~800 K does not arise from crystallisation, the corresponding structural information are considered. For this, the evolution of the intensities in dependence of the resolved distance q upon cooling are shown in figure 5.30.
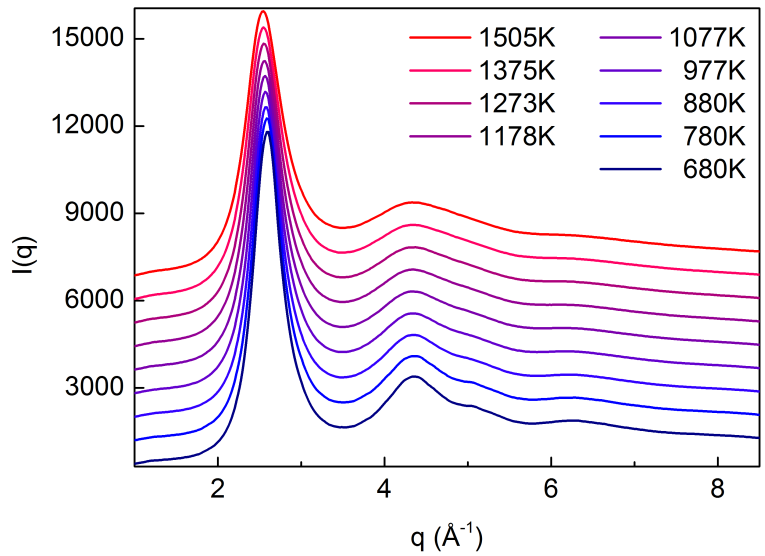
Figure 5.30 – Evolution of intensities in dependence of the resolved distance q upon cooling. The intensity information belong to the q_{max} data of figure 5.29. Curves are shifted for clarity.

The intensity distributions show smooth patterns and lack a long-range order, indicating an amorphous structure. Upon undercooling the first and second peak increase slightly in intensity. None of the distributions reveal any Bragg peaks or indications for such. (Indications in the intensity distribution for the formation of crystalline fractions upon undercooling are shown in figure 5.23 (right).) This leads to the conclusion that no crystallisation occurred and the sample entirely vitrified. This, in turn confirms that the observed shift in q_{max} just below 880 K is not caused by crystallisation, but is due to structural changes in the undercooled liquid state.

Next, the c_p/ε course was derived from the time-temperature profile of the experiment performed within this section. Time-temperature profile as well as c_p/ε course are shown in figure 5.31. The time-temperature profile shows a linear heating rate of 100 K/min from 680 K to 1505 K. Recalescence and melting are reflected in a peak between 810 K and 840 K. Cooling happened due to free radiation cooling. Note that the lowest detection limit of the pyrometer is 673 K. The c_p/ε course was derived from the cooling behaviour according to section 4.2.2. The c_p/ε signal

increases slightly between 1400 K and ~ 900 K. (The c_p/ε value at 1500 K is due to data reduction.) Just below 900 K a peak in c_p/ε is found. The onset temperature of this peak is ~ 880 K and correlates with the onset temperature of the sudden increase in q_{max} upon cooling (see figure 5.29), which is also found at ~ 880 K.

Therefore, the thermal signal found in the undercooled melt is associated with structural changes observed in the diffraction pattern.

In conclusion, structural changes, which are not caused by crystallisation were found in the undercooled melt of Vit106a. These structural changes were correlated with the thermal signal found in the corresponding c_p/ε course. Since, structural changes and thermal signal occur at
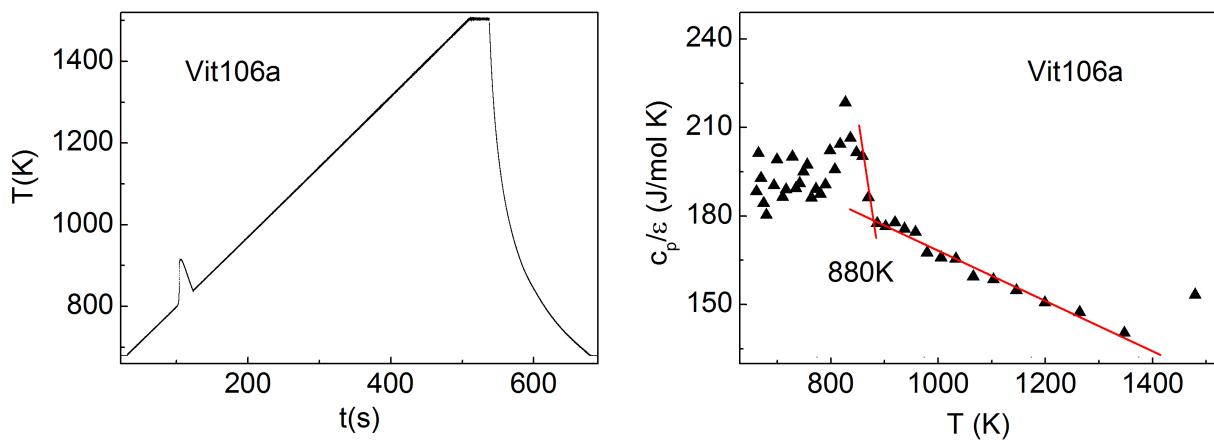
Figure 5.31 – (left) Time-temperature profile of an ESL experiment with a 100 K/min heating rate and free radiation cooling. (right) c_p/ε course derived from the free cooling data of the time-temperature profile (left).

the same onset temperature they are associated with each other. It is assumed that they correspond to the same underlying process, which demonstrably is no crystallisation, but possibly an strong-to-fragile transition.

5.14   Cooling rate dependence of structural changes

In this section, ESL cooling experiments in combination with in situ investigations are performed at different cooling rates. This is done in order to investigate a possible dependence between structural changes and the cooling rate.

Cooling experiments on Vit106a from the equilibrium melt into the glassy state were carried out using different cooling rates of 50 K/min, 100 K/min, and free radiation cooling (which corresponds to approximately 250 K/min in the temperature region of interest). The position of the

first maximum of the total structure factor, q_{max} was determined for these experiments. Data involving any crystallisation is excluded in the following discussion.

The positions of the first maximum of the total structure factor, q_{max} upon cooling at 50 K/min, 100 K/min, and at free radiation cooling are shown in figure 5.32.
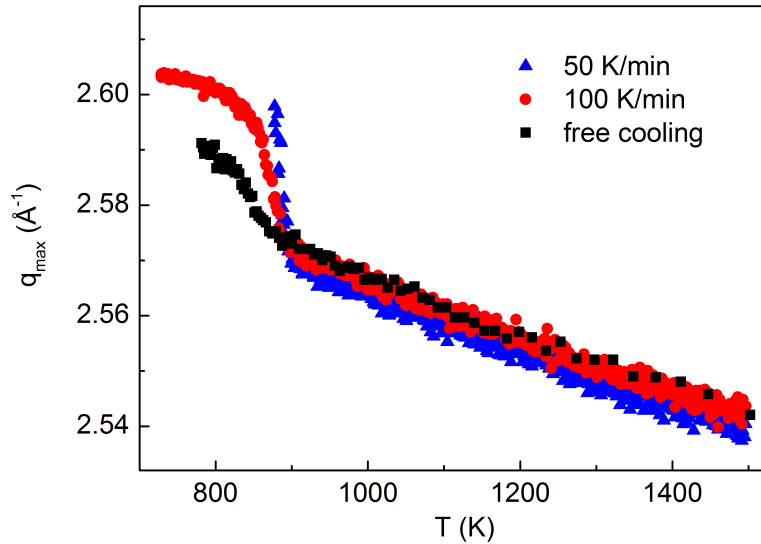
Figure 5.32 – Positions of the first maxima of the total structure factor (S(q)), q_{max} as function of temperature. Experiments on Vit106a are performed upon cooling from the equilibrium melt to below T_g at cooling rates of 50 K/min, 100 K/min, and at free radiation cooling (which corresponds to approximately 250 K/min in the temperature region of interest).

Here, q_{max} increases upon cooling from 1500 K to just below 900 K, independent of the cooling rate. Just below 900 K the respective q_{max} values increase and thus, show a discontinuity in their course. The increase in q_{max} is differently pronounced. The lower the cooling rate the more pronounced the increase in q_{max} is. In the case of the 100 K/min cooling rate sufficient data below 800 K is conducted to reason that after passing the change in slope q_{max} increases again with decreasing temperatures. For the other cooling rates, not sufficient data was conducted at these temperatures. In the case of the 50 K/min cooling rate due to crystallisation setting in at 865 K. However, experiments performed in section 5.13 showed that a similar behaviour of q_{max} is observed for free radiation cooling (see figure 5.29).

Next, the onset temperature for the change in slope of q_{max} ($T_{onset}^{q_{max}}$) is determined from figure 5.32. This is done individually for each cooling rate. The $T_{onset}^{q_{max}}$ temperatures are given in table 5.6. They deviate between 895 and 876 K for the 50 K/min cooling rate and the free radiation

cooling rate, which corresponds to approximately 250 K/min at 876 K. This deviation is within error bars according to the temperature uncertainties of section 4.2.1.

cooling rate	50 K/min	100 K/min	free radiation cooling
T_{onset}^{qmax} (K)	895 ($\pm$ 3.15)	892 ($\pm$ 2.85)	876 ($\pm$ 5.15)

Table 5.6 – Onset temperatures, T_{onset}^{qmax} for the change in slope of q_{max} determined from different cooling rates. Free radiation cooling corresponds to a cooling rate of approximately 250 K/min at 876 K.

Thus, the structural changes found in the undercooled melt of Vit106a showed no dependence on the investigated cooling rates. This may either be because no dependence exists or the variation of the cooling rate is too small. Experiments to extent the variation of the cooling rates are performed in section 5.16.

In figure 5.32 it was found that the changes in q_{max} are more pronounced the lower the cooling rate gets. This may indicate an underlying diffusion driven process, like nucleation. Obviously not in the classical sense in which nuclei form in a liquid phase and thereby start crystal growth, but perhaps in the sense of a transformation from one liquid phase into another. This transformation process takes a certain time, as indicated by the different cooling rates and is probably influenced by interfacial energy. The lower the cooling rate the more time remains for the transition to take place and the more pronounced it becomes. However, the onset temperatures for the change in q_{max} (see table 5.7) seem not vary significantly. This fact indicates a first order transition, however the temperature rate dependence of the quality of the transition is ? fast. Almost instantaneously nucleation
unusual for a first order transition.
Here, another consideration has to be made. Cooling a levitating sample always creates a temperature gradient from the inside to the outside of the sample. The higher the cooling rate the larger the gradient. This temperature gradient in turn induces thermal convection, meaning a certain flow exists in the sample. A possible explanation for the quality of the change in slope of q_{max} may be the consideration that the higher the cooling rate, the larger the temperature gradient becomes and the stronger the flow inside the sample gets. This may constrain the transformation process.

In conclusion, structural changes in the undercooled melt of Vit106a show no dependence on cooling rates varying between 50 K/min and 250 K/min. However, it was found that the quality of these structural changes does depend on the cooling rate. It becomes more pronounced the lower the cooling rate gets.

5.15 Thermal signal in the laser power course

In section 5.13, structural changes on the atomic scale were found in the undercooled melt of Vit106a and correlated with the thermal signal found in the corresponding c_p/ε course. However, c_p/ε signals can only be derived from free radiation cooling experiments and not from temperature controlled experiments. Therefore, a new method is introduced in this section to determine a thermal signal equivalent to the c_p/ε signal from temperature controlled experiments.

The dependence of structural changes on cooling rates investigated in section 5.13 was studied for cooling rates of 50 K/min, 100 K/min, and free radiation cooling. However, experiments performed at 50 K/min and 100 K/min provide no c_p/ε signal. Therefore, another way to detect an onset temperature equivalent to $T_{onset}^{c_p/\varepsilon}$ was developed within this work.

For this, a sample is levitated and subject to a preprogrammed temperature program (as in the experiments of section 5.13). The laser power necessary to follow this temperature profile is tracked, as shown in figure 5.33.
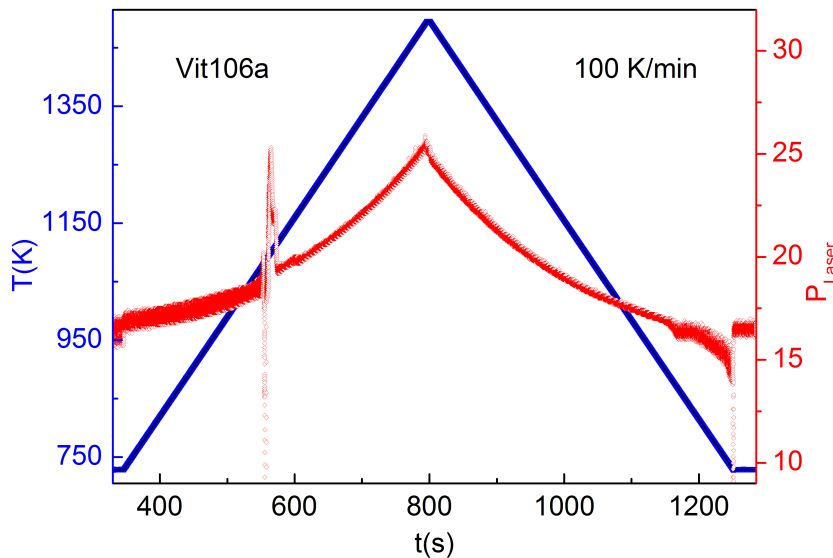
Figure 5.33 – Time-temperature profile with associated laser power of an experiment with heating and cooling rates of 100 K/min. (Corresponding q_{max} data is given in figure 5.32.)

Here, the defined heating and cooling rate of 100 K/min is given in blue (left axis), while the laser power necessary to run this time-temperature profile is given in red (right axis). Note, that actual and nominal temperature coincide and therefore only the actual temperature is displayed. Upon heating (350 - 800 s) the initially amorphous sample crystallised at 1075 K. This becomes visible in the sudden decrease in laser power. During crystallisation heat is dissipated and therefore less laser power is necessary to maintain the heating rate. The crystallisation process is followed by
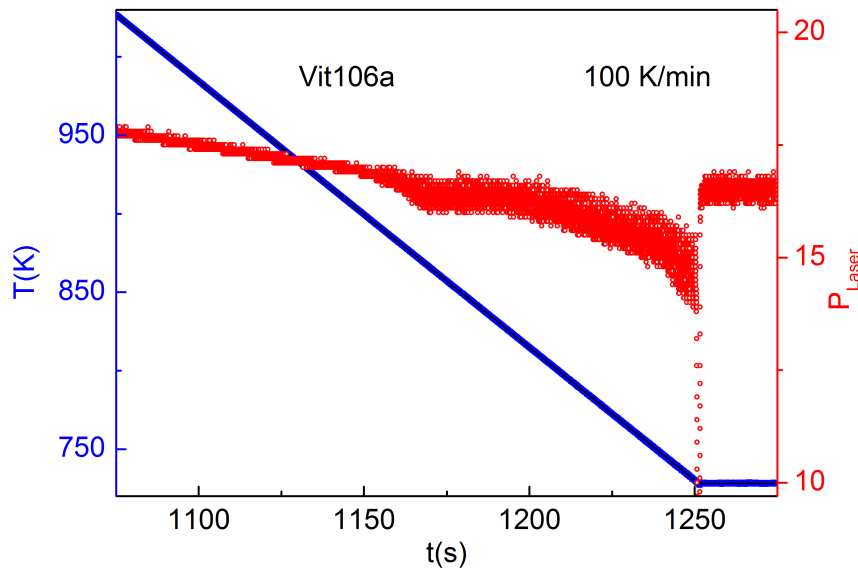
Figure 5.34 – Image section of figure 5.33. Time-temperature profile with associated laser power of an experiment with heating and cooling rates of $100\,\mathrm{K/min}$.

the melting process. Here, an increased laser power is required to overcome the phase transition. Upon cooling (800 - 1250 s in figure 5.33) the laser power decreases until at ~ 888 K (and 1170 s) a change in its course is observed, which can be seen in figure 5.33 and is shown again enlarged in figure 5.34. Here, the laser power indicates the onset temperature by a small decrease in its course, meaning the underlying reaction is an exothermic process and energy is released equivalent to the signal in the c_p/ε course (section 5.8). Thus, laser power can be used to determine an onset temperature from temperature controlled experiments similar to the onset temperature of free radiation cooling experiments. The onset temperature of this change in laser power course, $\mathrm{T}_{onset}^{laser\,power}$ is 888 K and correlates with the onset temperature of the change in slope of q_{max} upon cooling (see figure 5.32 and table 5.6), which is 892 K. Therefore, this signal in laser power found in the undercooled melt is also associated with structural changes on the atomic scale. It is thus, also an equivalent signal to the c_p/ε signal derived from free radiation cooling behaviour. The onset temperature for the change in laser power course was also determined for the cooling experiment using a cooling rate of $50\,\mathrm{K/min}$. All onset temperatures for changes in laser power course, c_p/ε behaviour, and q_{max} data are given in table 5.7 for the cooling rates of 50 K, 100 K, and free radiation cooling (which corresponds to a cooling rate of ~ 250 K/min at 876 K).

The onset temperatures given in table 5.7 vary between 895 K and 875 K. This deviation is within error bars as discussed in paragraph 4.2.1. Thus, onset temperatures for changes in laser power course, c_p/ε behaviour, and q_{max} data coincide with each other.

In conclusion, a new methods was developed to derive a thermal onset signal, equivalent to the

cooling rate	50 K/min	100 K/min	free radiation cooling
$T_{onset}^{q_{max}}$ (K)	895 ($\pm$ 4.15)	892 ($\pm$ 3.85)	876 ($\pm$ 7.15)
$T_{onset}^{c_p/\varepsilon}$ (K)	–	–	875 ($\pm$ 10.5)
$T_{onset}^{laserpower}$ (K)	890 ($\pm$ 4.5)	888 ($\pm$ 7.5)	–

Table 5.7 – Onset temperatures for changes in laser power course, c_p/ε behaviour, and q_{max} data for cooling rates of 50 K, 100 K, and free radiation cooling (which corresponds to a cooling rate of ~ 250 K/min at 876 K)

thermal c_p/ε signal of free radiation cooling experiments from temperature controlled experiments. This thermal signal found in the laser power course was correlated with the structural changes found in the undercooled melt of Vit106a. It is thus, concluded that these signals as well as the c_p/ε signal correspond to the same underlying process, which may be an strong-to-fragile transition.

5.16   Variation of cooling rates

Dependencies of onset temperatures on cooling rates provide information on the nature of phase transitions, as discussed in section 2.3.1.

The variation of cooling rates in experiments performed in section 5.14 allowed no clear statement on whether the onset temperature changes with the cooling rates. This, however gives information whether the underlying process is a phase transition of the first or second order. Therefore, cooling rates are varied to a maximum in this section.

In order to enlarge the cooling rate variation of the levitated sample two samples with different masses are processed in the ESL1. A 20 mg and a 103 mg Vit106a sample. These are the lightest and heaviest masses possible to levitate in the ESL1. The samples differ in weight by a factor of five. The difference in cooling rate is given later on.

Free radiation cooling experiments from ~ 1460 K were carried out (as already discussed in section 5.8 and 5.10). Both samples were cooled nine times in total. An exemplary cooling curve for each sample (20 and 103 mg) is shown in figure 5.35. These cooling curves show a time dependent temperature decay with a temperature dependence of $t^{\frac{1}{3}}$ (as expected from eq. 4.2). They exhibit no indications for a recalescence or crystallisation.

The corresponding c_p/ε signals were derived from the cooling curves (according to section 4.2). This was done for each of the nine cooling experiments performed on one sample (not shown). Again, only two exemplary c_p/ε curves, which correspond to the cooling curves in figure 5.35 are presented in figure 5.36. They belong to the 20 mg and 103 mg Vit106a sample, respectively.

These c_p/ε curves all show a consistent increase in c_p/ε upon cooling from ~ 1400 K until just
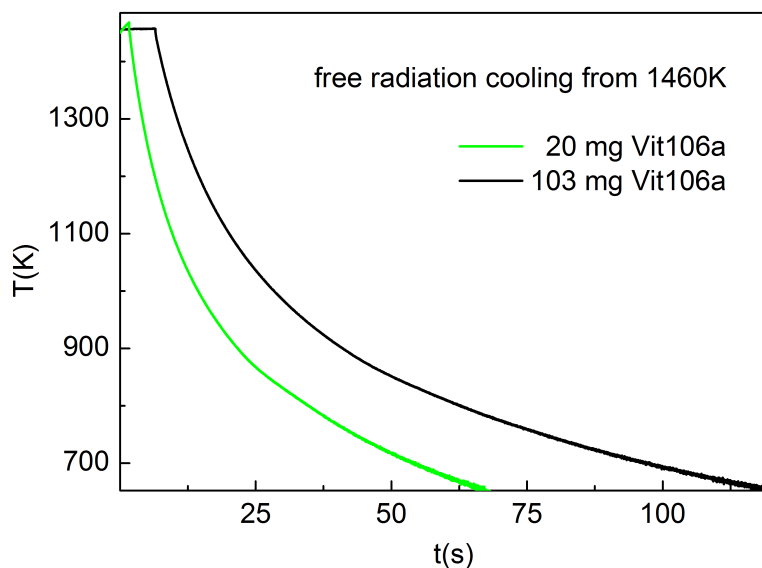
Figure 5.35 – Free radiation cooling experiments of a 20 mg and a 103 mg Vit106a sample performed in the ESL 1 (for information on ESL 1 see section 3.3.1).

below 900 K. Slightly below 900 K a peak in c_p/ε is found. The onset temperatures of these c_p/ε peaks are determined by creating tangents and specifying the intersection point, as indicated in figure 5.36. For the two cooling experiments displayed in this section the onset temperatures of the c_p/ε peaks are determined to be 893 K for the 20 mg sample and 892 K for the 103 mg sample. Cooling rates in this temperature region (around 895 K) are ~400 K/min for the 20 mg sample and ~245 K/min for the 103 mg sample.

The c_p/ε peaks of the remaining cooling experiments revealed an averaged c_p/ε onset temperature of 887 K for the 20 mg and of 896 K for the 103 mg sample. The individual onset temperatures varied about 15 K, which is within the measurement error (see paragraph 4.2.1).

This means the onset temperature of the c_p/ε signal remains unchanged within error bars, even though the cooling rate varies by a factor of 1.6. This statement, however only holds under the assumption that the experiments were not influenced by crystallisation. This assumption is considered true, because on the one hand cooling rates are either similar or by a factor of 1.6 greater than in comparable in situ monitored experiments. On the other hand the c_p/ε signals of this section occurred at similar temperatures than the c_p/ε signals of in situ monitored experiments, which are demonstrably free of crystallisation (see section 5.10).

Thus, these experiments demonstrate that the thermal signal found in the undercooled melt of Vit106a does not depend on cooling rates between 250 and 400 K/min.

Combined with the temperature controlled cooling experiment of section 5.14 (performed in the mobile ESL), a cooling rate variation between 50 K/min and 400 K/min is achieved. The corresponding onset temperatures are 890 K for the cooling experiment at 50 K/min and 887 K for the
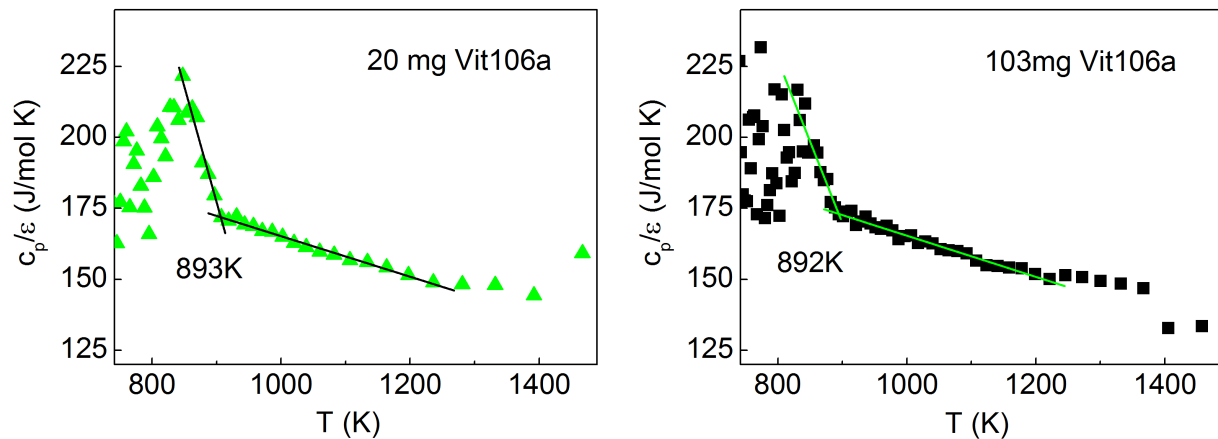
Figure 5.36 – The c_p/ε course of two Vit106a samples, which differ in weight by a factor of five. The c_p/ε data is determined from the free radiation cooling curves displayed in figure 5.35. The (left) curve corresponds to the 20 mg sample and has a peak onset temperature of 893 K while the (right) curve belongs to the 103 mg sample with a peak onset temperature of 892 K.

experiment with a cooling rate of ~ 400 K/min at the temperature region of interest. These two onset temperatures are similar and therefore, indicate that the thermal signal found in the undercooled state of Vit106a does not depend on cooling rates between 50 K/min and 400 K/min. This, in turn may be interpreted as an indication for a first order phase transition.

In conclusion, variation in cooling rates by a factor of 8 revealed no dependence on the corresponding thermal signal found in the undercooled melt of Vit106a. This finding indicates a first order phase transition.

5.17 Discussion and outlook

Experimental studies, performed within the previous sections of this work revealed indications for an underlying transition in Zr-based BMGs. Such an indication is for instance the discrepancy between the temperature dependences of high and low temperature viscosity behaviour (section 5.7).

In the following investigations the focus was placed on the composition Vit106a. This BMG is of particular interest, because it can be undercooled down to the glass transition temperature using the ESL technique. Therefore, measurements from the equilibrium melt down to the glass transition temperature can be performed for this composition.

In Vit106a an exothermic signal indicating an energy release was measured in the ratio of specific heat capacity to total hemispherical emissivity (section 5.8) as well as in the laser power course

of temperature controlled cooling experiments (section 5.15). Besides, in situ investigations revealed structural changes in the position of the first maximum of the total structure factor, q_{max} for this BMG (section 5.13). The onset of these structure changes shows no dependence on the cooling rate in the range between 50 and 400 K/min (section 5.14). However, the changes in q_{max} become more pronounced the slower the cooling rate gets (section 5.14).

Since, these signals occur at similar temperatures, they are associated with the same underlying process.

In summary, this means that the underlying process takes place upon cooling from the equilibrium melt, in the undercooled melt of Vit106a and is thermodynamically and structurally reflected by a release of internal energy and by local structure changes, respectively. In addition, the transition temperature at which this underlying process most likely occurs corresponds to the temperature at which a strong-to-fragile transition is expected (section 5.7). A transition in this temperature region would thus explains the discrepancy between high and low temperature viscosity behaviour.

These indications suggest a transition between a fragile high temperature liquid in the equilibrium melt and a stronger liquid around the glass transition temperature. The transition between these two states takes presumably place in the undercooled melt. For a more detailed description of the underlying transition, it is important to first exclude crystallisation as possible origin before interpreting the experimentally determined indications for a transition. This was done by several experiments and according to the following considerations.

An exothermic peak, which corresponds to an enthalpy of ~ 0.5 kJ/g-atom K (section 5.11) was measured in the undercooled melt of Vit106a. According to Gallino et al. [40] the enthalpy of crystallisation for Vit106a is 6.38 kJ/g-atom K. Thus, if the exothermic signal is due to crystallisation, it would correspond to approximately 8 % crystalline volume in the sample. 8 % crystalline volume should become obvious in the corresponding XRD patterns (section 5.13). However, the XRD patterns are free of Bragg peaks, which indicate crystallisation (section 5.13). In addition, crystals consume more volume than an amorphous phase. Roughly 8 % crystalline volume would become visible in the specific volume (section 5.9) or density course (section 5.3). This is not the case for Vit106a.

Moreover, the increase in q_{max} is limited to 880 - 800 K and clearly ends there (figure 5.29). If crystal growth is the underlying origin, it should continue upon further cooling. Thus, the behaviour found in q_{max} upon cooling is different from crystallisation behaviour. Yet, one can argue that the behaviour in q_{max} is caused by the formation of nano crystals, which are too small to rise Bragg peaks, but form broad diffuse maxima in the XRD patterns instead. In this case, it is unclear how ~ 8 % nano crystalline volume causes such a large discrepancy in temperature dependent viscosity behaviour (section 5.7). Viscosity experiments upon heating (section 5.2) showed that a remaining crystalline fraction (from the solid crystalline phase) causes only a maximum difference in viscosity of about 30 mPas (figure 5.7). It is therefore not clear how 8 % nano

crystalline volume should cause a greater difference in viscosity. Based on these considerations crystallisation as possible underlying origin for the transition phenomenon is excluded.

The structural investigations of q_{max} (section 5.13) suggest that two liquid states with different local structures exist above and below the point of transition (section 5.13 and 5.14). A possible interpretation for this is a polyamorphic (phase) transition from one amorphous phase into another. Such a transition is consistent with a liquid-liquid transition in e.g. water [74].
It is hypothesised that these two liquid phases are of strong and fragile character and thus, cause the strong-to-fragile transition and the discrepancy in temperature dependent viscosity behaviour.

This hypothesis of a transition is supported by the exothermic signal found in the c_p/ε course, which takes place at the same temperature in the undercooled melt as the structural changes are discovered. This signal does not depend on cooling rates between 50 and 400 K/min (section 5.16). It is associated with a first order phase transition, since it shows similarities to the heat of fusion or crystallisation in a solid-to-liquid (or vice versa) phase transition. The estimated change in enthalpy corresponds to roughly 8 % of the enthalpy of crystallisation of Vit106a (section 5.11). Similar values are found for the BMG Vitreloy 1 [114]. This shows that the enthalpy changes for the underlying transition are much smaller than for a liquid-crystal transition. This, in turn means that the energy barrier for the transition is much larger than for a liquid-crystal transition. Therefore, the strong liquid phase is considered as an intermediate state between fragile liquid and crystalline phase.
It is therefore concluded that the transition in the undercooled melt of Vit106a is a first order, polyamorphic transition, which separates a fragile high temperature liquid from a kinetically stronger liquid at lower temperatures. This transition shows no dependence on the cooling rate between 50 and 400 K/min and possesses a nucleation process. In levitation experiments no nucleation sites are present, therefore the transformation process presumably occurs due to homogeneous nucleation. The independence of the cooling rate can be explained by considering the time-temperature transformation diagram (figure 2.3). However, this time not for a melt-to-crystal transformation, but for a fragile-to-strong transformation. In this case, the c-shaped "nose" represents the transformation points where the strong liquid forms, while areas usually representing the melt, now represent the fragile liquid. Upon cooling, not sufficient time to bypass the "nose" is available and thus, the kinetically stronger liquid forms. On these time scales, the slope of the "nose" is nearly zero, meaning no cooling rate dependence becomes visible.
Even though the onset of the transition process, thus the nucleation shows no cooling rate dependence the quality of the structural changes does (section 5.14). This indicates a diffusion driven growth process, which becomes more pronounced the more time is available. This hypothesis is supported by the fact that the changes in q_{max} become more pronounced the slower the cooling rate gets (section 5.14).

Another phenomenon, likely to occur, but which should not be confused with an underlying

transition is chemical decomposition. Chemical decomposition or phase separation describes a process, in which a system decomposes into two (or more) immiscible phases with different compositions. Assuming that phase separation is the underlying origin of the local structure changes and the exothermic signal, two (or more) phases of different chemical compositions must have formed upon cooling below T_g. In this case, two (or more) glass transition temperatures are expected to exist, corresponding to each of the separated phases. However, this is not the case, when performing a DSC scan on amorphous, as-cast Vit106a material. Phase separation causes compositional changes. These changes should become detectable in the thermal expansion coefficient. The thermal expansion coefficient of Vit106a, however is constant within the temperature region of interest (section 5.9). Hence, no major differences in concentration exist. It is therefore concluded that either no or only small compositional changes exist, which cause no detectable variation in the thermal expansion coefficient.

Based on the indications discussed above and which support a transition, it is hypothesised that upon cooling, the fragile liquid transforms into a strong liquid phase. However, this happens only if the investigated system is at its critical composition at the point of transition. If the composition of the system does not correspond to the critical composition it decomposes into two phases of similar or slightly different compositions, but with different local structures. This means that phase separation with a small compositional difference can be part of the underlying transition. Note that the LLT, as recently discussed in literature [114, 112], is indeed not an exclusive phenomenon of phase separation [114]. If the composition of the system is not right on the critical point, phase separation can be part of the LLT. In this case both processes, polyamorphic transition and phase separation occur simultaneously.

The in situ structural investigations showed that the two liquid phases above and below the point of transition differ in structure. This manifests in an increase in q_{max}. An increase in q_{max} denotes a decrease in the interatomic distance, since q_{max} is an inverse spacing. Meaning the averaged next neighbour distance between an atom and its nearest neighbour shell decreases. However, no changes are found in the temperature depended density course at this temperature (see figure 5.8). This means, the structural changes occur only locally on the short-range at most medium-range order.

A decrease in interatomic distances can be associated with an increase in density. However, it should be noted that density describes a macroscopic property and the structure factor characterises a microscopic property. These two properties do not necessarily correlate with each other.

In addition, it should be noted that there is no direct relationship between diffraction maxima and interatomic distances for glassy and liquid alloys according to N. Mattern [70]. Different local arrangements in different liquids may lead to different q_{max} values even for identical atomic volumes [70].

In order to derive real space information from a measured total structure factor it has to be

transformed into the partial pair correlation functions of the alloys via a Fourier transformation. Vit106a, as a five component BMG possesses 15 different pairs of partial correlation functions, which all contribute to the measured total structure factor. Due to the variety of individual pair correlation function it is not possible to provide more detailed real space information. But, since Zr has the highest concentration in Vit106a and the second largest atomic number (of 40 (Nb : 41)) it is hypothesised that Zr-Zr correlations dominate the contribution to the first peak of S(q) and thus q_{max}. Therefore, the discontinuity in q_{max} is associated with a decrease in the Zr-Zr interatomic distances in real space.

The increase in q_{max} can be interpreted as a transition from larger to smaller length scales on Zr-dominant interatomic distances. Assuming that the number and species of atoms stays constant on the measured length scales, a transition from larger to smaller length scales indicates a change in local atomic packing density from a looser to more densely packed state.

Similar structural studies have been performed on Vitreloy 1. Here, Wei et al. [114] discovered similar structure changes in q_{max} in the undercooled melt of Vitreloy 1. However, these changes in q_{max} are in opposite to those changes in q_{max} found in Vitreloy 106a, as shown in figure 5.37.
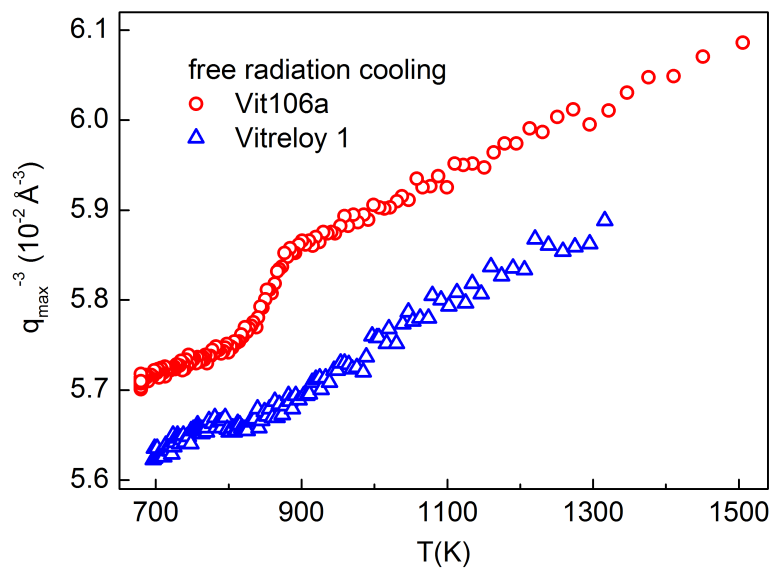
Figure 5.37 – Temperature dependence of the peak position of the first maximum of the total structure factor, q_{max}^{-3} upon free radiation cooling for Vit106a and Vitreloy 1. Vit106a shows a discontinuity at ~ 890 K, while Vitreloy 1 shows it at ~ 830 K. Data of Vitreloy 1 is taken from reference [114] and shifted by 0.3 (10^{-2} Å^{-3}) up for clarity.

The structure changes in Vitreloy 106a exhibit a negative slope at the region of transition, while the structure changes in Vitreloy 1 show a positive slope. Wei et al. [114] interpreted the structure changes in Vitreloy 1 as a transition in the local atomic packing density from a denser to a looser state.

The reason for these opposing structure changes in q_{max} is not apparent. Vitreloy 1 as well as 106a is a five component BMG and exhibits excellent glass forming abilities. Furthermore, they exhibit similar glass transition (T_g^{Vit1} = ~ 640 K , $T_g^{Vit106a}$ = 670 K) and liquidus temperatures (T_{liq}^{Vit1} = 1026 K , $T_{liq}^{Vit106a}$ = 1113 K). They only differ in composition. The major component in both BMGs is Zr, while they also contain Cu and Ni. Additionally, Vitreloy 106a contains Al and Nb, while Vitreloy 1 contains Be and Ti instead.

It should be noted that section 5.4 revealed that Al causes a looser packing density with a decrease in the mean packing density in viscous systems. Peng et al. [84] showed on the example of Al-Au compositions that Al exhibits a soft interaction potential. This means that interatomic distances between Al atoms are much more sensitive to the melt composition and temperature than for instance Au-Au interatomic distances. Therefore, alloys containing Al differ to alloys without Al. This may be one reason why Vitreloy 1 and 106a exhibit different slopes in q_{max} at the region of transition and why the transition is more pronounced in Vitreloy 106a.

In conclusion, these experimental findings suggest a first order transition in the undercooled state of Vit106a, which separates a high temperature fragile liquid from a strong liquid at lower temperatures. The transformation process is considered to be homogeneous nucleation followed by a diffusion driven growth process. The results presented within this work are in line with a transition of a polyamorphic nature, whose kinetics are controlled by diffusion. Whether chemical composition changes occur in the different liquid phases is subject to further investigations.

All these measurements, however, give no information on the behaviour of individual atoms, but only on the atomic structure as a whole. In order to decode the behaviour of individual atoms during an LLT, neutron diffraction experiments can be used to investigate the short-range order of melts. By combining neutron scattering experiments with the technique of isotope substitution, partial structure factors can be determined and topological and chemical structure of the melt can be described [59]. However, partial structure factors can only be obtained for binary, maximum ternary systems. And these systems are known to require such high cooling rates to form a glass, that they can not be achieved using the ESL technique. Thus, multicomponent BMG formers, as investigated within this thesis are inevitable to first understand the mechanism of the LLT, because they offer experimental access to the temperature region of interest.

Another conceivable option to elucidate the transition on an atomic scale are computer simulations. Molecular dynamic (MD) simulations, for example, can be used to describe the behaviour of liquids on a microscopic scale [56]. Here, a system of particles interacts via a potential and the corresponding Newton's equations of motion are solved for the system [100].

More specifically, a system with a fixed number of particles (typically 1000 to 10000 particles for the study of viscous liquids) and with a constant volume is considered. Such systems typically have periodic boundary conditions in order to prevent surface effects. Every particle in such a system has a certain velocity according to the Maxwell-Boltzmann distribution at a certain tem-

perature. The system is than moved in small time intervals and according to Newton's equation of motion. Position and velocity of each particle are tracked [100].

Molecular time scales are in the order of picoseconds (ps). This means, the time steps in the numerical integration of the equation of motion must be smaller than ps; they are typically on the femtosecond (fs) scale [109]. The best MD simulations these days can thus calculate a few ns per day for big systems of up to 1 million particles [81].

In the following an approximation is made to estimate the time scales and computing time necessary for a MD simulation on the BMG Vit106a.

Yang et al. measured liquid viscosity (η) and structural relaxation (τ) data on Vitreloy 4 [119]. According to Maxwell's relation (equation 2.4) these two properties are linked via the shear modulus. In this approximation it is assumed that the shear moduli of Vitreloy 4 and Vit106a are similar and constant over a few hundred Kelvin. Therefore, viscosity and structural relaxation time at 1100 K, hence approximately at the liquidus temperature of Vit106a, are determined for Vitreloy 4. It exhibits a viscosity of nearly 100 mPas and a structural relaxation time of 15 to 20 ps. Vit106a, at this temperature exhibits a viscosity of ~ 275 mPas (extrapolated from fig. 5.5) and assuming a similar shear modulus for the two BMGs a relaxation time of approximately 50 ps. However, the closer one gets to the glass transition the longer time scales and computing times become. Therefore, the viscosity data of Vit106a as shown in figure 5.5 is extrapolated down to the temperature region of interest, namely 880 K. Here, Vit106a exhibits a viscosity of approximately 850 Pas and the corresponding relaxation time is 150 ns, thus 0.15 μs.

While structural relaxation times in the order of ns are feasible to simulate, simulation times increase drastically upon greater relaxation times. Relaxation times in the order of ms already take about 1000 days, thus approximately 3 years for a MD simulation to process [109]. Therefore, MD simulations on an LLT are very time consuming due to the slow time scales but are generally feasible.

Furthermore, it must be stressed that MD simulations need an effective interaction potential in order to let atoms interact with each other. Building such a potential is not trivial for the elements of BMGs investigated in this thesis [109]. Suppose a simulation shows no LLT then it can not be clearly stated whether it is due to a poor interaction potential or because there is simply no LLT present.

Hence, MD simulations are not the very first option to directly investigate an LLT, because time scales are too slow and computing times are disproportionately long. However, this means that the question whether an LLT is a result of the multiple components can not be answered yet (using MD simulations).

In order to bypass the slow time scales another simulation method could be an possible option. If really two equilibrium phases, above and below the LLT exist Monte Carlo simulation would be such an option. In a Monte Carlo simulation particles are not moved according to Newton's equation of motion but randomly, meaning they are brought into equilibrium using an artificial

dynamic. The idea here is that if the LLT is a thermodynamic transition different equilibrium structure parameters should be found on both sides of the transition. However, the viscosity behaviour can not be determined using a Monte Carlo simulation and the transition can only be detected if it really is a thermodynamic phase transition. In addition, the objection to building the interaction potentials remains the same as in MD simulations. Therefore, Monte Carlo simulations are not an option either to investigate the LLT.

Chapter 6

Summary

The central objective of this work was to study thermodynamic and kinetic aspects of the strong-to-fragile crossover in bulk metallic glasses (BMGs). In addition, special emphasis was placed on understanding the nature of the underlying transition of such crossovers, for example through structural aspects.

Viscosity is a property which provides information on the kinetic behaviour of melts. The kinetic fragility can be directly derived from the temperature dependence of melt viscosities. Evenson et al. [38] found a discrepancy in fragility between the high and low temperature regime in several Zr-based bulk metallic glasses. Way et al. [111] discovered a hysteresis-like temperature dependency in the equilibrium viscosity of $Zr_{41.2}Ti_{13.8}Cu_{12.5}Ni_{10}Be_{22.5}$ (Vitreloy 1) depending on the measurement's starting temperature. These are crucial indications for a strong-to-fragile crossover. Thus, viscosity is an important parameter for the investigations at hand.

However, melt viscosities are experimentally challenging to determine due to the high chemical reactivity of these metallic melts. This manifests in viscosity data obtained by different measurement techniques for Vitreloy 1, which scatter over two orders of magnitude [46].

Therefore different high temperature measurement methods were compared within this work and discussed in terms of their accuracy. These methods were Couette rheology, electrostatic (ESL), and electromagnetic levitation (EML) in combination with the oscillating drop technique and the latter under microgravity conditions. Among them, electrostatic levitation proved to be the most precise method to investigate melt viscosities of BMGs. Moreover, it was found that temperature dependent equilibrium melt viscosities, which were measured using the ESL technique, can be described by a single fragility parameter. This is in contrast to the finding made by Way et al. [111] which documents the discovery of a hysteresis-like temperature dependency of the viscosity in the equilibrium melt of Vitreloy 1. This new ESL data in combination with viscosity data around the glass transition temperature revealed a discrepancy in fragility between high and low temperature regimes.

Moreover, the ESL technique covers a broad temperature range and enables access to the deeply undercooled liquid state due to the absence of container walls, which may act as heterogeneous

nucleation sites. ESL was therefore used for following investigations on the thermodynamic and structural nature of the strong-to-fragile transition. For this, the focus was placed on the composition Vitreloy 106a, which is of particular interest because it can be undercooled down to the glass transition temperature without crystallisation. It is thus a very promising composition to investigate a dynamic crossover and its underlying origin.

Investigations of the density, specific volume, or thermal expansion coefficient in the equilibrium and undercooled melt revealed no indications for a transition. However, studies of the ratio of specific heat capacity to emissivity revealed an exothermic signal in the undercooled melt upon free radiation cooling.

In a further step, the ESL technique is combined with structural investigations using high energy x-rays of the PETRA III P07 beamline facility located at the German Electron Synchrotron (DESY) in Hamburg. This setup enables time-resolved structural information on a microscopic scale of equilibrium and undercooled BMG-forming melts. These in situ investigations revealed structural changes in the peak position of the first maximum of the total structure factor in the undercooled melt at the same temperature as the exothermic signal was found. Since these phenomena occur at the same temperature, they were attributed to the same underlying process. The onset temperature of these structural changes was found to be independent of the cooling rate in the range of 50 to 400 K/min. However, the structural changes in the peak position of the first maximum of the total structure factor are larger with slower cooling rates.

These experimental findings suggest a first order transition in the undercooled state of Vit106a, which separates a fragile high temperature liquid from a stronger liquid at lower temperatures. Whether chemical composition changes occur in the different liquid phases is subject to further investigations. The results presented within this work are in line with a transition of a polyamorphic nature, whose kinetics are controlled by diffusion.

Bibliography

[1] *Lumasense Techniologies, IMPAC Infrared Thermometers, Technical data sheet.*

[2] Wah Chang Allegheny Technologies (USA), Technical data sheet Zircadyne 702®/705®. 2012.

[3] Wah Chang Allegheny Technologies (USA), Technical data sheet Zirconium crystal bar. 2012.

[4] S. Aasland and P. McMillan. Density-driven liquid–liquid phase separation in the system AI2O3–Y2O3. *Nature*, 369(6482):633–636, 1994.

[5] A. Angell. Formation of glasses from liquids and biopolymers. *Sience*, 267(5206):1924–1935, 1995.

[6] A. Angell. Liquid fragility and the glass transition in water and aqueous solutions. *Chemical Reviews*, 102(8):2627–2650, 2002.

[7] A. Angell. Insights into phases of liquid water from study of its unusual glass-forming properties. *Science*, 319(5863):582–587, 2008.

[8] C. A. Angell. Relaxation in liquids, polymers and plastic crystals – strong to fragile patterns and problems. *Journal of Non-Crystalline Solids*, 131:13–31, 1991.

[9] C. A. Angell. Glass formation and glass transition in supercooled liquids, with insights from study of related phenomena in crystals. *Journal of Non-Crystalline Solids*, 354(42):4703–4712, 2008.

[10] E. Bakke, R. Busch, and W. Johnson. The viscosity of the $Zr_{46.75}Ti_{8.25}Cu_{7.5}Ni_{10}Be_{27.5}$ bulk metallic glass forming alloy in the supercooled liquid. *Applied Physics Letters*, 67(22):3260–3262, 1995.

[11] J. Barrat, J. Badro, and P. Gillet. A strong to fragile transition in a model of liquid silica. *Molecular Simulation*, 20(1-2):17–25, 1997.

[12] A. Bartsch. *Diffusion und Viskosität in der Gleichgewichtsschmelze und im unterkühlten Zustand glasbildender Metalllegierungen.* PhD thesis, Christian-Albrechts-Universität zu Kiel, 2009.

[13] S. W. Basuki, A. Bartsch, F. Yang, K. Rätzke, A. Meyer, and F. Faupel. Decoupling of component diffusion in a glass forming $Zr_{46.75}Ti_{8.25}Cu_{7.5}Ni_{10}Be_{27.5}$ melt far above the liquidus temperature. *Physical Review Letters*, 113(16), 2014.

[14] E. Becker, W. J. Hiller, and T. A. Kowalewski. Experimental and theoretical investigation of large amplitude oscillations of liquid droplets. *Journal of Fluid Mechanics*, 231:189–210, 1991.

[15] J. Bendert, M. Blodgett, A. Gangopadhyay, and K. Kelton. Measurements of volume, thermal expansion, and specific heat in $Zr_{57}Cu_{15.4}Ni_{12.6}Al_{10}Nb_5$ and $Zr_{58.5}Cu_{15.6}Ni_{12.8}Al_{10.3}Nb_{2.8}$ liquids and glasses. *Applied Physics Letters*, 102(21), 2013.

[16] J. Bernal. A geometrical approach to the structure of liquids. *Nature*, 183(4655):141–147, 1959.

[17] J. Bernal. Geometry of the structure of monatomic liquids. *Nature*, 185:67–70, 1960.

[18] P. Bovenkamp. *Seminar zur Theorie der Teilchen und Felder.* PhD thesis, Westfälische Wilhelms-Universität Münster, 2011.

[19] J. Brillo. Habilitation. RWTH Aachen 2016.

[20] J. Brillo and I. Egry. Density determination of liquid copper, nickel, and their alloys. *International Journal of Thermophysics*, 24(4), 2003.

[21] R. Busch, E. Bakke, and W. L. Johnson. Viscosity of the supercooled liquid and relaxation at the glass transition of the $Zr_{46.75}Ti_{8.25}Cu_{7.5}Ni_{10}Be_{27.5}$ bulk metallic glass forming alloy. *Acta Materialia*, 46(13):4725–4732, 1998.

[22] R. Busch and W. L. Johnson. The kinetic glass transition of the $Zr_{46.75}Ti_{8.25}Cu_{7.5}Ni_{10}Be_{27.5}$ bulk metallic glass former-supercooled liquids on a long time scale. *Applied Physics Letters*, 72(21):2695–2697, 1998.

[23] R. Busch, W. Liu, and W. L. Johnson. Thermodynamics and kinetics of the $Mg_{65}Cu_{25}Y_{10}$ bulk metallic glass forming liquid. *Journal of Appield Physics*, 83(8):4134–4141, 1998.

[24] R. Busch, J. Schroers, and W. Wang. Thermodynamics and kinetics of bulk metallic glass. *MRS Bulletin*, 32(08):620–623, 2007.

[25] S. Chathoth, A. Meyer, M. Koza, and F. Juranyi. Atomic diffusion in liquid Ni, NiP, PdNiP, and PdNiCuP alloys. *Applied physics letters*, 85(21):4881–4883, 2004.

[26] S. Chen, Y. Zhang, M. Lagi, S. Chong, P. Baglioni, and F. Mallamace. Evidence of dynamic crossover phenomena in water and other glass-forming liquids: experiments, MD simulations and theory. *Journal of Physics: Condensed Matter*, 21(50):504102, 2009.

[27] Y. Cheng, E. Ma, and H. Sheng. Atomic level structure in multicomponent bulk metallic glass. *Physical Review Letters*, 102(24):245501, 2009.

[28] M. Cohen and D. Turnbull. Molecular Transport in Liquids and Glasses. *The Journal of Chemical Physics*, 31(5):1164–1169, 1959.

[29] D. Cummings and D. Blackburn. Oscillations of magnetically levitated aspherical droplets. *Journal of Fluid Mechanics*, 224:395–416, 1991.

[30] W. Demtröder. *Experimentalphysik 3: Atome, Moleküle und Festkörper*. Springer Verlag, 2010.

[31] DLR. http://www.dlr.de/mp/, August 2015.

[32] A. Drehmann, A. Greer, and D. Turnbull. Bulk formation of a metallic glass: Pd40Ni40P20. *Applied Physics Letters*, 41(8):716–171, 1982.

[33] S. Earnshaw. On the nature of the molecular forces which regulate the constitution of the luminiferous ether. *Trans. Camb. Phil. Soc.*, 7:97, 1842.

[34] T. Egami and S.J.L.Billinge. *Underneath the Bragg peaks: structural analysis of complex materials*, volume 7. Pergamon, Oxford, 1 edition, 2003.

[35] I. Egry, G. Lohöfer, I. Seyhan, S. Schneider, and B. Feuerbacher. Viscosity of eutectic $Pd_{78}Cu_6Si_{16}$ measured by the oscillating drop technique in microgravity. *Applied Physics Letters*, 73:462, 1998.

[36] Z. Evenson. *On the thermodynamic and kinetic properties of bulk glass forming metallic systems*. PhD thesis, Universität des Saarlandes, 2012.

[37] Z. Evenson, S. Raedersdorf, I. Gallino, and R. Busch. Equilibrium viscosity of Zr–Cu–Ni–Al–Nb bulk metallic glasses. *Scripta Materialia*, 63(6):573–576, 2010.

[38] Z. Evenson, T. Schmitt, M. Nicola, I. Gallino, and R. Busch. High temperature melt viscosity and fragile to strong transition in Zr–Cu–Ni–Al–Nb(Ti) and $Cu_{47}Ti_{34}Zr_{11}Ni_8$ bulk metallic glasses. *Acta Materialia*, 60:4712, 2012.

[39] H. Eyring. Viscosity, plasticity, and diffusion as examples of absolute reaction rates. *The Journal of Chemical Physics*, 4(4):283–291, 1936.

[40] I. Gallino, M. B. Shah, and R. Busch. Enthalpy relaxation and its relation to the thermodynamics and crystallization of the $Zr_{58.5}Cu_{15.6}Ni_{12.8}Al_{10.3}Nb_{2.8}$ bulk metallic glass-forming alloy. *Acta Materialia*, 55(4):1367–1376, 2007.

[41] M. Goldstein. Viscous liquids and the glass transition. V. Sources of the excess specific heat of the liquid. *The Journal of Chemical Physics*, 64(11):4767–4774, 1976.

[42] N. Greaves, M. Wilding, S. Fearn, D. Langstaff, F. Kargl, S. Cox, Q. Van, O. Majérus, C. Benmore, R. Weber, et al. Detection of first-order liquid/liquid phase transitions in yttrium oxide-aluminum oxide melts. *Science*, 322(5901):566–570, 2008.

[43] A. Hammersley. FIT2D V9. 129 Reference Manual V3. 1. *Inter Rep ESRF98HA01, ESRF, Grenoble*, 1998.

[44] J. Heinrich, R. Busch, F. Müller, S. Grandthyll, and S. Hüfner. Role of aluminum as an oxygen-scavenger in zirconium based bulk metallic glasses. *Applied Physics Letters*, 100(7):071909, 2012.

[45] P. Heintzmann. *Untersuchungen der Zusammenhänge von atomare Struktur, Selbstdiffusion, Interdiffusion und Viskosität in flüssigen Zr-Ni Legierungen*. PhD thesis, Ruhr-Universität Bochum, 2014.

[46] P. Heintzmann, F. Yang, S. Schneider, G. Lohöfer, and A. Meyer. Viscosity measurements of metallic melts using the oscillating drop technique. *Applied Physics Letters*, 108(24):241908, 2016.

[47] W. Hembree. *Dissertation*. PhD thesis, Universität des Saarlandes, 2015.

[48] M. Hemmati, C. Moynihan, and A. Angell. Interpretation of the molten BeF2 viscosity anomaly in terms of a high temperature density maximum, and other waterlike features. *Journal of Chemical Physics*, 115(14):6663–6671, 2001. Computer simulations.

[49] D. Holland-Moritz, S. Stüber, H. Hartmann, T. Unruh, T. Hansen, and A. Meyer. Structure and dynamics of liquid $Ni_{36}Zr_{64}$ studied by neutron scattering. *Physical Review B*, 79(6):064204, 2009.

[50] R. W. Hyers. Fluid flow effects in levitated droplets. *Measurement Science and Technology*, 16(2):394, 2005.

[51] Idzikowski, Bogdan and Švec, Peter and Miglierini, Marcel. *Properties and Applications of Nanocrystalline Alloys from Amorphous Precursors: Proceedings of the NATO Advanced Research Workshop.*, volume 184. Springer Science & Business Media, 2005.

[52] A. Inuoe, T. Negishi, H. Kimura, T. Zhang, and A. Yavari. High packing density of Zr-and Pd-based bulk amorphous alloys. *Materials Transactions, JIM*, 39(2):318–321, 1998.

[53] T. Ishikawa, P. F. Paradis, N. Koike, and Y. Watanabe. Effects of the positioning force of electrostatic levitators on viscosity measurements. *Review of Scientific Instruments*, 80(1), 2009.

[54] K. Ito, C. Moynihan, and A. Angell. Thermodynamic determination of fragility in liquids and a fragile-to-strong liquid transition in water. *Nature*, 398(6727):492–495, 1999.

[55] W. Johnson. Fundamental aspects of bulk metallic glass formation in multicomponent alloys. *Materials science forum*, 225:35–50, 1996.

[56] J.P. Hansen and I.R. McDonald. *Theory of simple liquids*. Elsevier, 1990.

[57] K. Rätzke and P. W. Hüppe and F. Faupel. Transition from single-jump type to highly cooperative diffusion during structural relaxation of a metallic glass. *Physical Review Letters*, 68(15):2347, 1992.

[58] W. Klement, R. Willens, and P. Duwez. Non-crystalline structure in solidified gold–silicon alloys. *Nature*, 187, 1960.

[59] T. Kordel. *Nahordnung und atomare Dynamik in elektrostatisch levitierten Zr-Basis-Schmelzen*. PhD thesis, Ruhr-Universität Bochum, 2011.

[60] T. Kordel, D. Holland-Moritz, F. Yang, J. Peters, T. Unruh, T. Hansen, and A. Meyer. Neutron scattering experiments on liquid droplets using electrostatic levitation. *Physical Review B*, 83(10), 2011.

[61] H. Kui, A. Greer, and D. Turnbull. Formation of bulk metallic glass by fluxing. *Applied Physics Letters*, 45(6):615–616, 1984.

[62] K. N. Lad, N. Jakes, and A. Pasturel. Signatures of fragile-to-strong transition in a binary metallic glass-forming liquid. *The Journal of Chemical Physics*, 136(10):104509, 2012.

[63] H. Lamb. On the oscillations of a viscous spheroid. *Proc. of London Mathematical Society*, 1(1):51 − 70, 1881.

[64] S. Lan, M. Blodgett, K. Kelton, J. Ma, J. Fan, and X.-L. Wang. Structural crossover in a supercooled metallic liquid and the link to a liquid-to-liquid phase transition. *Applied Physics Letters*, 108(21), 2016.

[65] B. Legg, J. Schroers, and R. Busch. Thermodynamics, kinetics, and crystallization of $Pt_{57.3}Cu_{14.6}Ni_{5.3}P_{22.8}$ bulk metallic glass. *Acta Materialia*, 55(3):1109–1116, 2007.

[66] J. Löffler, J. Schroers, and W. Johnson. Time–temperature–transformation diagram and microstructures of bulk glass forming Pd40Cu30Ni10P20. *Applied Physics Letters*, 77(5):681–683, 2000.

[67] S. Maruyama, K. Wakabayashi, and M. Oguni. Thermal properties of supercooled water confined within silica gel pores. In *SLOW DYNAMICS IN COMPLEX SYSTEMS: 3rd International Symposium on Slow Dynamics in Complex Systems*, volume 708, pages 675–676, 2004.

[68] B. Massey and J. Ward-Smith. *Mechanics of fluids*, volume 1. CRC Press, 1998.

[69] A. Masuhr, T. Waniuk, R. Busch, and W. Johnson. Time scales for viscous flow, atomic transport, and crystallization in the liquid and supercooled liquid states of $Zr_{41.2}Ti_{13.8}Cu_{12.5}Ni_{10}Be_{22.5}$. *Physical Review Letters*, 82(11):2290, 1999.

[70] N. Mattern. Comment on Thermal expansion measurements by X-ray scattering and breakdown of Ehrenfest's relation in alloy liquids Appl. Phys. Lett. 104, 191907 (2014). *Applied Physics Letters*, 105(25):256101, 2014.

[71] N. Mauro, M. Blodgett, M. Johnson, A. Vogt, and K. Kelton. A structural signature of liquid fragility. *Nature Communications*, 5, 2014.

[72] T. Meister. *Aufbau und Regelung eines elektrostatischen Levitators*. PhD thesis, Ruhr-Universität Bochum, 2000.

[73] T. Meister, H. Werner, G. Lohöfer, D. Herlach, and H. Unbehauen. Gain-scheduled control of an electrostatic levitator. *Control Engineering Practice*, 11(2):117–128, 2003.

[74] O. Mishima, L. Calvert, and E. Whalley. An apparently first-order transition between two amorphous phases of ice induced by pressure. *Nature*, 314(6006):76–78, 1985.

[75] O. Mishima and H. Standley. The relationship between liquid, supercooled and glassy water. *Nature*, 396(6709):329–335, 1998.

[76] S. Mukherjee, J. Schroers, Z. Zhou, W. Johnson, and W. Rhim. Viscosity and specific volume of bulk metallic glass-forming alloys and their correlation with glass forming ability. *Acta Materialia*, 52(12):3689–3695, 2004.

[77] S. Mukherjee, Z. Zhou, J. Schroers, W. L. Johnson, and W. Rhim. Overheating threshold and its effect on time-temperature-transformation diagrams of zirconium based bulk metallic glasses. *Applied Physics Letters*, 84(24):5010–5012, 2004.

[78] C. Neumann. Pat. DE 10 2013 203 555 B3, 2015.

[79] C. Neumann. . PhD thesis, Universität des Saarlandes, in preparatio for 2017.

[80] NOVESPACE. http://www.novespace.fr, August 2015.

[81] U. of Illinois at Urbana-Champaign. http://www.ks.uiuc.edu/research/namd/performance.html, April 2016.

[82] L. Pauling. Atomic radii and interatomic distances in metals. *Journal of the American Chemical Society*, 69(3):542–553, 1947.

[83] A. Peker and W. Johnson. A highly processable metallic glass: $Zr_{41.2}Ti_{13.8}Cu_{12.5}Ni_{10}Be_{22.5}$. *Applied Physics Letters*, 63(17):2342–2344, 1993.

[84] H. Peng, T. Voigtmann, G. Kolland, H. Kobatake, and J. Brillo. Structural and dynamical properties of liquid Al-Au alloys. *Physical Review B*, 92(18):184201, 2015.

[85] I. Pommrich. *Selbstdiffusion in Siliziumreichen Legierungsschmelzen*. PhD thesis, Ruhr-Universität Bochum, 2010.

[86] P. Poole, M. Hemmati, and A. Angell. Comparison of thermodynamic properties of simulated liquid silica and water. *Physical Review Letters*, 79(12):2281–2284, 1997. computer simulations.

[87] X. Qiu, L. Thompson, and S.J.L.Billinge. PDFgetX2: a GUI-driven program to obtain the pair distribution function from X-ray powder diffraction data. *Journal of Applied Crystallography*, 37(4):678–678, 2004.

[88] L. Ratke, H. Walter, and B. Feuerbacher. *Materials and Fluids Under Low Gravity*, volume 464. Springer Berlin Heidelberg, 1996.

[89] W. K. Rhim, K. Ohsaka, P. F. Paradis, and R. E. Spjut. Noncontact technique for measuring surface tension and viscosity of molten materials using high temperature electrostatic levitation. *Review of Scientific Instruments*, 70(6):2796 – 2801, 1999.

[90] I. Saika-Voivod, P. Poole, and F. Sciortino. Fragile-to-strong transition and polyamorphism in the energy landscape of liquid silica. *Nature*, 412(6846):514–517, 2001. computer simulations.

[91] K. Samwer, J. Li, W. K. Rhim, C. Kim, and W. Johnson. Evidence for a liquid–liquid phase transition in metallic fluids observed by electrostatic levitation. *Acta Materialia*, 59(5):2166–2171, 2011.

[92] S. Schneider. *Viskositäten unterkülter Metallschmelzen*. PhD thesis, Rheinisch-Westfälische Technische Hochschule Aachen, 2002.

[93] S. Schneider, I. Egry, R. Wunderlich, R. Willnecker, and M. Pütz. Evaluation of thermophysical data from electromagnetic levitation experiments with digital image processing. *Journal of the Japan Society of Microgravity Application*, 25(3):387 – 391, 2008.

[94] J. Schroers. On the formability of bulk metallic glass in its supercooled liquid state. *Acta Materialia*, 56(3):471–478, 2008.

[95] J. Schroers, W. Johnson, and R. Busch. Crystallization kinetics of the bulk-glass-forming $Pd_{43}Ni_{10}Cu_{27}P_{20}$ melt. *Applied Physics Letters*, 77(8):1158–1160, 2000.

[96] J. Schroers, B. A. Legg, and R. B. and. Thermodynamics, kinetics, and crystallization of $Pt_{57.3}Cu_{14.6}Ni_{5.3}P_{22.8}$ bulk metallic glass. *Acta Materialia*, 55(3):1109–1116, 2007.

[97] D. Scott. Packing of spheres: packing of equal spheres. *Nature*, 188(4754):908–909, 1960.

[98] L. Shadowspeaker and R. Busch. On the fragility of Nb-Ni-based and Zr-based bulk metallic glasses. *Applied Physics Letters*, 85(13), 2004.

[99] W. Shuai, M. Stolpe, O. Gross, Z. Evenson, I. Gallino, W. Hembree, J. Bednarcik, J. Kruzic, and R. Busch. Linking structure to fragility in bulk metallic glass-forming liquids. *Applied Physics Letters*, 106(18):181901, 2015.

[100] S. Sondermann. *Einfluss von Kreuzkorrelationen auf die Interdiffusion in aluminiumreichen Al-Ni-Schmelzen.* PhD thesis, Ruhr-Universität Bochum, 2015.

[101] F. W. Starr, A. Angell, and E. Stanley. Prediction of entropy and dynamic properties of water below the homogeneous nucleation temperature. *Physica A: Statistical Mechanics and its Applications*, 323:51–66, 2003.

[102] M. Stolpe, I. Jonas, S. Wei, W. Hembree, Z. Evenson, F. Yang, A. Meyer, and R. Busch. Structural changes during a liquid-liquid transition in the deeply undercooled $Zr_{58.5}Cu_{15.6}Ni_{12.8}Al_{10.3}Nb_{2.8}$ bulk metallic glass forming melt. *Physical Review B*, 93(1):014201, 2016.

[103] G. Tammann. Der Glaszustand . *Leopold Voss, Leipzig*, 1933.

[104] H. Tanaka. Relation between thermodynamics and kinetics of glass-forming liquids. *Physical Review Letters*, 90(5):055701, 2003.

[105] H. Tanaka, R. Hajime, and H. Mataki. Liquid-liquid transition in the molecular liquid triphenyl phosphite. *Physical Review Letters*, 92(2):025701, 2004.

[106] P. A. Tipler and G. Mosca. *Physik für Wissenschaft und Ingenieure.* Spectrum, Akademischer Verlag, 6. Auflage edition, 2009.

[107] V. Zöllmer and H. Ehmler and K. Rätzke and P. Troche and F. Faupel. Isotope effect of Co diffusion in thin amorphous Co51Zr49 layers during structural relaxation. *EPL (Europhysics Letters)*, 51(1):75, 2000.

[108] B. van Beest, G. Kramer, and R. van Santen. Force fields for silicas and aluminophosphates based on ab initio calculations. *Physical Review Letters*, 64(16):1955, 1990.

[109] T. Voigtmann. Deutsches Zentrum fürr Luft- und Raumfahrt e.V., Institute für Material-physik im Weltraum, private Mitteilung.

[110] T. Voigtmann, A. Meyer, D. Holland-Moritz, S. Stüber, T. Hansen, and T. Unruh. Atomic diffusion mechanisms in a binary metallic melt. *Europhysics Letters*, 82(6), 2008.

[111] C. Way, P. Wadhwa, and R. Busch. The influence of shear rate and temperature on the viscosity and fragility of the $Zr_{41.2}Ti_{13.8}Cu_{12.5}Ni_{10}Be_{22.5}$ metallic–glass–forming liquid. *Acta Materialia*, 55(9):2977 – 2983, 2007.

[112] S. Wei. *Kinetic, thermodynamic, and structural transitions in order-disorder alloys and bulk metallic glass-forming alloys.* PhD thesis, Universität des Saarlandes, 2014.

[113] S. Wei, I. Gallino, R. Busch, and A. Angell. Glass transition with decreasing correlation length during cooling of Fe50Co50 superlattice and strong liquids. *Nature Physics*, 7(2):178–182, 2011.

[114] S. Wei, F. Yang, J. Bednarcik, I. Kaban, O. Shuleshova, A. Meyer, and R. Busch. Liquid–liquid transition in a strong bulk metallic glass-forming liquid. *Nature communications*, 4, 2013.

[115] R. Willnecker, S. Schneider, and F. Munstermann. Digital video system for TEMPUS on parabolic flights. In *56th International Astronautical Congress*, pages 1–7, 2005.

[116] L. Xu, P. Kumar, S. Buldyrev, S. Chen, P. Poole, F. Sciortino, and H. Stanley. Relation between the Widom line and the dynamic crossover in systems with a liquid–liquid phase transition. *Proceedings of the National Academy of Science of the USA*, 102(46):16558–16562, 2005.

[117] W. Xu, M. Sandor, Y. Yu, H.-B. Ke, H.-P. Zhang, M.-Z. Li, W. Wang, L. Liu, and Y. Wu. Evidence of liquid-liquid transition in glass-forming La50Al35Ni15 melt above liquidus temperature. *Nature communications*, 6, 2015.

[118] F. Yang. Deutsches Zentrum fürr Luft- und Raumfahrt e.V., Institute für Materialphysik im Weltraum, private Mitteilung.

[119] F. Yang, T. Unruh, and A. Meyer. Coupled relaxation processes in a glass forming Zr-TiNiCuBe liquid. *EPL (Europhysics Letters)*, 107(2):26001, 2014.

[120] C. Yuan, F. Yang, F. Kargl, D. Holland-Moritz, G. Simeoni, and A. Meyer. Atomic dynamics in Zr-(Co, Ni)-Al metallic glass-forming liquids. *Physical Review B*, 91(21), 2015.

[121] C. Zhang, L. Hu, Y. Yue, and J. Mauro. Fragile-to-strong transition in metallic glass-forming liquids. *Journal of Chemical Physics*, 133(1):014508, 2010.

[122] C. Zhou, L. Hu, Q. Sun, J. Qin, X. Bian, and Y. Yue. Indication of liquid-liquid phase transition in CuZr-based melts. *Applied Physics Letters*, 103(17):171904, 2013.

Abbreviations

BMG	Bulk metallic glass
ESL	Electrostatic levitation/levitator
EML	Electromagnetic levitation/levitator
LLT	Liquid-liquid transition
VFT	Vogel-Fulcher-Tammann
μg	Microgravity
T$_g$	Glass transition
T$_{liq}$	Liquidus temperature
T$_{sol}$	Solidus temperature
T$_{melt}$	Melting temperature
SEM	Scanning electron microscopy
EBSD	Electron backscattering diffraction
EDX	Energy-dispersive X-ray spectroscopy
QNS	Quasi neuron scattering
3PBB	Three point beam bending
Vit 1	Vitreloy 1, $Zr_{41.2}Ti_{13.8}Cu_{12.5}Ni_{10}Be_{22.5}$
DSC	Differential scanning calorimetry
GFA	Glass forming ability

Acknowledgements

Curriculum Vitae

Isabell Jonas
born 26th of June, 1985 Kiel, Germany

since 01.11.2012	PhD student at the Institute of Materials Physics in Space, German Aerospace Center (DLR), Cologne
09.2011 - 05.2012	Institute for Superconducting and Electronic Materials (ISEM), University of Wollongong, Australia Master thesis: "Liquid crystals of large graphene oxide dispersions: A novel drug carrier system "
10.2009 - 06.2012	Christian-Albrechts-Universität Kiel Master in Materials Science and Engineering
04.2009 - 09.2009	Institute of Materials Physics in Space, German Aerospace Center (DLR), Cologne Bachelor thesis: "Metalldiffusion in der Germaniumschmelze: Referenzversuch unter normalen Gravitationsbedingungen"
10.2006 - 09.2009	Christian-Albrechts-Universität Kiel Bachelor in Materials Science and Engineering
07.2005 - 07.2006	Work and Travel Australia
08.1996 - 06.2005	Humboldt-Gymnasium, Kiel
1992 - 1996	Primary school Quarnbek-Strohbrück, Schleswig-Holstein